

## Bringing coating surfaces to life

***Citation for published version (APA):***

Vissschers, F. L. L. (2021). *Bringing coating surfaces to life: Electric field-driven surface dynamics of PDMS*. [Phd Thesis 1 (Research TU/e / Graduation TU/e), Chemical Engineering and Chemistry]. Technische Universiteit Eindhoven.

***Document status and date:***

Published: 30/04/2021

***Document Version:***

Publisher's PDF, also known as Version of Record (includes final page, issue and volume numbers)

***Please check the document version of this publication:***

- A submitted manuscript is the version of the article upon submission and before peer-review. There can be important differences between the submitted version and the official published version of record. People interested in the research are advised to contact the author for the final version of the publication, or visit the DOI to the publisher's website.
- The final author version and the galley proof are versions of the publication after peer review.
- The final published version features the final layout of the paper including the volume, issue and page numbers.

[Link to publication](#)

***General rights***

Copyright and moral rights for the publications made accessible in the public portal are retained by the authors and/or other copyright owners and it is a condition of accessing publications that users recognise and abide by the legal requirements associated with these rights.

- Users may download and print one copy of any publication from the public portal for the purpose of private study or research.
- You may not further distribute the material or use it for any profit-making activity or commercial gain
- You may freely distribute the URL identifying the publication in the public portal.

If the publication is distributed under the terms of Article 25fa of the Dutch Copyright Act, indicated by the "Taverne" license above, please follow below link for the End User Agreement:

[www.tue.nl/taverne](http://www.tue.nl/taverne)

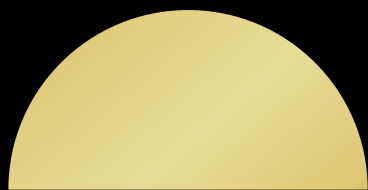
***Take down policy***

If you believe that this document breaches copyright please contact us at:

[openaccess@tue.nl](mailto:openaccess@tue.nl)

providing details and we will investigate your claim.

**BRINGING COATING  
SURFACES TO LIFE:  
ELECTRIC FIELD-DRIVEN  
SURFACE DYNAMICS OF PDMS**



**FABIAN VISSCHERS**



# Bringing coating surfaces to life

Electric field-driven surface dynamics of PDMS

## PROEFSCHRIFT

ter verkrijging van de graad van doctor aan de Technische Universiteit  
Eindhoven, op gezag van de rector magnificus prof.dr.ir. F.P.T. Baaijens, voor  
een commissie aangewezen door het College voor Promoties, in het openbaar  
te verdedigen op vrijdag 30 april om 11:00 uur

door

Fabian Ludovicus Louis Visschers

geboren te Meerssen

Dit proefschrift is goedgekeurd door de promotoren en de samenstelling van de promotiecommissie is als volgt:

voorzitter:	prof.dr. F. Gallucci
1 <sup>e</sup> promotor:	prof.dr. D.J. Broer
2 <sup>e</sup> promotor:	prof.dr. A.P.H.J. Schenning
copromotor(en):	dr. D. Liu
leden:	prof.dr.ir. D.C. Nijmeijer
	prof.dr. G.H. Gelinck
	prof.dr. T. Seki (Nagoya University)
	prof.dr. G.J. Vancso (Universiteit Twente)

*Het onderzoek of ontwerp dat in dit proefschrift wordt beschreven is uitgevoerd in overeenstemming met de TU/e Gedragscode Wetenschapsbeoefening.*

*"It's the questions we can't answer that teach us the most. They teach us how to think. If you give a man an answer, all he gains is a little fact. But give him a question and he'll look for his own answers."*

– Patrick Rothfuss

A catalogue record is available from the Eindhoven University of Technology Library  
ISBN: 978-90-386-5268-9

Copyright © 2021 by Fabian Visschers

Cover design by Stefanie van den Herik

Printed by Proefschriftmaken

The research described in this thesis was financially supported by the Netherlands  
Foundation for Scientific Research and the European Research Council.

# Table of Contents

<b>Chapter 1</b>	Introduction	7
<b>Chapter 2</b>	Oscillating surfaces fueled by a continuous AC electric field	25
<b>Chapter 3</b>	Finite element simulations on electric-field induced oscillating surfaces	39
<b>Chapter 4</b>	Improved electrode design for programmed surface oscillations	51
<b>Chapter 5</b>	Patterned surface dynamics at substrate-restricted electroactive silicone coatings	65
<b>Chapter 6</b>	High-frequency surface dynamics in electroactive polymer coatings with SU-8 microstructures	77
<b>Chapter 7</b>	Technology assessment	91
<b>Summary</b>		103
<b>Samenvatting</b>		107
<b>Acknowledgments</b>		111
<b>Curriculum Vitae</b>		115
<b>List of Publications</b>		117





# Chapter 1

## Introduction

---

This chapter is partially reproduced from: 'Liquid crystal polymers with motile surfaces'  
F.L.L. Visschers, M. Hendrikx, Y. Zhan, D. Liu, *Soft Matter*, 2018, 14, 4898-4912.

## 1.1 General introduction

In nature, micro- and nanostructured surfaces provide a huge variety of functions, such as wettability,<sup>[1,2]</sup> adhesion,<sup>[3,4]</sup> signaling,<sup>[5]</sup> temperature control,<sup>[6]</sup> transport barrier,<sup>[7]</sup> and protection against harmful radiation and mechanical stress.<sup>[8]</sup> Inspired by the effectiveness of nature, scientists have developed numerous artificial coatings incorporating similar structures for applications like self-cleaning,<sup>[9–11]</sup> adhesive tapes,<sup>[12–14]</sup> drag reduction,<sup>[15]</sup> anti-icing,<sup>[16]</sup> anti-fogging<sup>[17]</sup> and anti-reflection.<sup>[18]</sup> The structures in most of these coatings are static and as such, they cannot switch between different functionalities or be turned on and off again. The ability to alter surface structures is appealing, not only for applications involving haptics or (soft) robotics where surfaces perform multiple tasks, but also to introduce new applications like active mixing in microfluidic devices or unidirectional transport of matter over a surface. The movement of dynamic micro- and nanostructures found on surfaces in nature usually serves a very specific function. Take for example the human respiratory system, where the bronchus in the lungs are covered with moving protrusions and cilia. These cilia play an essential role, as their specific rhythmic waving motion moves microbes and dirt out of the airways, allowing us to breathe easily and without irritation. Similar to nature, we too can create artificial switchable coatings that respond to various external stimuli like pH,<sup>[19]</sup> light<sup>[20,21]</sup>, temperature<sup>[22,23]</sup> and electric fields<sup>[24–26]</sup>. Those dynamic coatings demonstrate the capability to deform, morph or grab and release, and have already introduced new functions for various applications.

## 1.2 Dynamic surface topographies in liquid crystal networks

One popular method to reversibly induce surface topographies in polymer coatings is by using liquid crystal networks (LCNs). Liquid crystals are materials with a mesophase in which molecules can align themselves into nematic or smectic phases, depending on their chemical structure. In 2006, Feringa et al.<sup>[27]</sup>

published in Nature the generation of rotational surface reliefs in liquid crystal films under continuous light illumination. In their method, a light-responsive chiral molecular motor is embedded in the liquid crystal film, which continuously inverses its chirality under UV exposure. The enantiomeric inversion results in the winding and unwinding of the helix. This realignment of the cholesteric liquid crystals in their fingerprint mode can then lead to dynamic topographies with a continuous rotation of the fingerprint. The surface motion can exert work by rotating a small glass fiber placed on top of it. The coating, however, is still in the liquid phase and not able to withstand any mechanical force. By modification of these mesogens with reactive groups, the liquid crystalline order can be frozen into a network to provide mechanical stability and maintain its anisotropic properties at a larger temperature range. In their polymeric state, LCNs can remain responsive to various external stimuli, like temperature, light and electric fields or even a combination of these.

### **1.2.1 Thermal responsive coatings**

Thermal responsive surface topographies can be formed using patterned polymer coatings, in which cholesteric regions are embedded in an isotropic matrix through a two-step polymerization process.<sup>[28]</sup> The isotropic and cholesteric areas experience different thermal expansion coefficients at an elevated temperature resulting in protrusions formed in the cholesteric regions (Figure 1.1). Similar surface profiles can also be created with defect patterns through a photo-alignment technique.<sup>[29,30]</sup> The photo-alignment layer contains azo-dye molecules that can reorient their long axes perpendicular to the local light polarization. Defects can be written by using a plasmonic photomask in which the linear polarization follows pre-designed patterns. Upon heating above the glass transition temperature ( $\sim 50$  °C), both indentations and protrusions can be developed in the defect areas. The dynamic surface topography is fully reversible

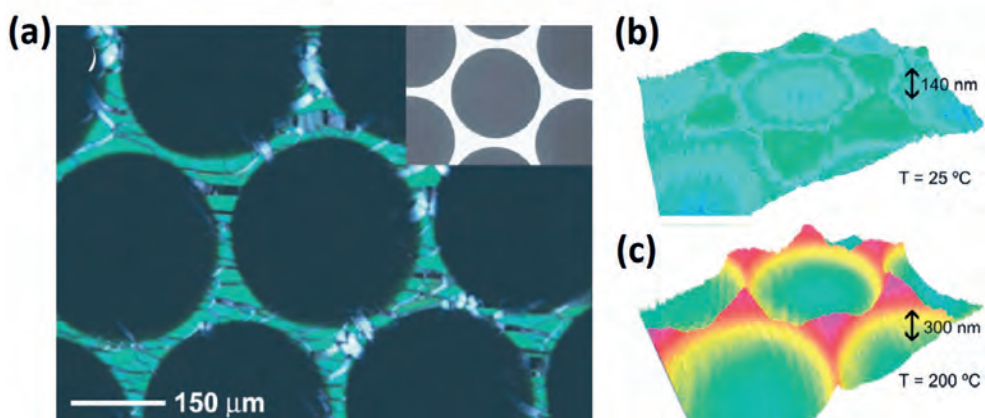


**Figure 1.1** | (a) A pattern with hexagonal packing of isotropic circles in a cholesteric matrix as seen through an optical polarizing microscope. The inset shows the photomask that was used to obtain the pattern. (b) Image from a white light interferometer at room temperature. (c) Image from a white light interferometer at 175 °C. Reproduced from reference 28.

unless the materials are heated to above 150 °C, when irreversible strains may be developed.

Surface topographies, both dynamic and static, can also be generated in two material combinations where a difference in modulus and thermal expansion lead to wrinkling of the top layer.<sup>[31–35]</sup> Typically, the combination of poly(dimethyl siloxane) and a hard top coating deforms randomly when being heated. Better controlled wrinkling can be achieved by selecting an oriented liquid crystal polymer as one of the materials. The directionality of the thermal expansion coefficient in this case leads to patterns with controlled shape and direction.

### 1.2.2 Light responsive coatings

Coatings based on LCNs can be made light-responsive by the addition of azobenzene molecules. Illuminating azobenzene moieties with ultraviolet light will cause an isomerization reaction from the ground *trans* state to the *cis* state, which reduces its molecular length from 9 to 5.5 Å.<sup>[36]</sup> Upon isomerization, the geometric change results in a small photomechanical effect within amorphous polymers,<sup>[37,38]</sup> which is amplified by integrating the azobenzenes into LCNs. With this

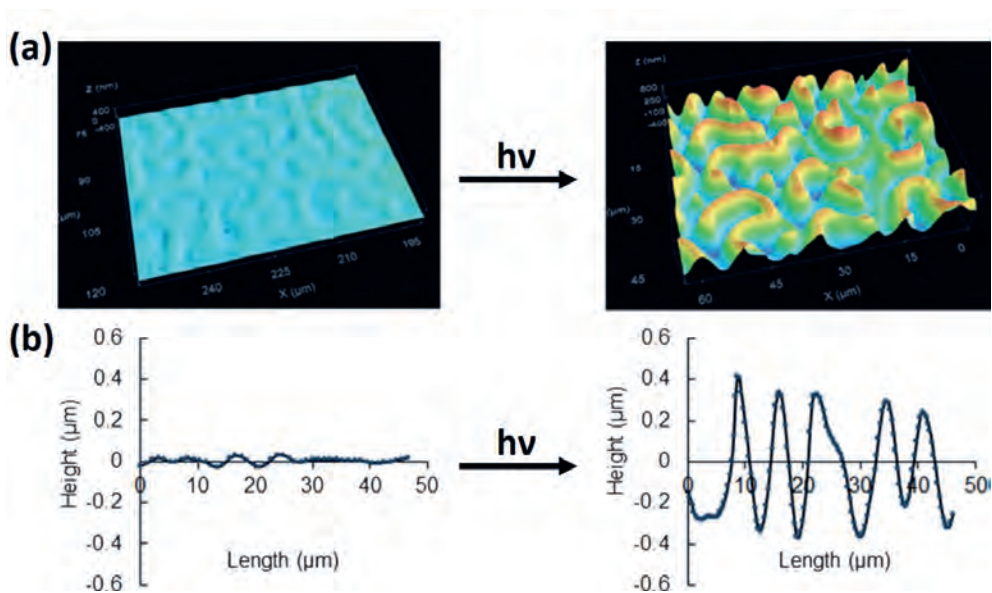


**Figure 1.2** | (a) An LCN coating containing fingerprint patterns. The 3D surface topographies from interferometer measurements are given before (left) and during UV-light exposure (right). (b) Corresponding surface profiles of the LCN coatings before (left) and after UV-light exposure (right). Reproduced from reference 21.

knowledge, many groups have demonstrated different photomechanical effects of azobenzene-modified liquid crystal polymers.<sup>[39–44]</sup> The incorporated azobenzene changes the order in the LCN coating which leads to mechanical stresses, which in turn, lead to surface deformations. For instance, when a coating is made with a periodic structure containing areas with a molecular orientation perpendicular to the surface next to areas with a planar cholesteric structure.<sup>[45]</sup> During actuation, the cholesteric regions expand perpendicular to the plane of the coating due to a reduction of the order parameter, as well as due to the generation of free volume. In the homeotropic regions, the reduction in order parameter causes an expansion parallel to the substrate. Combined, these effects increase the height of the protrusions to a strain value close to 20%. The same method can also be applied to LCN coatings where the mesogens are self-assembled into fingerprint structures (Figure 1.2).<sup>[21]</sup> The azobenzenes in LCN coatings can even be used to achieve oscillatory deformation under continuous illumination.<sup>[46]</sup> The dichroic properties of the *trans*-isomer cause it to

preferentially absorb linearly polarized UV light parallel to its electrical dipole moment.<sup>[47]</sup> Upon rotation of the linear polarized UV light under continuous blue light irradiation, the topographies show oscillatory deformations.

### 1.2.3 Electric field responsive coatings

Electric fields can be used to create free volume within LCN coatings by the incorporation of a large dipole moment, either parallel or perpendicular to the long axis of the mesogens.<sup>[24]</sup> Liquid crystals capped with a cyano group are well-known examples of mesogens with their dipole moment parallel to the long axis. During the oscillation, the liquid crystal molecules are continuously changing their orientation and packing. By tuning the AC frequencies to natural network frequencies, resonance-enhanced oscillatory dynamics are initiated which amplifies the deformation (Figure 1.3). The natural network frequencies, however, continuously change due to the deformation of the network. As soon as the system finds a new equilibrium, the resonance condition change again, resulting in a continuous loop of chaotic fluctuations. This method shows applicatory results by removing dust and debris under both dry and humid conditions.<sup>[25]</sup>

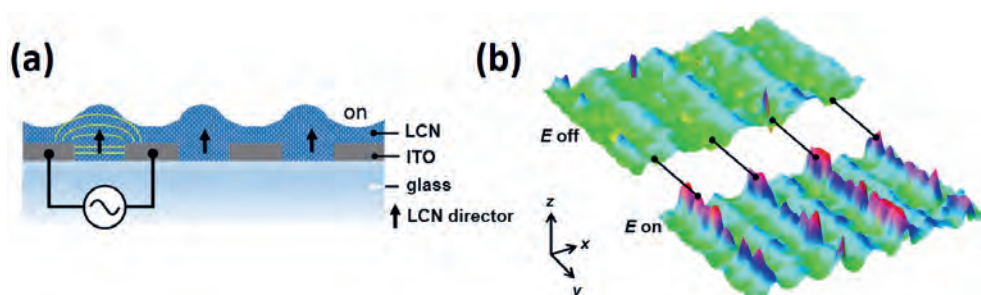


**Figure 1.3** | (a) Volume increase induced in a homeotropically aligned LCN by a lateral electric field from interdigitating indium tin oxide electrodes. (b) 3D images of the LCN coating with and without an electric field. Reproduced from reference 24.

### 1.2.4 Advantages and limitations

The previously discussed temperature and light-responsive coatings are useful because they can be programmed to provide a response under certain conditions when no human intervention is required. Alternatively, electric field responsive coatings provide active control over functionality, which is more useful when using electronic devices like mobile phones. Furthermore, with electric field responsive coatings, it is easy to provide a high-frequency input which could potentially lead to a high-frequency output in terms of surface dynamics. With LCN coatings however, these high-frequency inputs only give a high-frequency output on a molecular level. This molecular motion is necessary to induce the free volume that causes the surface deformation and takes about 10 seconds to complete on a macroscopic scale. Although the coatings display random oscillatory motion after activation, there is no direct correlation with the frequency of the applied electric field. In order to create dynamic surface topographies that oscillate fast and at a controllable frequency in response to an electric field, we decided to look for alternative methods and materials.

## 1.3 Electroactive polymers and Maxwell stresses

Polymers that change shape in response to electrical stimulation are generally referred to as 'electro-active polymers' (EAPs). Dependent on their mode of action, they can be classified as 'ionic' or 'electronic' EAPs.<sup>[48-50]</sup> Ionic EAPs are materials that are driven by the mobility or diffusion of ions. As they often require a solvent to allow transportation of the ions, they do not seem suitable for application in thin coatings where evaporation and leaking can occur rapidly. Electronic EAPs on the other hand are materials that respond directly to an external electric field, without the use of added charge carriers. As a result, they usually have fast response times and are more suitable for coating applications. Ferroelectric polymers, electrostrictive graft elastomers, liquid-crystal networks



and dielectric elastomers are all considered electronic EAPs. Although each of these polymer types has its advantage and disadvantage, dielectric elastomers stand out due to their large strain values, quick response, high mechanical energy densities and their ability to hold an induced displacement at constant voltage without consuming electrical energy.<sup>[51,52]</sup> The only disadvantage of dielectric elastomers is that these materials show the best performance at high electric fields close to the breakdown voltage.<sup>[50]</sup>

A dielectric elastomer device consists of two stretchable electrodes separated by the dielectric elastomer in a two-plate capacitor setup (Figure 1.4). The application of an electric field induces electrostatic attraction between the opposite charges of both electrodes, causing them to close in on each other. During this process, the area  $A$  is increased and the thickness  $z$  is reduced, which changes the capacitance of the dielectric material twice and increases its effectiveness in converting energy. The electric energy storage is enhanced by the polarizability of the dielectric, which is determined by the dielectric constant  $\epsilon_r$ . The mechanical energy storage is determined by the elastic modulus  $Y$ . Pelrine et al.<sup>[53]</sup> have mathematically derived the conversion of electrical energy into mechanical energy by the dielectric elastomer. They describe differential changes  $dU_e$  in electrical energy  $U_e$  for a plate capacitor that holds charge  $Q$  across the capacitance  $C$ .

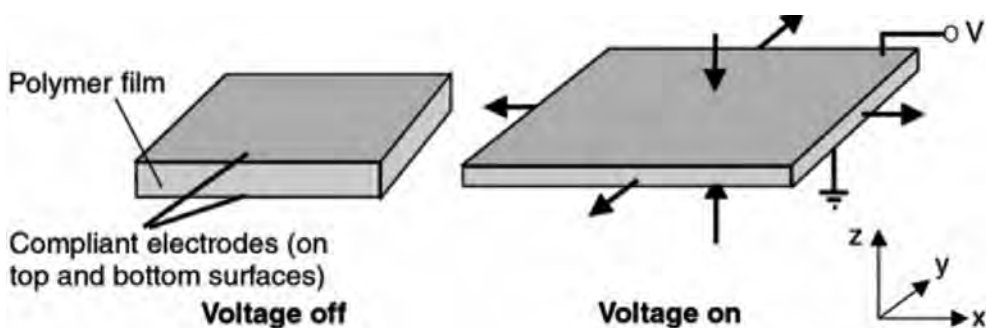


**Figure 1.4** | Schematic overview showing the working principle of dielectric elastomers. The two stretchable electrodes are charged with opposite polarity. The electrostatic forces pull the electrodes together which reduces the thickness of the film while increase its surface area. Reproduced from reference 48.

$$dU_e = \left(\frac{Q}{C}\right) dQ - 2U_e \left(\frac{1}{A}\right) dA = \left(\frac{Q}{C}\right) dQ + 2U_e \left(\frac{1}{z}\right) dz \quad (1)$$

In Equation (1)  $(Q/C)dQ$  represents the change of electrical energy and  $dQ$  is the change of the electrical charge in the capacitor. Next,  $2U_e(1/z)dz$  represents the mechanical work done by the electric field. At a constant charge  $Q$ , the transducer works as a generator if the film thickness  $z$  is increased. If the film thickness is decreased at a constant charge, the transducer works as an actuator. Assuming a constant charge, preservation of volume and after the introduction of the energy content of the capacitor, you can derive the equation for the Maxwell stress  $p$ .

$$p = \epsilon_0 \epsilon_r \left(\frac{V}{z}\right)^2 \quad (2)$$

In equation (2)  $V$  is the voltage applied and  $\epsilon_0$  and  $\epsilon_r$  are the permittivity of vacuum and the dielectric constant of the material. Finally, an expression for the free stroke  $S_z$  can be derived by assuming a linear elastic response, free boundary conditions and by introducing Young's modulus  $Y$ .

$$S_z = -\frac{1}{Y} \epsilon_0 \epsilon_r \left(\frac{V}{z}\right)^2 \quad (3)$$

The performance of such a dielectric elastomer is proportional to the dielectric constant and the square of the electric field in the capacitor. For this reason, increases in the  $(V/z)$  or  $\epsilon_r$  are the most obvious ways to affect the efficiency of the device. Unfortunately,  $(V/z)$  can only be increased until a certain limit, determined by the material's dielectric breakdown strength. If this point is exceeded the device is damaged by a large current passing through the dielectric material. Increasing the dielectric constant can be achieved by introducing polar groups with orientational degrees of freedom. Their translational mobility must remain low to avoid a lowering of the dielectric breakdown strength.

## 1.4 Dielectric elastomeric materials

The previous section covered the basic principles of dielectric elastomers and showed that the performance and energy density can be increased by increasing the dielectric constant and dielectric breakdown strength. To obtain a proper dielectric device however, the material should meet several other requirements as well. The polymers need to have a very low specific conductivity in order to store electrical energy for a considerable period. If a current leaks through the material, the energy conversion of the device becomes less efficient and heat will be generated. Furthermore, a low modulus of the polymer is required for an effective deformation, but the modulus should still be high enough to prevent electro-mechanical instabilities. Finally, the polymer needs to be tear-resistant and chemically and thermally stable. Several classes of materials exist which can be used for dielectric elastomers: acrylates, silicones, urethanes, rubbers, etc. In this introduction we focus on acrylates and silicones, which are most well known in literature and usually do not require plasticizers.

### 1.4.1 Acrylates

Acrylates are one of the most widely studied dielectric elastomers, because they are abundant, have high film quality, low cost and exhibit excellent performance at high electric fields. A standard acrylic dielectric elastomer is produced by 3M corporation and commercialized under the name VHB 4910, and due to its large strains and elastic energy density, it has been used in many studies.<sup>[54–58]</sup> The response of the materials is predictable, as equations relating the applied voltage to the measured force from an actuator fit well with experimental data.<sup>[55]</sup> Furthermore, the material also exhibits a small electrostrictive effect, indicated by the drop in dielectric constant when the polymer is strained. Similar to the dielectric constant, the dielectric breakdown strength is also dependent on the

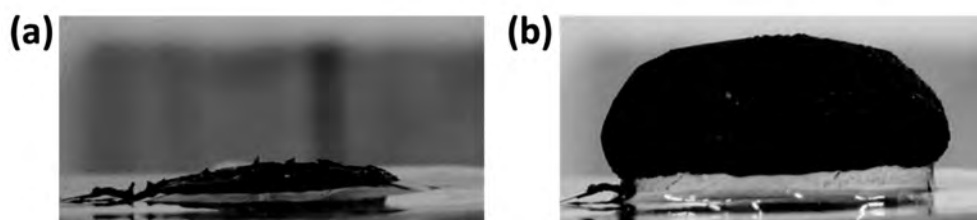


**Figure 1.5** | An interpenetrating network of VHB 4910 and poly(1,6-hexanediol diacrylate). (a) No voltage is applied on the film, however air pressure in the diaphragm chamber keeps the film under some tension. (b) After applying an electric field of  $300 \text{ V}/\mu\text{m}$ , the surface area expands and balloons out. Reproduced from reference 57.

strain.<sup>[56]</sup> For applications in artificial muscles, VHB 4910 has been studied in an interpenetrating network with poly(1,6-hexanediol diacrylate).<sup>[57]</sup> At a concentration of 18.3 wt%, the poly(1,6-hexanediol diacrylate) can lock pre-strain up to 275 % while allowing electrically induced strains of up to 233 % (Figure 1.5).

### 1.4.2 Silicones

Silicones are, just like acrylates, a material that is widely studied for its application as dielectric elastomers.<sup>[59–67]</sup> The largest advantages of silicone over acrylate are its high stability of a wide temperature range, faster response speed and high efficiency.<sup>[59,60]</sup> In 2010 Michel et al.<sup>[61]</sup> made a comparison between the acrylic elastomer film from 3M VHB 4910 and a Dow Corning silicone (DC 3481). The silicone DC 3481 displays a constant elasticity over the temperature range  $-25$  to  $150 \text{ }^\circ\text{C}$ . Electromechanical tests show that the silicone has a response time of 3 seconds to reach an activation strain of 8.5 %. The acrylic VHB 4910 has constant elasticity over the range from  $25$  to  $75 \text{ }^\circ\text{C}$ . And its response time is long with creep processes still occurring during its actuation after more than 100 seconds. The comparison makes it clear that silicone DC 3481 is the better choice when a fast response time is preferred over high strains ( $<10 \%$ ). Although their strain rates are smaller, many options are still available for the improvement of electromechanical actuation performances of silicone dielectric elastomers. Just like acrylic elastomers, the silicones can be subjected to pre-stretching to increase

the dielectric breakdown strength<sup>[62]</sup> or lower the Young's modulus.<sup>[63]</sup> Other options involve the addition of inorganic microparticles like titanium dioxide,<sup>[64]</sup> lead magnesium niobite<sup>[65]</sup> or magnesium-doped calcium copper titanate,<sup>[66]</sup> which increases the dielectric constant. In our research we aim for high-speed deformations and precise control over modulus in the range of 100 kPa to 10 MPa. For these reasons, we decided to use silicones to create dynamic surfaces topographies. Still, the principles we describe in this thesis might also be applied effectively using alternative materials.

## **1.5 Dynamic surfaces in dielectric elastomer coatings**

The previous paragraph focused on field-induced dimensional changes of dielectric films as a whole, resulting in thickness changes of the film coupled, through the Poisson ratio, to changes in length and width. Applying dielectric elastomers in coatings to obtain dynamic surfaces brings about a whole new challenge: dealing with the mechanical constraint of the rigid substrate which prohibits the global in-plane displacement. Because of this constraint, equation 3 is no longer valid, as the free boundary conditions are not met. Two different methods can be used to deal with this restriction. One method is by applying the Maxwell stresses locally rather than over the entire surface of the coating. This method usually involves some form of patterning of the electrodes, for example by using a percolating network of metallic nanowires as a top electrode rather than the conventional continuous electrodes.<sup>[26]</sup> In this case the surface is deformed by the displacement of the charged nanowires towards the oppositely charged indium tin oxide (ITO) coated glass substrate (Figure 1.6). The overall volume of the elastomer is conserved as the elastomer moves away from the nanowires rather than being compressed. The displacement of the elastomer surfaces varies spatially due to the inhomogeneous distribution of the randomly dispersed nanowires. At high electrical field strengths of up to 130 V/ $\mu\text{m}$ , light is

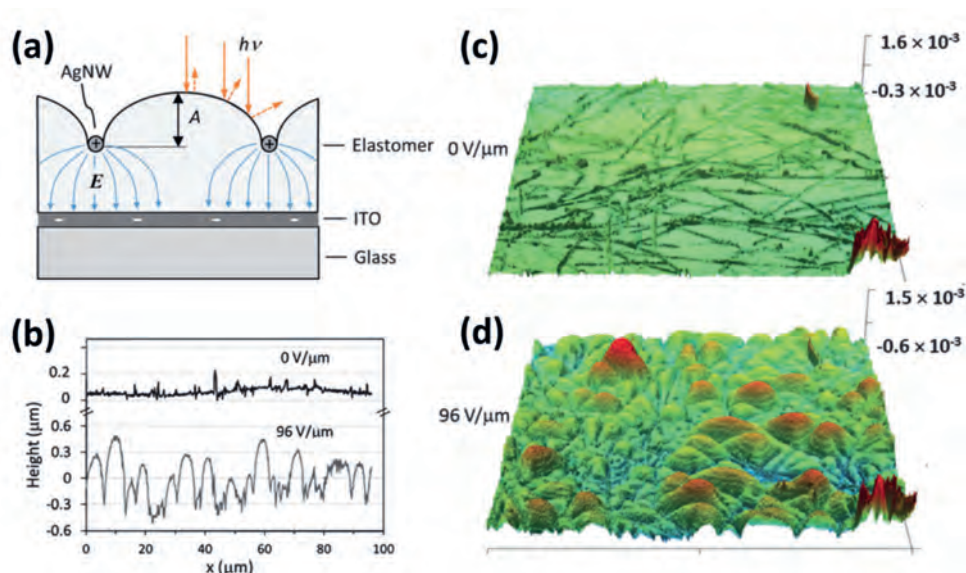


**Figure 1.6 |** (a) A schematic cross-section of the surface displacements and the electric field emanating from individual nanowires. (b) Line profiles that show the change in surface morphology when the electric field is applied. (c) Confocal microscopy maps of the nanowire electrode and elastomer surface without the electric field. (d) Confocal microscopy maps of the nanowire electrode and elastomer surface at an applied electric field of  $96 \text{ V}/\mu\text{m}$ . Reproduced from reference 26.

strongly scattered by the surface undulations which might be useful in applications like tunable privacy windows.

The second method to deal with the constraints of a rigid substrate, and the incompressibility of the dielectric, is by incorporating collapsible pockets of air into the dielectric elastomer material to which the compressed material can escape. Such pockets of air can be incorporated by sandwiching a flexible dielectric elastomer layer with a monolithic pyramidal geometry between two parallel polyethylene terephthalate (PET) films with ITO electrodes.<sup>[68]</sup> As soon as a potential of 3 kV is applied to the ITO electrodes, the electrostatic attraction force compresses the parallel-arranged micro-structures, which store the elastic energy similar to a compressed spring (Figure 1.7). Although no surface topographies are created in this process, a vibrational output in the human-sensitive frequency range (100-200 Hz) of perception can be obtained by applying a sinusoidal voltage.<sup>[69–71]</sup> The resonance frequency of the system can be

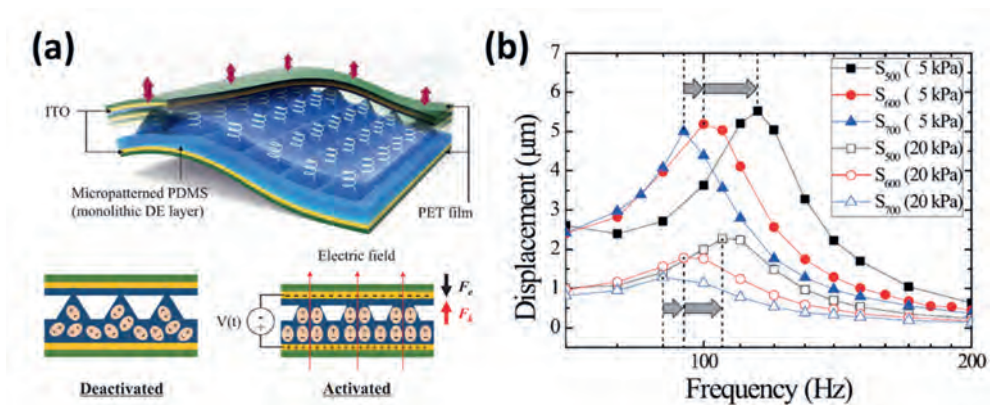


**Figure 1.7** | (a) Schematic illustrations of the structural configuration and operating principle of a micro-structured dielectric elastomer actuator. The micro-structures behave like a spring and allow for a vibrational response. (b) The displacement of the surface for various spatial distances between the pyramids (500, 600 and 700  $\mu\text{m}$ ), and at two different pressures. Reproduced from reference 68.

influenced by the spatial distance between the micro-pyramids as well as by the applied external pressure. Other methods to incorporate an air pocket underneath the surface of the coating involve the mounting of the dielectric film on pillars at the edges of the sample, similar to a small drum.<sup>[72]</sup> The dielectric material consists of polyurethane mixed with conductive polymers and at potentials up to 2 kV, a vibrational response is obtained with frequencies up to 400 Hz.

From these examples we can conclude that several issues need to be addressed before dielectric elastomer coatings with dynamic surface topographies can be applied in existing devices. First, the driving potential and applied electrical fields should be lowered to reduce the risk for potential users and prevent breakdown events. Second, the shape of the surface deformation needs to be controlled and not randomly generated to open options for more applications. Third, the incorporation of air pockets underneath the surface should be considered when generating dynamic topographies, rather than just vibrating surfaces. Fourth, the frequency range at which the surface dynamics take place can still be increased which expands the range of applications to, for instance acoustics and communication optics. Before we rise to the challenge, we first discuss the aim and outline of this thesis.

## 1.6 Aim and outline of this thesis

This thesis reports on the characterization, potential applications and various approaches to generate dynamic surface topographies in poly(dimethyl siloxane) coatings by applying electric fields. Dynamic surface topographies have already been extensively studied in LCN coatings as discussed in section 1.2. The advantage of the LCNs is that the shape of the surface deformation is easily programmable while being responsive to a large variety of different stimuli. Some of the few limits of these coatings are their response time, which is usually around 10 seconds, and their costs. Our challenge is to create dynamic surface topographies that respond quickly to an electrical stimulus, while overcoming the issues mentioned in section 1.5. Furthermore, we aim to provide full control over parameters like amplitude, frequency, shape and start- and stop-times. Finally, we also aim to provide an in-depth explanation and deep understanding of the mechanisms that drive the surface deformations.

Chapter 2 proposes a new method to generate oscillating waves in soft polymer networks under a continuous AC electric field. The material consists of a poly(dimethyl siloxane) layer reinforced with a 10 nm thick silicon oxide top layer. With a novel integrated tri-electrode structure, the viscoelastic properties of the material are exploited to bring the initially flat surface into a self-sustaining oscillatory motion, without the use of an intermittent on-off switch. After activation, the surface quickly returns to its original flat shape.

Chapter 3 provides more insight into the deformation mechanics by providing finite element method simulations of the previously described system. The nonlinear finite element software of Marc Mentat is used with a coupled electrostatic-structural analysis. We compare the simulated results to our experimentally obtained data and elucidate how the material moves within our coating. Furthermore, the model can be employed to predict the outcome of future experiments



Chapter 4 explores methods to program the shape of the dynamic surface topographies. First, we determine the effect of different electric circuits on the shape of the oscillating surface waves. Next, we again employ finite element modeling to change and optimize the shape of the surface wave with different electrode patterns. The results from these simulations are confirmed experimentally, revealing the different types of oscillating surface waves that can be created.

Chapter 5 shows how electrode structures can be modified further to add desired complexity to the deformation patterns in electroactive polymer coatings. The complex deformation figures are predicted with finite element modelling and subsequently confirmed with experimental results. The optical effects that result from the change in surface texture are demonstrated.

Chapter 6 presents a new method to create high-frequency surface dynamics using a tougher coating that consists of a densely crosslinked elastic poly(dimethyl siloxane) network, supported by SU-8 microstructures. At the resonance frequency, the elastic film covering microscopically small air-pockets vibrates locally with significantly increased amplitudes and speeds.

Chapter 7 provides a technology assessment where we discuss the impact of the research, along with future challenges and potential applications.

## 1.7 References

- [1] R. Fürstner, W. Barthlott, C. Neinhuis, P. Walzel, *Langmuir* **2005**, *21*, 956.
- [2] C. Neinhuis, W. Barthlott, *Ann. Bot.* **1997**, *79*, 667.
- [3] L. Q. Ren, S. J. Wang, X. M. Tian, Z. Q. Han, L. N. Yan, Z. M. Qiu, *J. Bionic Eng.* **2007**, *4*, 33.
- [4] Y. Tian, N. Pesika, H. Zeng, K. Rosenberg, B. Zhao, P. McGuiggan, K. Autumn, J. Israelachvili, *Proc. Natl. Acad. Sci. U. S. A.* **2006**, *103*, 19320.
- [5] H. C. Hoch, R. C. Staples, B. Whitehead, J. Comeau, E. D. Wolf, *Science*. **1987**, *235*, 1659.
- [6] L. B. Pérez-Estrada, Z. Cano-Santana, K. Oyama, *Tree Physiol.* **2000**, *20*, 629.
- [7] G. Kerstiens, *J. Exp. Bot.* **1996**, *47*, 1813.
- [8] K. Koch, B. Bhushan, W. Barthlott, *Soft Matter* **2008**, *4*, 1943.
- [9] Y. Lu, S. Sathasivam, J. Song, C. R. Crick, C. J. Carmalt, I. P. Parkin, *Science*. **2015**, *347*, 1132.
- [10] K. Liu, L. Jiang, *Annu. Rev. Mater. Res.* **2012**, *42*, 231.

- [11] S. Nishimoto, B. Bhushan, *RSC Adv.* **2013**, *3*, 671.
- [12] A. K. Geim, S. V. Dubonos, I. V. Grigorieva, K. S. Novoselov, A. A. Zhukov, S. Y. Shapoval, *Nat. Mater.* **2003**, *2*, 461.
- [13] M. Sitti, R. S. Fearing, *J. Adhes. Sci. Technol.* **2003**, *17*, 1055.
- [14] J. Davies, S. Haq, T. Hawke, J. P. Sargent, *Int. J. Adhes. Adhes.* **2009**, *29*, 380.
- [15] G. McHale, M. I. Newton, N. J. Shirtcliffe, *Soft Matter* **2010**, *6*, 714.
- [16] F. Wang, F. Lv, Y. Liu, C. Li, Y. Lv, *J. Adhes. Sci. Technol.* **2013**, *27*, 58.
- [17] V. Zorba, X. Chen, S. S. Mao, *Appl. Phys. Lett.* **2010**, *96*, 3.
- [18] W. L. Min, B. Jiang, P. Jiang, *Adv. Mater.* **2008**, *20*, 3914.
- [19] Z. Dang, L. Liu, Y. Li, Y. Xiang, G. Guo, *ACS Appl. Mater. Interfaces* **2016**, *8*, 31281.
- [20] G. Babakhanova, H. Yu, I. Chaganava, Q. H. Wei, P. Shiller, O. D. Lavrentovich, *ACS Appl. Mater. Interfaces* **2019**, *11*, 15007.
- [21] D. Liu, D. J. Broer, *Angew. Chemie Int. Ed.* **2014**, *53*, 4542.
- [22] Q. Hao, W. Li, H. Xu, J. Wang, Y. Yin, H. Wang, L. Ma, F. Ma, X. Jiang, O. G. Schmidt, P. K. Chu, *Adv. Mater.* **2018**, *30*, 1.
- [23] B. Wang, X. Xue, X. Liu, P. Neuzžil, B. Ma, W. Yuan, J. Luo, C. Jiang, *Appl. Mater. Today* **2018**, *13*, 271.
- [24] D. Liu, N. B. Tito, D. J. Broer, *Nat. Commun.* **2017**, *8*, 1.
- [25] W. Feng, D. J. Broer, D. Liu, *Adv. Mater.* **2018**, *1704970*, 1.
- [26] S. Shian, D. R. Clarke, *Soft Matter* **2016**, *12*, 3137.
- [27] R. Eelkema, M. M. Pollard, J. Vicario, N. Katsonis, B. S. Ramon, C. W. M. Bastiaansen, D. J. Broer, B. L. Feringa, *Nature* **2006**, *440*, 163.
- [28] M. E. Sousa, D. J. Broer, C. W. M. Bastiaansen, L. B. Freund, G. P. Crawford, *Adv. Mater.* **2006**, *18*, 1842.
- [29] G. Babakhanova, T. Turiv, Y. Guo, M. Hendrikx, Q.-H. Wei, A. P. H. J. Schenning, D. J. Broer, O. D. Lavrentovich, *Nat. Commun.* **2018**, *456*, 1.
- [30] Y. Guo, M. Jiang, C. Peng, K. Sun, O. Yaroshchuk, O. Lavrentovich, Q.-H. Wei, *Adv. Mater.* **2016**, *28*, 2353.
- [31] D. Yang, L. H. He, *Smart Mater. Struct.* **2014**, *23*, 1.
- [32] D. Yang, L. H. He, *Acta Mech. Sin. Xuebao* **2015**, *31*, 672.
- [33] C. Fu, F. Xu, Y. Huo, *Int. J. Solids Struct.* **2017**, *132–133*, 264.
- [34] A. Agrawal, P. Luchette, P. Palffy-Muhoray, S. L. Biswal, W. G. Chapman, R. Verduzco, *Soft Matter* **2012**, *8*, 7138.
- [35] S. H. Kang, J. H. Na, S. N. Moon, W. Il Lee, P. J. Yoo, S. D. Lee, *Langmuir* **2012**, *28*, 3576.
- [36] G. S. Kumar, D. C. Neckers, *Chem. Rev.* **1989**, *89*, 1915.
- [37] C. D. Eisenbach, *Polym. (United Kingdom)* **1980**, *21*, 1175.
- [38] J. Algers, P. Sperr, W. Egger, L. Liskay, G. Kögel, J. De Baerdemaeker, F. H. J. Maurer, *Macromolecules* **2004**, *37*, 8035.
- [39] C. L. Van Oosten, C. W. M. Bastiaansen, D. J. Broer, *Nat. Mater.* **2009**, *8*, 677.
- [40] T. J. White, S. V. Serak, N. V. Tabiryan, R. A. Vaia, T. J. Bunning, *J. Mater. Chem.* **2009**, *19*, 1080.
- [41] M. Camacho-Lopez, H. Finkelmann, P. Palffy-Muhoray, M. Shelley, *Nat. Mater.* **2004**, *3*, 307.
- [42] J. S. Evans, P. J. Ackerman, D. J. Broer, J. van de Lagemaat, I. I. Smalyukh, *Phys. Rev. E - Stat. Nonlinear, Soft Matter Phys.* **2013**, *87*, 1.
- [43] H. Yu, C. Dong, W. Zhou, T. Kobayashi, H. Yang, *Small* **2011**, *7*, 3039.
- [44] Z. Yan, X. Ji, W. Wu, J. Wei, Y. Yu, *Macromol. Rapid Commun.* **2012**, *33*, 1362.
- [45] D. Liu, C. W. M. Bastiaansen, J. M. J. den Toonder, D. J. Broer, *Angew. Chemie Int. Ed.* **2012**,

- 51, 892.
- [46] M. Hendrikx, A. P. H. J. Schenning, D. J. Broer, *Soft Matter* **2017**, *13*, 4321.
- [47] Y. Yu, M. Nakano, T. Ikeda, *Nature* **2003**, *425*, 145.
- [48] N. America, B. C. Burchfiel, P. W. Lipman, T. Parsons, G. Soc, A. Bull, A. Tovish, G. Schubert, B. P. Luyendyk, R. Pelrine, R. Kornbluh, Q. Pei, J. Joseph, *Science* **2000**, *287*, 836.
- [49] R. E. Pelrine, R. D. Kornbluh, J. P. Joseph, *Sensors Actuators, A Phys.* **1998**, *64*, 77.
- [50] Y. Bar-Cohen, Q. Zhang, *MRS Bull.* **2008**, *33*, 173.
- [51] J. Biggs, K. Danielmeier, J. Hitzbleck, J. Krause, T. Kridl, S. Nowak, E. Orsell, X. Quan, D. Schapeler, W. Sutherland, J. Wagner, *Angew. Chemie - Int. Ed.* **2013**, *52*, 9409.
- [52] L. J. Romasanta, M. A. Lopez-Manchado, R. Verdejo, *Prog. Polym. Sci.* **2015**, *51*, 188.
- [53] R. Pelrine, R. Kornbluh, *Dielectric Elastomers as Electromechanical Transducers: Fundamentals, Materials, Devices, Models and Applications of an Emerging Electroactive Polymer Technology*; Carpi, F.; Rossi, D. De; Kornbluh, R.; Pelrine, R.; Sommer-Larsen, P., Eds.; Elsevier Ltd, 2008.
- [54] R. Pelrine, R. Kornbluh, Q. Pei, J. Joseph, *Science* **2000**, *287*, 836.
- [55] G. Kofod, P. Sommer-Larsen, R. Kornbluh, R. Pelrine, *J. Intell. Mater. Syst. Struct.* **2003**, *14*, 787.
- [56] J. Huang, S. Shian, R. M. Diebold, Z. Suo, D. R. Clarke, *Appl. Phys. Lett.* **2012**, *101*.
- [57] S. M. Ha, W. Yuan, Q. Pei, R. Pelrine, S. Stanford, *Adv. Mater.* **2006**, *18*, 887.
- [58] W. Hu, S. N. Zhang, X. Niu, C. Liu, Q. Pei, *J. Mater. Chem. C* **2014**, *2*, 1658.
- [59] R. D. Kornbluh, R. Pelrine, J. Joseph, R. Heydt, Q. Pei, S. Chiba, *Smart Struct. Mater. 1999 Electroact. Polym. Actuators Devices* **1999**, *3669*, 149.
- [60] X. Zhang, M. Wissler, B. Jaehne, R. Breonmann, G. Kovacs, *Smart Struct. Mater. 2004 Electroact. Polym. Actuators Devices* **2004**, *5385*, 78.
- [61] S. Michel, X. Q. Zhang, M. Wissler, C. Löwe, G. Kovacs, *Polym. Int.* **2010**, *59*, 391.
- [62] D. Gatti, H. Haus, M. Matysek, B. Frohnafel, C. Tropea, H. F. Schlaak, *Appl. Phys. Lett.* **2014**, *104*.
- [63] S. Zakaria, L. Yu, G. Kofod, A. L. Skov, *Mater. Today Commun.* **2015**, *4*, 204.
- [64] F. Carpi, D. De Rossi, *IEEE Trans. Dielectr. Electr. Insul.* **2005**, *12*, 835.
- [65] D. Yang, L. Zhang, H. Liu, Y. Dong, Y. Yu, M. Tian, *J. Appl. Polym. Sci.* **2012**, *125*, 2196.
- [66] L. Duan, G. L. Wang, Y. Y. Zhang, Y. N. Zhang, Y. Y. Wei, Z. F. Wang, M. Zhang, *Polym. Compos.* **2018**, *39*, 691.
- [67] F. B. Madsen, L. Yu, A. L. Skov, *ACS Macro Lett.* **2016**, *5*, 1196.
- [68] D. Pyo, S. Ryu, K. U. Kyung, S. Yun, D. S. Kwon, *Appl. Phys. Lett.* **2018**, *112*, 1.
- [69] K. O. Johnson, *Curr. Opin. Neurobiol.* **2001**, *11*, 455.
- [70] H. U. Ko, H. Chan Kim, J. Kim, S. Y. Kim, *Smart Mater. Struct.* **2015**, *24*.
- [71] M. Morioka, M. J. Griffin, *Somatosens. Mot. Res.* **2005**, *22*, 281.
- [72] W. H. Park, T. H. Yang, Y. Yoo, S. Choi, S. Y. Kim, *IEEE World Haptics Conf. WHC 2015* **2015**, 165.

# Chapter 2

## Oscillating surfaces fueled by a continuous AC electric field

---

This chapter is partially reproduced from: 'Oscillating surfaces fueled by a continuous AC electric field' F.L.L. Visschers, H. Gojzewski, G.J. Vancso, D.J. Broer, D. Liu, *Adv. Mater. Interfaces*, 2019, 1901292.

## 2.1 Introduction

Responsive shape-changing materials have attracted recent attention, varying from shape-memory materials delivering a single-time deformation in response to a trigger (often temperature) to stimuli-responsive materials that respond reversibly to a trigger (often temperature, light or pH).<sup>[1–9]</sup> However, until present the fabrication of oscillating materials that dynamically alter their shape upon a continuous flow of energy or “chemical fuels” is still in infancy. These materials could lead to functions such as peristaltic gas pumping through membranes or controlled movement of molecules or particles at surfaces. Only a very limited number of such materials is known, which shows great potential for new developments on one hand, but also shows the challenges that have to be overcome to bring them to the prospective level of sophistication.<sup>[10,11]</sup>

So far, the most successful example for autonomous movement of materials is based on the Belousov-Zhabotinsky (BZ) reaction generating chemical oscillations used in gels.<sup>[10,12,13]</sup> The first biomimetic gel with an autonomous self-oscillating function, resembling heart muscles, was developed by Yoshida et al. in 1996. The self-oscillating polymer is composed of a poly(*N*-isopropylacrylamide) network in which the catalyst for the BZ reaction is covalently immobilized.<sup>[14,15]</sup> The other example known in literature is an oscillating beam of a laser-powered azobenzene-modified liquid crystal network (LCN).<sup>[16]</sup> The mechanical coupling of momentum and directional addressing leads to a fast oscillation. Clamped at one side, the beam oscillates with its eigenfrequency between 5 and 100 Hz depending on its dimension, normally a few millimeters. Despite the beauty of these examples, they still lack the appropriate set of properties to become implemented in practical applications. For instance, the BZ reaction is limited to very soft materials in the presence of water. And the oscillating beam is limited to thin and dimension-limited free-standing films. For further progress in this promising field of materials science, new approaches are needed.

Here, we propose an approach to generate an oscillating wave in a soft polymer coating consisting of loosely crosslinked poly(dimethyl siloxane) (PDMS) under a continuous AC electric field. The surface motilities demonstrated may lead to a plurality of potential applications, such as self-cleaning, adjustable tribology, de-icing, haptics and motile transport of species.

## 2.2 Results and discussion

Surface deformation is produced by a periodic electrostatic attraction based on Maxwell stresses. Maxwell stresses are well known and extensively studied and applied for the actuation of electroactive polymers (see chapter 1).<sup>[17–22]</sup> Generally, a two-plate capacitor configuration is established where a thin elastomeric film is coated at both sides with flexible electrodes. By applying an electric field, the electrostatic attraction between the electrodes causes the polymer film to contract in thickness while expanding in the lateral direction.<sup>[23,24]</sup> We expanded on this concept and trigger the Maxwell stresses locally on a thin crosslinked film firmly adhering to a rigid substrate (Figure 2.1a). When the coating is compressed, the global in-plane displacement is prohibited by the rigid substrate. However, locally we create lateral escape routes of the compressed excess of volume by adjacent expanding areas (Figure 2.1c). This is achieved by employing patterned bottom electrodes (E1) made by conventional lithographic procedures. On top of E1, we created a coating consisting of the ultra-soft PDMS polymer network, provided with an 11 nm silicon oxide top film. The PDMS consists of a poly(dimethyl siloxane) decorated with reactive vinyl groups, which is crosslinked by platinum catalyzed hydrosilylation reaction by a Si-H groups containing siloxane curing agent. The elastic modulus of the material, measured by AFM in the PeakForce Quantitative Nanomechanical Mapping (QNM) mode, varies from  $\sim 2.1$  to  $\sim 0.3$  MPa with decreasing amount of the curing agent from 10% to 2%. The silicon oxide top layer is obtained by UV/ ozone treatment of the PDMS.<sup>[25,26]</sup> When applied on a film containing 2% curing agent, this treatment increases the sample

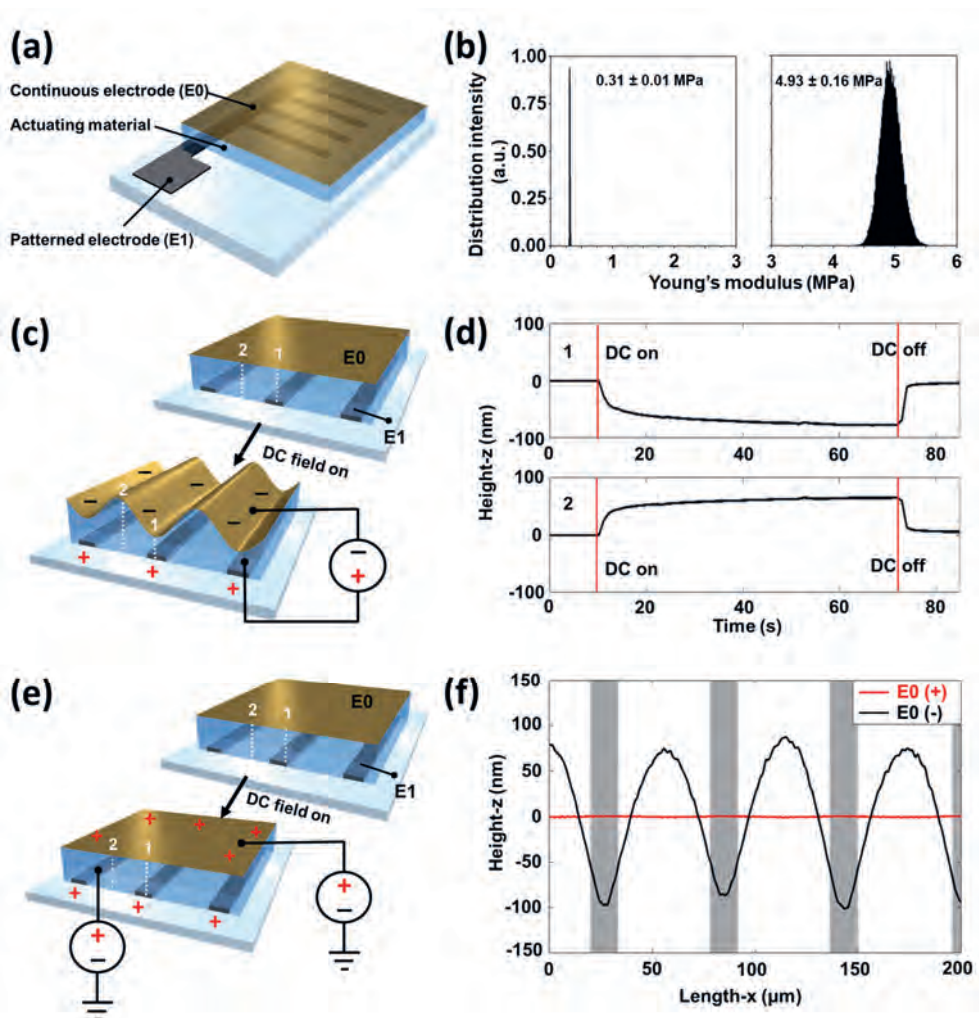


**Figure 2.1** | Design principle of coatings that generate surface waves by applying an electric field. (a) Schematic representation of the device configuration. (b) The AFM modulus of PDMS coatings with 2% curing agent before (left) and after (right) the UV/ ozone treatment. (c) Schematic illustration of the Maxwell effect confined to a coating. (d) Measured formation and relaxation of the surface deformation at two adjacent areas. Vertical red lines indicate the moment that the voltage is switched on and off. (e) Illustration of top and bottom electrodes both connected to an electric field of the same polarity. (f) Measured 2D surface profile when E0 reverses its polarity. The applied DC potential is 150 V. The gray blocks in the background indicate the position of the electrode (E1).

surface elastic modulus from 0.3 MPa to 4.9 MPa (Figure 2b). On top of the silicon oxide layer, a compliant second gold electrode (E0) is coated. Details of the device dimensions and the process are provided in section 2.4. The combination of the gold top electrode and the silicon oxide provides the

robustness needed but is still flexible enough to deform together with the polymer coating. To initiate surface waves, E0 and E1 are supplied with an electric field with opposite polarity (Figure 2.1c), typically the voltage is 150 V. We demonstrate the proposed actuation principle by monitoring the time-resolved electro-mechanic response of the coating by digital holographic microscopy (DHM) at two adjacent locations (Figure 2.1d). Location 1 is activated by the Maxwell stress which leads to a negative surface deformation. Location 2 is inactive and directly connects to location 1. Although location 2 was not subjected to an electric field, we measured a surface expansion that is of the same order as observed for the contraction, which is caused by the mechanical stress-strain from contraction at the connecting areas (location 1). Keeping E1 and E0 at the same polarity of 150V (Figure 2.1e), there is no potential established suggesting a zero electrostatic compression or expansion. The kinetic measurements as carried out under isothermal conditions reveal that there is no electrostatic repulsion to expand the coating. Subsequently, by reversing the polarity of E0, we create a coating whose surface transfer from flat to the corrugated state (Figure 2.1f)

Building further on this idea, surface waves are brought into oscillation under a continuous AC electric field. The principle of generating oscillating standing waves is based on spatially periodic and continuous polarity inversion in the viscoelastic dielectric coating. Based on the device configuration given in Figure 2.1a, we created two patterned indium tin oxide (ITO) interdigitated bottom electrodes E1 and E2 (Figure 2.2a). During activation, the tri-electrode structures are simultaneously provided with electric signal. The polymer film functions as two individual capacitors provided by a continuous electrode and two discrete electrodes as illustrated by the circuit (Figure 2.2b). The patterned electrodes (E1, E2) are supplied with a direct electric field (DC) with opposite polarity. An alternating electric field (AC) is applied on the continuous top electrode (E0) and thus E0 repeatedly inverses its polarity. During activation E1 and E0 can have opposite charges while E2 and E0 have equal charges. A potential is thus built between E1 and E0, which is indicated as  $\Delta V_1$ , while between E2 and E0 the



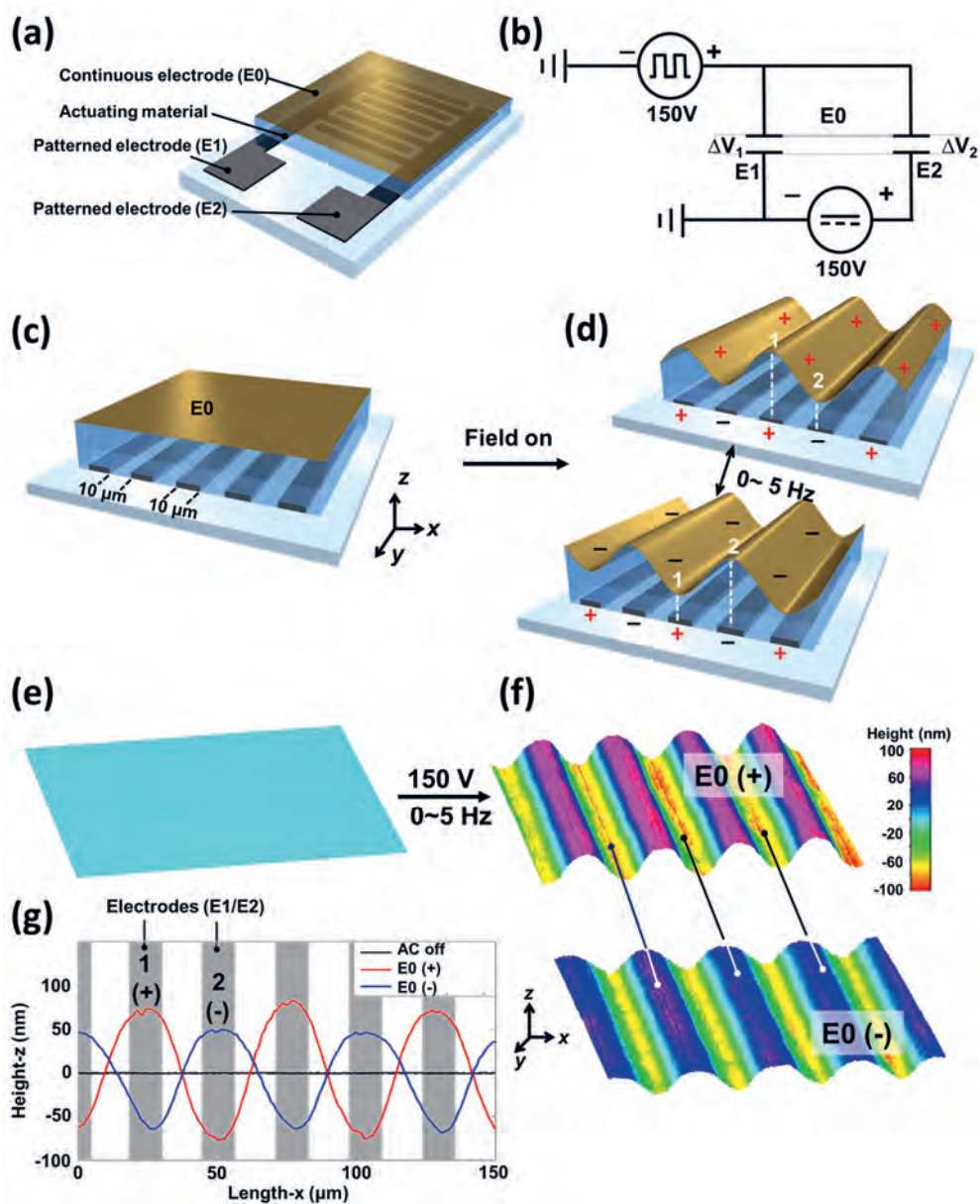


**Figure 2.2** | (a) Schematic representation of the device configuration. (b) Equivalent electric circuit of the tri-electrode driving scheme. The activated polymer works as a double capacitor when placed in the external electric field. (c) Illustration of the initial surface and (d) the actuation principle based on the inversion of polarity in the dielectric elastomeric coating. (e) 3D images measured by DHM show the initial flat surface without electric field. (f) With an alternating electric field, the surface oscillates. (g) The corresponding 2D profile is extracted from the DHM measurement. The black curve is the surface profile without electric field. Red and blue curves are measured when the electric field is applied showing the wave oscillates in time. The gray blocks indicate the position of electrodes (E1/E2).

potential is zero ( $\Delta V_2$ ). As a consequence, the Maxwell stress compresses the polymer film between E1 and E0 via  $\Delta V_1$ , simultaneously, because of conservation of the volume the adjacent area (between E2 and E0) expands. As a result, a sinusoidal wave appears at the coating surface. This is accompanied by a strain in the silicon oxide-gold top layer as the surface area continuously expands and relaxes. By flipping the polarity of E0, the wave reverses its peaks and valleys (Figures 2.2d and 2.2e). The oscillation frequency is thus governed by the electric signal applied to E0.

The oscillating standing wave is characterized by DHM. The profile of the wave, as well as its corresponding oscillation kinetics, is extracted from the measurement. Before actuation, the coating surface is flat and smooth and does not change with time (Figures 2.2e and 2.2g (black curve)). Upon applying the electric field, the surface corrugates into a sinusoidal wave and oscillates temporally following the alternating electric field (Figures 2.2f and 2.2g). Typically, both DC and AC power sources supply 150 V to generate the electric field. The peak-to-peak voltage value of the AC field is measured and is further denoted as  $V_{PP}$ . Under this applied potential, the wave exhibits a peak-to-valley height difference of 150 nm on top of an 8  $\mu\text{m}$  coating.

Taking a closer look at the oscillating wave, we discovered a deformation asymmetry when the polarity of E0 switches from positive to negative. To be more specific, the height difference between points 1 and 2 is 30% larger when E0 is positive than when E0 is negative. To solve the origin of this height difference, we investigated the influence of the in-plane electric field on the deformation profile. By applying a DC electric field across electrodes E1 and E2, we observe a small surface relief of 50 nm, in which the material above the positive electrode (1) forms a peak while at the location above the negative electrode (2) the material forms a valley (Figures 2.3a and 2.3b). We attribute this phenomenon to an ionic impurity possibly from the platinum catalyst in the curing agent of the PDMS, in which the negatively charged material accumulates

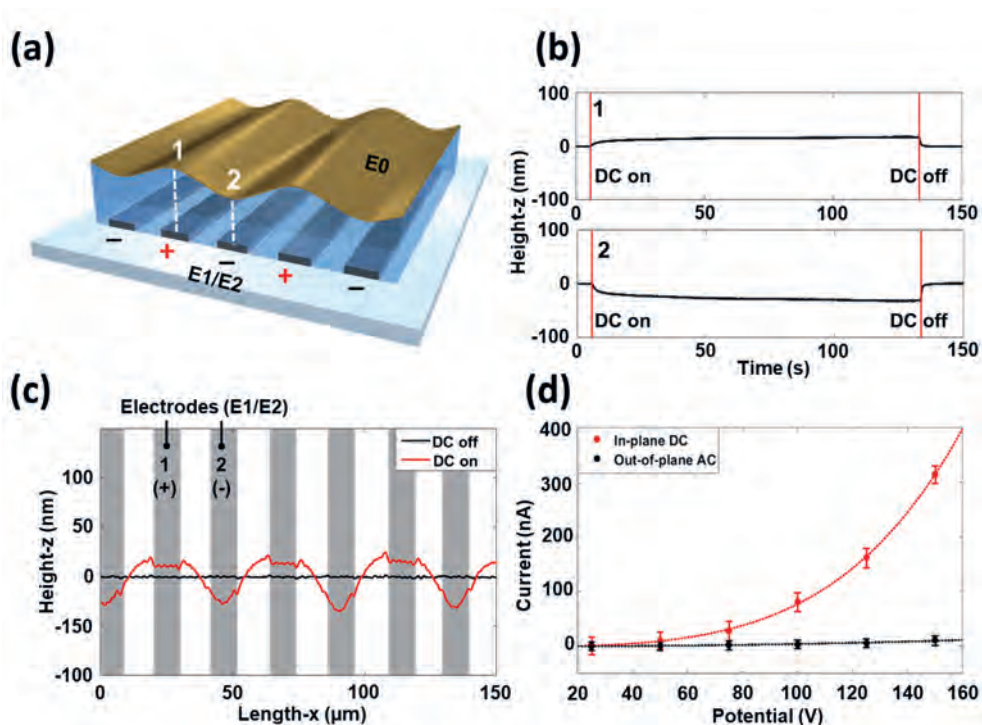


**Figure 2.3** | (a) Schematic representation of a minor surface relief produced by an in-plane DC electric field provided by the electrodes E1 and E2. (b) Measured change of the surface height on top of the positive and negative electrodes respectively. (c) The 2D profile of the surface relief created by the in-plane potential, measured by DHM. (d) Current through the PDMS coating measured both in-plane (red) and out-of-plane (black) in a tri-electrode driving scheme.

at the positive electrode. The shape of the relief is not as smooth as found for the tri-electrode system (Figure 2.3c). This odd shape is influenced by the electric field, which is smaller in the areas above the electrodes than in the areas above the gaps. Consequently, any charged material will prefer to move towards the gap, resulting in a slight reduction of the height above the electrodes. This effect will also contribute to the small elevations ('ears') appearing at the sides of each hill. Furthermore, the migration of charges is confirmed by measuring an in-plane current which has a value of 315 nA at 150 V (Figure 2.3d). In comparison, the out-of-plane current in the tri-electrode driving scheme reaches a value of only 12 nA at the same applied potential.

To gain more insight into the deformation mechanics, we measured the amplitude values of the surface wave as a function of the applied electric field strength (Figure 2.4a). This response can be intuitively understood in terms of the larger Maxwell stress exerted on the coating with increasing field strength (Equation 2). The indentation leads to an expansion in the adjacent area due to volume conservation forming a protrusion. The deformation amplitude is then calculated as the height difference between the valley and the peak and scales with the quadratic of the applied voltage. The mechanical properties of the PDMS also influence the deformation (Figure 2.4b). The deformation scales inversely with the modulus. At a modulus above 1 MPa, barely any deformation occurs. This observation is explained by a larger resistance against lateral displacement at higher moduli. Next, we investigate the oscillating behavior of the standing wave in terms of the viscoelastic behavior of the soft PDMS. We randomly select two adjacent areas above the electrodes as indicated in Figure 2.2d and trace their relative height changes under the continuous electric field input in time (Figure 2.4c). The polarity of  $E_0$  reverses every 500 ms, as indicated by vertical red lines. In response to this change, the surface of the coating inverts its original topography. The inversion begins with a rapid elastic-like deformation, followed by a gradual change as controlled by viscoelastic properties. Despite the viscous component, the maximum protrusion height is obtained within 100 ms after switching the polarity of  $E_0$ , corresponding to a vertical displacement speed of 5  $\mu\text{m/s}$  (Figure 2.4d). In comparison, the surface deformation of coatings in other systems generally requires 10 s or more.<sup>[27–29]</sup> We then monitor the deformation amplitude during a frequency sweep (Figure 2.4e). The results indicate that at a frequency above 5 Hz, the deformation amplitude decreases rapidly. The oscillatory mechanical frequency sweep (Figure 2.4f), reveals that  $\tan(\delta) > 1$  at a frequency of 5 Hz. Above this frequency, the value of the loss modulus exceeds the storage modulus indicating that the energy dissipation by the viscous component of the material starts to dominate. As a result, the strain can no longer keep up with the applied stresses.

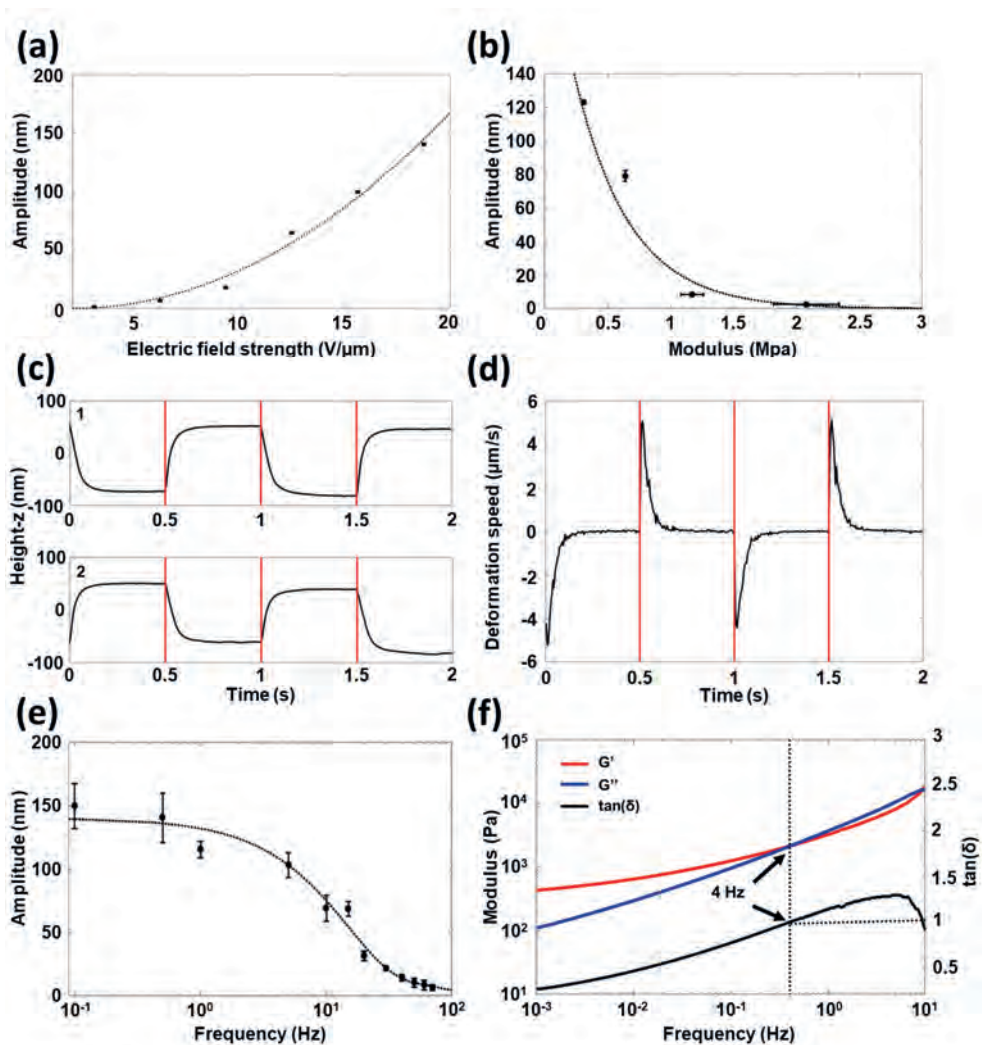


**Figure 2.4 |** Details of influential parameters on the oscillation of the wave. (a) Influence of the electric field strength on the deformation amplitude. (b) Influence of the material's modulus on the deformation. (c) Dynamics of the height change at a frequency of 1 Hz. Red lines indicate when  $E0$  inverts its polarity. (d) The speed at which the surface topographies switch as a function of time. (e) Influence of the frequency on the deformation amplitude. (f) Measured storage modulus  $G'$ , loss modulus  $G''$ , and  $\tan(\delta)$  when the coating is subjected to a frequency sweep at 6% strain.

The energy consumption of the surface dynamics is determined by measuring the in-plane (315 nA) and out-of-plane (12 nA) current values at a potential of 150 V (Figure 2.3d). Considering also the surface area of our sample (1 cm<sup>2</sup>), remarkably low energy consumption of 168 mW m<sup>-2</sup> is required to bring the surface to a mechanical oscillation. In comparison, electrically responsive LCN surface

topographies require about  $90 \text{ W m}^{-2}$  and UV responsive LCN coatings  $2\text{-}7 \text{ kW m}^{-2}$ , almost five orders of magnitude higher.<sup>[27,29,30]</sup>

## 2.3 Conclusions

In conclusion, we describe a method to generate oscillation in complex motion figures such as waves in a thin solid coating triggered by a continuous AC field. In this new approach, surface deformation is achieved by localized periodic electrostatic attraction based on Maxwell stresses. Our innovation is that a tri-electrode configuration is designed to initiate the oscillation. We demonstrate that the waves can be brought into motion at a frequency up to 5 Hz. This value is significantly larger than that of, for instance, LCN coatings which is generally in the range of 0.05 Hz. We envision that this newly proposed fast oscillating wave can be used for haptic applications, such as human-machine interface, refreshable braille display as well as used to interact with the environment, for instance, transporting materials and particles, mechanically de-icing through surface vibrations, and regulating light. For many of the practical applications we need to optimize the coating further, e.g., isolating or grounding the top electrode for safety reasons and introducing complex electrode patterns to further tune the motion figure.

## 2.4 Experimental section

### 2.4.1 Materials

Interdigitated ITO electrodes were provided by Merck. The poly(dimethyl siloxane) (PDMS) elastomer and curing agent (Sylgard 184) were obtained from Dow Corning.

### 2.4.2 Sample preparation

The PDMS curing agent was added to the silicone elastomer in a concentration of 2 wt% to obtain a soft and flexible network. After thorough mixing of the two components, the trapped air in the sample was removed under reduced pressure. The substrates with the interdigitated ITO electrodes (10 x 10  $\mu\text{m}$ ) were cleaned by ultrasonication for 20 min in acetone and isopropanol, respectively, and dried with airflow. Subsequently, the clean substrates were subjected to a UV-ozone treatment for 20 min. The PDMS mixture was applied on the substrates by spin coating at 7000 rpm (acceleration rate 1000 rpm  $\text{s}^{-1}$ ) for 2 min, which resulted in a thickness of 8  $\mu\text{m}$ . The resulting layer of PDMS was cured overnight at 70  $^{\circ}\text{C}$ . After subjecting the PDMS surface to a 20 min UV-ozone treatment, a thin layer of gold (10 nm) was sputter-coated on top of the PDMS layer at a current of 65 mA for 11 s. The total electric activated area had a dimension of 1 cm x 1 cm.

### 2.4.3 Characterization

The alternating electric field with a square pulse function was provided by a function generator (Tektronix AFG3252). The electric signal from the function generator was then amplified with an amplifier (Falco Systems WMA-300). The in-plane potential difference was generated by a DC Power Supply (3B Scientific U33000). The output voltage and current were measured with an oscilloscope (Keysight InfiniiVision DSO-X 3032T). The surface topographies were measured with a Digital Holography Microscope (Lyncée Tec.). During the experimental period, no obvious fatigue was observed in the samples. The thickness of samples was measured by an interferometer (Fogale Nanotech Zoomsurf). The mechanical properties of PDMS were measured with an oscillatory frequency sweep by a rheometer (AR-G2, TA instruments) with a strain of 6%. AFM measurements were performed using a Multimode 8 AFM with a NanoScope V controller (Bruker) in the PeakForce Quantitative Nanomechanical Mapping mode.

## 2.5 References

- [1] G. Babakhanova, T. Turiv, Y. Guo, M. Hendriks, Q.-H. Wei, A. P. H. J. Schenning, D. J. Broer, O. D. Lavrentovich, *Nat. Commun.* **2018**, *456*, 1.
- [2] T. Takeshima, W. Y. Liao, Y. Nagashima, K. Beppu, M. Hara, S. Nagano, T. Seki, *Macromolecules* **2015**, *48*, 6378.
- [3] H. C. Cheng, S. Xu, Y. Liu, S. Levi, S. T. Wu, *Opt. Commun.* **2011**, *284*, 2118.
- [4] J. Sun, S. Xu, H. Ren, S. T. Wu, *Appl. Phys. Lett.* **2013**, *102*, 1.
- [5] O. T. Picot, R. Alcalá, C. Sánchez, M. Dai, N. F. Hughes-Brittain, D. J. Broer, T. Peijs, C. W. M. Bastiaansen, *Macromol. Mater. Eng.* **2013**, *298*, 33.
- [6] N. Bowden, W. T. S. Huck, K. E. Paul, G. M. Whitesides, N. Bowden, W. T. S. Huck, K. E. Paul, G. M. Whitesides, *Appl. Phys. Lett.* **1999**, *75*, 1.
- [7] T. Seki, *J. Mater. Chem. C* **2016**, *4*, 7895.
- [8] O. D. Lavrentovich, *Proc. Natl. Acad. Sci.* **2018**, *115*, 7171.
- [9] T. H. Ware, M. E. McConney, J. J. Wie, V. P. Tondiglia, T. J. White, *Science* **2015**, *347*, 982.
- [10] P. Dayal, O. Kuksenok, A. C. Balazs, *Proc. Natl. Acad. Sci.* **2013**, *110*, 431.
- [11] X. He, M. Aizenberg, O. Kuksenok, L. D. Zarzar, A. Shastri, A. C. Balazs, J. Aizenberg, *Nature* **2012**, *487*, 214.
- [12] M. L. Smith, C. Slone, K. Heitfeld, R. A. Vaia, *Adv. Funct. Mater.* **2013**, *23*, 2835.
- [13] T. Masuda, M. Hidaka, Y. Murase, A. M. Akimoto, K. Nagase, T. Okano, R. Yoshida, *Angew. Chemie - Int. Ed.* **2013**, *125*, 7616.
- [14] R. Yoshida, T. Takahashi, T. Yamaguchi, H. Ichijo, *J. Am. Chem. Soc.* **1996**, *118*, 5134.
- [15] R. Yoshida, *Biophysics (Oxf)* **2012**, *8*, 163.
- [16] S. Serak, N. Tabiryar, R. Vergara, T. J. White, R. A. Vaia, T. J. Bunning, *Soft Matter* **2010**, *6*, 779.
- [17] R. E. Pelrine, R. D. Kornbluh, J. P. Joseph, *Sensors Actuators, A Phys.* **1998**, *64*, 77.
- [18] L. J. Romasanta, M. A. Lopez-Manchado, R. Verdejo, *Prog. Polym. Sci.* **2015**, *51*, 188.
- [19] S. Shian, K. Bertoldi, D. R. Clarke, *Adv. Mater.* **2015**, *27*, 6814.
- [20] D. Pyo, S. Ryu, K. U. Kyung, S. Yun, D. S. Kwon, *Appl. Phys. Lett.* **2018**, *112*, 1.
- [21] E. M. Henke, K. E. Wilson, I. A. Anderson, *Bioinspiration and Biomimetics* **2018**, *13*, 1.
- [22] K. Cheng, A. Hussain, D. Clarke, *Proc. SPIE* **2018**, *1059423*, 1.
- [23] Q. Wang, X. Zhao, *Phys. Rev. E* **2013**, *88*, 1.
- [24] S. Shian, D. R. Clarke, *Soft Matter* **2016**, *12*, 3137.
- [25] A. Oláh, H. Hillborg, G. J. Vancso, *Appl. Surf. Sci.* **2005**, *239*, 410.
- [26] H. Hillborg, N. Tomczak, A. Oláh, H. Schönherr, G. J. Vancso, *Langmuir* **2004**, *20*, 785.
- [27] D. Liu, N. B. Tito, D. J. Broer, *Nat. Commun.* **2017**, *8*, 1.
- [28] W. Feng, D. J. Broer, D. Liu, *Adv. Mater.* **2018**, *1704970*, 1.
- [29] M. Hendriks, A. P. H. J. Schenning, D. J. Broer, *Soft Matter* **2017**, *13*, 4321.
- [30] D. Liu, L. Liu, P. R. Onck, D. J. Broer, *Proc. Natl. Acad. Sci.* **2015**, *112*, 3880.



## Chapter 2

# Chapter 3

## Finite element simulations on electric-field induced oscillating surfaces

---

This chapter is partially reproduced from: 'Oscillating surfaces fueled by a continuous AC electric field' F.L.L. Visschers, H. Gojzewski, G.J. Vancso, D.J. Broer, D. Liu, *Adv. Mater. Interfaces*, 2019, 1901292.

### 3.1 Introduction

In the previous chapter we introduced an approach to generate an oscillating wave in soft polymer coatings consisting of loosely crosslinked poly(dimethylsiloxane) (PDMS) under an AC electric field. The applied field was continuous, meaning that there was no on and off switching needed to generate the required effect. The surface motilities that were demonstrated have the potential to lead to a plurality of applications, such as self-cleaning,<sup>[1]</sup> adjustable tribology,<sup>[2]</sup> de-icing,<sup>[3]</sup> haptics<sup>[4]</sup> and even motile transport of species at the coating surface.<sup>[5]</sup> However, for many of the practical applications the coating needs to be optimized further, for example by introducing complex electrode patterns to further tune the motion figure. In order to make well-informed and targeted adjustments to the system, we need to fully understand the processes that take place within our coatings when they are subjected to an electric field. More specifically, the material displacement inside our coating under the condition of volume preservation, as well as the distribution of the electric field must be elucidated. A better understanding of these subjects can be obtained by performing simulations on our system using the finite element method (FEM). Such simulations also enable us to predict the outcome of experiments that are otherwise impossible to perform due to practical limitations like the dielectric breakdown strength of our material. Finally, a reliable FEM model can guide us to perform targeted experiments and help with the interpretation of their results.

In order to model the movement of our coating resulting from the applied electric fields, we need to perform dynamic 3D simulations in which the viscoelastic properties of our material are accurately represented. The simulation of viscoelastic properties is more complex than the simulation of purely elastic properties due to their strain-rate dependence, loading history dependence and energy dissipative behavior as a result of internal damping.<sup>[6]</sup> Dependent on the temperature and loading conditions, viscoelastic materials behave like a combination of elastic solids and viscose liquids. Constitutive viscoelastic

parameters of a given material can be obtained from the frequency-dependent storage modulus ( $G'$ ) and loss modulus ( $G''$ ). These parameters are represented by the Prony series in the following equations:

$$G'(\omega) = G_{\infty} + \sum_i \frac{G_i \omega^2 \tau_i^2}{1 + \omega^2 \tau_i^2} \quad (4)$$

$$G''(\omega) = \sum_i \frac{G_i \omega \tau_i}{1 + \omega^2 \tau_i^2} \quad (5)$$

In equation (4) and (5)  $G_{\infty}$  is the long term (shear) modulus,  $\omega$  is the circular frequency,  $G_i$  and  $\tau_i$  are the intensity coefficients and relaxation time constants of the Prony series that will represent the viscoelastic parameters of the material within our FEM simulations. Various methods exist to calculate the Prony series from dynamic mechanical analysis.<sup>[7–10]</sup> One of those methods is using the program 'ViscoData' which can fit data from the frequency sweep experiments to a maximum of 40 relaxation modes.<sup>[11]</sup> The Prony series obtained from this program can directly be inserted in FEM software like Marc Mentat.<sup>[12]</sup>

### 3.2 Results and discussion

In order to provide an in-depth explanation and deep understanding of the mechanisms that drive the surface deformations, we first need to know how the electric field is distributed through the thickness of our coating. For this study, we have performed finite element simulations of a 2D cross-section of our system, using COMSOL Multiphysics (AC/DC module).<sup>[13]</sup> In the simulations, we assumed the length of the electrodes is infinite and the electrode thickness was set at 10 nm for E0 and 100 nm for E1/E2 (Figure 3.1). The media above the electrodes is the PDMS polymer with a relative permittivity of 2.7 as indicated by the Technical Data Sheet supplied by the manufacturer. First, the electric field distribution is modeled in a di-electrode circuit (Chapter 2, Figure 2.1a) where only one patterned electrode E1 is present. When applying a control voltage of 150 V, the simulated result suggests that the electric field strength varies between 15 and

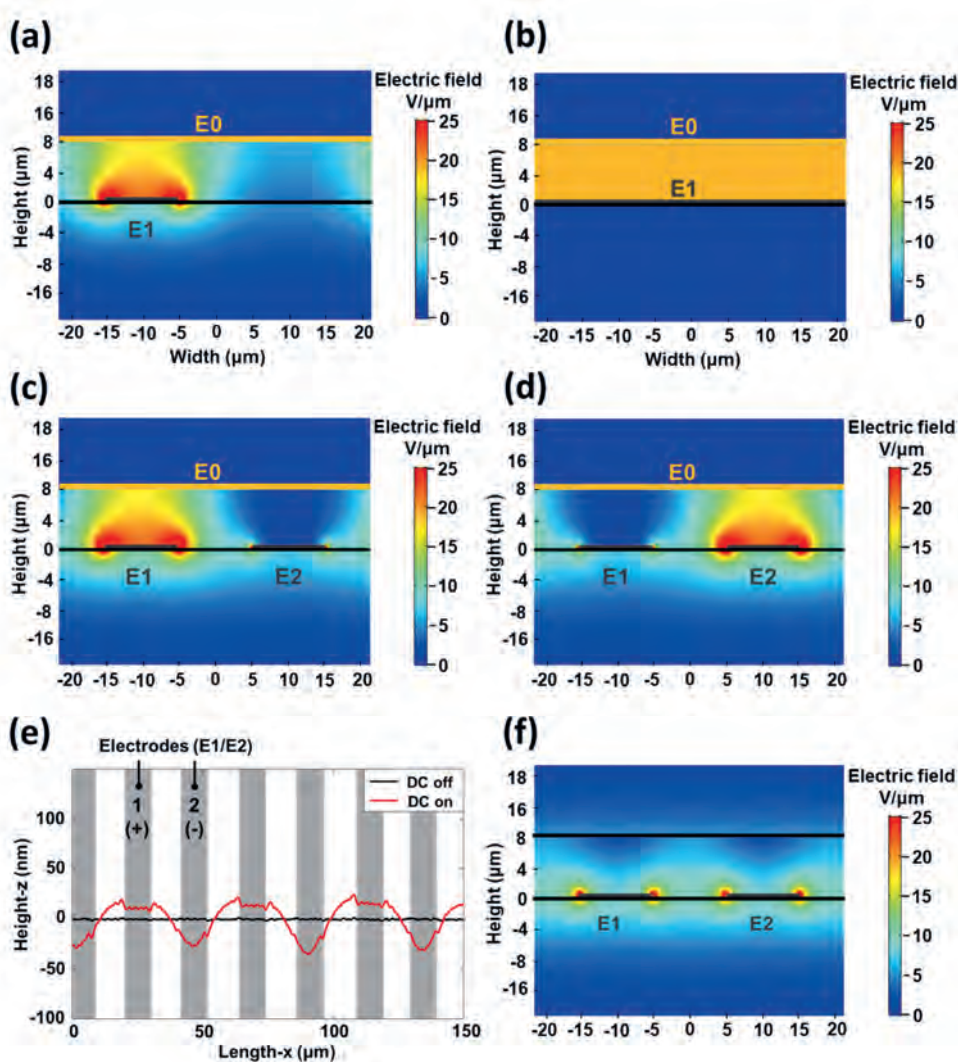


**Figure 3.1** | Simulated electric field distributions in cross-sections of our dielectric coating. (a) The field distribution in a di-electrode setup while applying 150V.  $E_0$  and  $E_1$  have opposite polarity. (b) A homogeneous field distribution is predicted in a di-electrode setup where both electrodes  $E_0$  and  $E_1$  are continuous. The field strength has a value of  $19 \text{ V}/\mu\text{m}$ . (c) Snapshot of the field distribution in a tri-electrode setup.  $E_0$  and  $E_1$  have opposite polarity, while  $E_0$  and  $E_2$  have equal polarity. (d) A second snapshot of the field distribution in a tri-electrode setup. Now  $E_0$  and  $E_1$  have equal polarity, while  $E_0$  and  $E_2$  have opposite polarity. (e) The 2D profile of the surface relief created by an in-plane DC potential, measured by DHM. (f) The field distribution across the polymer film when only an in-plane DC potential is applied.

$25 \text{ V}/\mu\text{m}$  in the activated area (Figure 3.1a). In the non-activated area there is still some electric field present, averaging at a value of  $5 \text{ V}/\mu\text{m}$ . The unusual shape of

the electric field distribution with high field strengths at the edges of E1 is caused by the difference in width between the top and bottom electrodes. A homogeneous electric field distribution with the expected field strength of  $19 \text{ V}/\mu\text{m}$  is obtained in the model when E1 covers the entire glass substrate (Figure 3.1b). Next, the electric field distribution is modeled in a tri-electrode circuit (Chapter 2, Figure 2.2a) where both patterned electrodes E1 and E2 are present. In this case, due to the use of an alternating power source, two different electric field distributions occur, depending on the polarity of the top electrode E0. The first field distribution is calculated when the electrodes E1 and E0 have opposite charges, while E2 and E1 have an equal charge (Figure 3.1c). A potential is thus built between E1 and E0 and the electric field is restricted to the area above electrode E1. Interestingly, in this case the area above E2 is effectively shielded off from the electric field simply because E2 and E0 have the same polarity. By flipping the polarity of E0, the electric field distribution switches positions and is now located above electrode E2 while the area above electrode E1 is shielded from the electric field.

In chapter 2, we also performed experiments where only an in-plane DC electric field was applied to E1 and E2, in order to find the origin of the deformation asymmetry in the tri-electrode configuration. As a result, small protrusions were observed and attributed to an ionic impurity from the platinum catalyst in the curing agent of the PDMS, in which the negatively charged material accumulates at the positive electrode. The shape of the relief, however, was not as smooth as found for the tri-electrode system (Figure 3.1e). Now, we can explain this odd shape by calculating the electric field distribution within this experimental setup (Figure 3.1f). The simulations indicate that the electric field is strongest at the edges of the electrodes E1 and E2, which causes the small elevations ('ears') appearing at the sides of each hill. Furthermore, the electric field above the electrodes is smaller than the electric field above the gap areas. As a consequence, any dipoles within the polymer will migrate towards the gap areas, resulting in a slight reduction of the surface height above the electrodes.

After determining how the electric field is distributed within our coating, the next step is to gain more insight into the surface dynamics resulting from the electric fields and to validate our experimental results. To do so, we perform FEM simulations using Marc Mentat with a coupled electrostatic-structural analysis. In the simulations, we assume the length of the electrodes is infinite and the electrode thickness is set at 10 nm for E0 and 100 nm for E1 and E2. Both the glass and the patterned electrodes E1 and E2 are rigid (infinite stiffness) and static. The flexible (finite stiffness) and dynamic media above the electrodes is defined as a Neo-Hookean type material, as justified by the low effective strain, with the viscoelastic properties as obtained from rheology oscillatory frequency sweeps (Chapter 2, Figure 2.4f). The program 'ViscoData' is used to convert the frequency-dependent storage modulus of the material to a 5-term Prony series, which is directly inserted into Marc Mentat to define viscoelastic properties. The obtained  $G_0$  and  $G_\infty$  have values of 18300 Pa and 433 Pa respectively, and the Prony series itself is given in table 3.1.

**Table 3.1** | *Prony series obtained after converting the experimental storage and loss modulus with the program 'ViscoData'.*

<b>Relaxation time (ms)</b>	<b>Coefficients</b>
<b>2.3</b>	<b>0.8</b>
<b>22</b>	<b>0.11</b>
<b>120</b>	<b>0.04</b>
<b>670</b>	<b>0.019</b>
<b>4200</b>	<b>0.01</b>

The oxidation layer resulting from the UV/ozone treatment is modeled as an 11 nm thick elastic-plastic isotropic material with Young's modulus of 4.93 MPa as determined from AFM measurements. The top electrode is modeled with the material properties of gold. The elements of all materials are assigned to contact

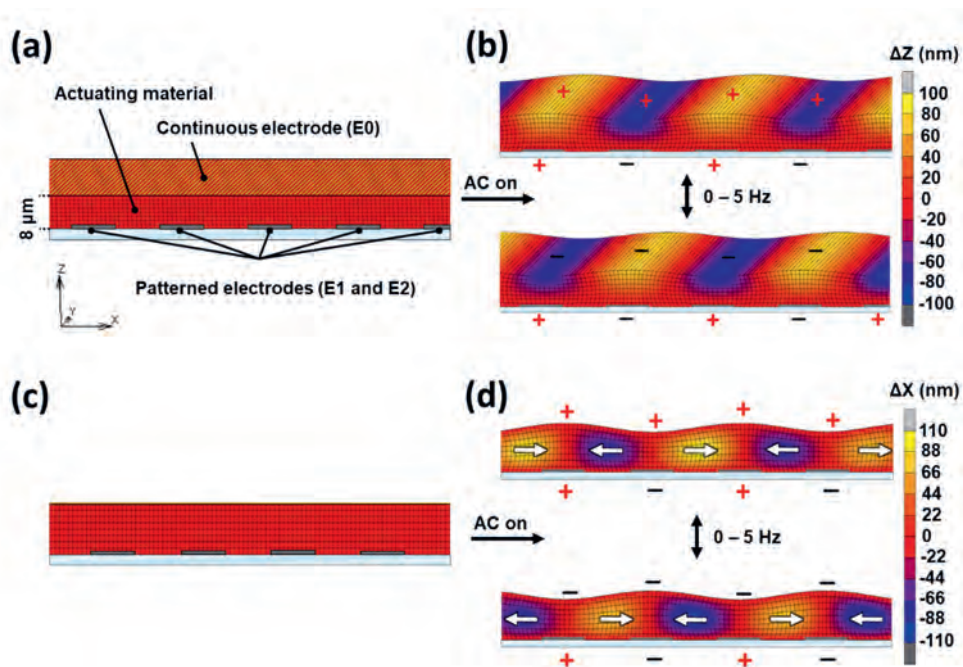


**Figure 3.2** | Results from finite element simulations showing the cross-section and top layer of our coating. (a) The initial shape of the coating before the electric field is applied. (b) The actuated shapes of the coating while the alternating electric field is applied. The color indicates the relative movement of each node in the Z-direction. (c) Again, the initial shape of the coating is shown, however, now the movement in the X-direction is traced. (d) As the electric field is applied, the movement of material within the coating is visualized by tracing in-plane trajectory of each node.

bodies and the corresponding contact interactions are defined as 'glued' and 'permanent'. All static elements are assigned to element type 7 (Hexagonal, Full integration) and all dynamic elements are assigned to element type 84 (Hexagonal, Full & Hermann Formulation).<sup>[14]</sup> A potential of 150 V is applied via the tri-electrode driving scheme where E1 and E2 have opposite polarity, while E0 switches its polarity as a function of time. During the simulations, the displacement of each node within the coating is traced and analyzed. Analysis of the displacement in the Z-direction, perpendicular to the plane of the coating, yields results that closely resemble the experimental data from DHM measurements (Figures 3.2a and 3.2b). Without the electrical stimulus, each node remains stationary as indicated by the red color. As soon as the electric potentials are introduced the coating morphs into a wave oscillating between two opposite



states. As expected, the valleys are located in the areas where the polarity between top and bottom electrodes is opposite, while the hills are situated in locations where top and bottom electrodes have an equal charge. The amplitude of the deformation (150 nm) matches with the values found experimentally, which validates the reliability of our model. Furthermore, the presence or absence of the 11 nm thick elastic-plastic type oxidation layer, does not have a significant effect on the amplitude of the deformation. For the sake of completeness, we have still included this layer in all future simulations. Next, we use the same simulation to predict the movement of the material inside our dielectric coating during the surface oscillations. Instead of the Z-direction, we now trace the movement of each node in the X-direction. The results indicate that movement of material parallel to the substrate occurs throughout almost the entire cross-section and is largest in the middle of the coating. It explains why the presence of the relatively thin oxidation layer on top seems to have a negligible effect on the amplitude of the deformation. Additionally, the lateral displacement concentrates above the gap areas in-between electrodes E1 and E2, whereas the movement in the Z-direction occurs mostly above the patterned electrodes. As expected, the dielectric material moves away from the areas where a potential is applied between top and bottom electrodes and accumulates where the charges between top and bottom are equal.

For further verification of our model the amplitude values of the surface wave are calculated as a function of the applied electric field strength and compared with the experimental results (Figure 3.3a). In this case the electric field values are adjusted by varying the applied potentials on the electrodes. In the simulations, perfect conditions are assumed and a similar although slightly improved performance is determined. Next, the effectiveness of the Prony series in the Neo-Hookean type material is tested by analyzing the oscillating behavior of the standing wave. We selected two adjacent areas above the electrodes and traced their relative height changes under the input of a continuous electric field (Figure 3.3b). Similar to the experimental results, the deformation in the simulation

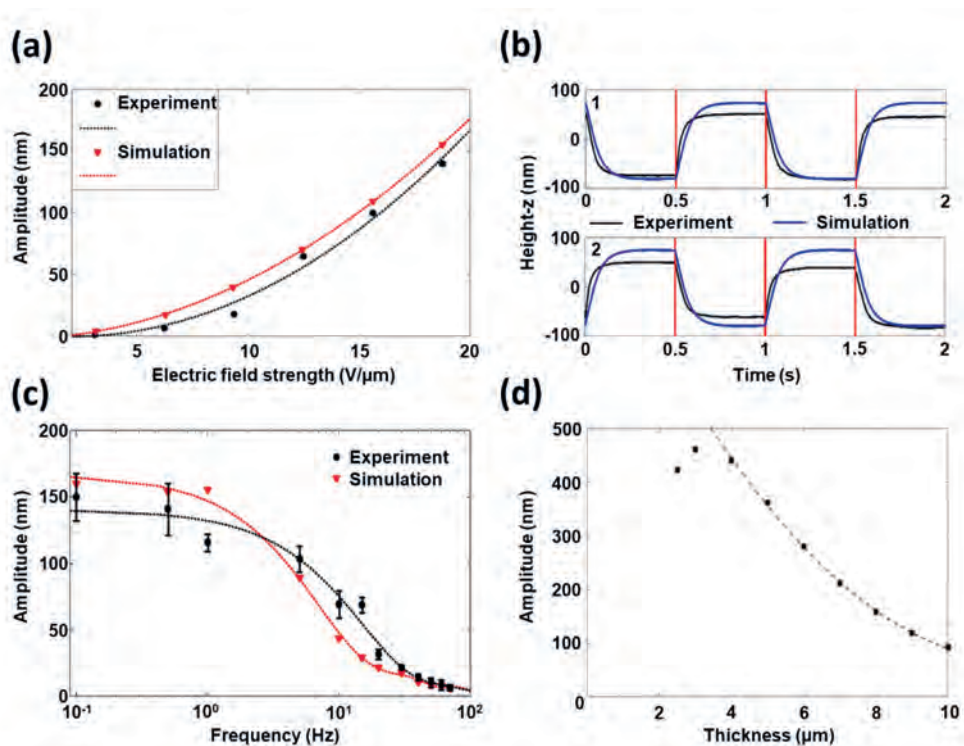


**Figure 3.3** | Details of influential parameters on the oscillation of wave. (a) Influence of the electric field strength on the simulated (red) and experimental (black) deformation amplitude. (b) Simulated (blue) and real (black) dynamics of the height change at a frequency of 1 Hz. (c) Influence of the frequency on the deformation amplitude. (d) Simulated influence of the thickness of the coating on the deformation amplitude. Below a thickness of 4  $\mu m$ , the restriction from the rigid substrate dominates as these results cannot be fitted to a quadratic equation.

initiates with a rapid elastic-like response, followed by a gradual change as controlled by the Prony series. As a final validation, we monitored the deformation amplitude during a simulated frequency sweep. Both simulations and experimental results indicate that at a frequency above 5 Hz, the deformation amplitude decreases rapidly, which is related to the frequency-dependent storage ( $G'$ ) and loss ( $G''$ ) moduli as discussed in Chapter 2. We attribute the small differences between the simulated and experimental oscillating behavior to the somewhat different conditions used within the rheometer experiments, of which the results are used to obtain the Prony series. The differences include the curing condition of the PDMS, which occurs in a 1000  $\mu m$  layer while in contact with the top cone plane, and the application of a rotary force rather than a compressive

force during the frequency sweeps. As the differences between experiment and simulation are small, the model can be used to predict the outcome of experiments that are difficult or impossible to perform due to practical limitations like the dielectric breakdown strength of the material. For example, it is possible to predict the influence of the coating thickness on the amplitude of the deformation (Figure 3.3d). The outcome of the model shows that above a thickness of 4  $\mu\text{m}$ , the amplitude decreases quadratically as the thickness increases. Below a thickness of 4  $\mu\text{m}$ , the deformation amplitude becomes restricted by the presence of the rigid substrate. Unfortunately, at a thickness of 2  $\mu\text{m}$  and below, the simulated stresses in the system are too large and the software is unable to compile the simulation. We expect that the amplitude will decrease to zero when the thickness of the coating is reduced further.

### 3.3 Conclusions

In conclusion, we model the electric field distribution within our coating using the finite element method. The simulated results indicate a shielding effect above one of the bottom ITO electrodes in a tri-electrode configuration. The electric field distributions resulting from in-plane DC-potentials help us understand the shape of the corresponding surface relief. Furthermore, in the dynamic 3D FEM model, the viscoelastic properties can be expressed using a Prony series. With this model we systematically reproduce the experimental results and elucidate how the material moves within our coating. After comparing the simulated results with experiments, taking parameters like electric field strength, response time and frequency into consideration, we conclude that the model accurately represents our device. Finally, the model is used to simulate the results of experiments that we are unable to perform due to practical limitations, which predicts that the restriction from the rigid substrate starts to dominate at thicknesses below 4  $\mu\text{m}$ . The simulations described in this chapter can guide our future experiments and help with the interpretation of their results.

## **3.4 Experimental section**

### **3.4.1 Finite Element Method Simulations**

The electric field distribution in a 2D cross-section of the coating was simulated using COMSOL Multiphysics 5.2. The electric field-induced surface dynamics of the coating were simulated in 3D using Marc Mentat 2014.0.0.

### **3.4.2 Materials**

Interdigitated ITO electrodes were provided by Merck Darmstadt. The poly(dimethyl-siloxane) (PDMS) elastomer and curing agent (Sylgard 184) were obtained from Dow Corning.

### **3.4.3 Sample preparation**

The PDMS curing agent was added to the silicone elastomer in a concentration of 2 wt% to obtain a soft and flexible network. After thorough mixing of the two components, we removed the trapped air in the sample under reduced pressure. The substrates with the interdigitated ITO electrodes (electrode widths/gaps = 10/10  $\mu\text{m}$ ) were cleaned by ultrasonication for 20 min in acetone and isopropanol, respectively, and dried with airflow. Subsequently, the clean substrates were subjected to a UV-ozone treatment for 20 min. The PDMS mixture was applied on the substrates by spin coating at 7000 rpm (acceleration rate 1000 rpm  $\text{s}^{-1}$ ) for 2 min, which resulted in a thickness of 8  $\mu\text{m}$ . The resulting layer of PDMS was cured overnight at 70 °C. After subjecting the PDMS surface to a 20 min UV-ozone treatment, a thin layer of gold (10 nm) was sputter-coated on top of the PDMS layer at a current of 65 mA for 11 s. The total electric activated area had a dimension of 1 cm x 1 cm.

### 3.4.4 Characterization

The alternating electric field with a square pulse function was provided by a function generator (Tektronix AFG3252). The electric signal from the function generator was then amplified with an amplifier (Falco Systems WMA-300). The in-plane potential difference was generated by a DC Power Supply (3B Scientific U33000). The output voltage and current were measured with an oscilloscope (Keysight InfiniiVision DSO-X 3032T). The surface topographies were measured with a Digital Holography Microscope (Lyncée Tec.). The thickness of samples was measured by an interferometer (Fogale Nanotech Zoomsurf). The mechanical properties of PDMS were measured with an oscillatory frequency sweep by a rheometer (AR-G2, TA instruments) with a strain of 6%.

### 3.5 References

- [1] W. Feng, D. J. Broer, D. Liu, *Adv. Mater.* **2018**, 1704970, 1.
- [2] D. Liu, D. J. Broer, *Angew. Chemie Int. Ed.* **2014**, 53, 4542.
- [3] F. Wang, F. Lv, Y. Liu, C. Li, Y. Lv, *J. Adhes. Sci. Technol.* **2013**, 27, 58.
- [4] W. H. Park, T. H. Yang, Y. Yoo, S. Choi, S. Y. Kim, *IEEE World Haptics Conf. WHC 2015* **2015**, 165.
- [5] G. Babakhanova, H. Yu, I. Chaganava, Q. H. Wei, P. Shiller, O. D. Lavrentovich, *ACS Appl. Mater. Interfaces* **2019**, 11, 15007.
- [6] M. F. P. Costa, C. Ribeiro, *AIP Conf. Proc.* **2011**, 1389, 771.
- [7] M. A. Tapia Romero, M. Dehonor Gomez, L. E. Lugo Uribe, *Ing. Investig. y Tecnol.* **2020**, 21, 1.
- [8] M. Baumgaertel, H. H. Winter, *Rheol. Acta* **1989**, 28, 511.
- [9] J. E. L. Pacheco, C. A. Bavastri, J. T. Pereira, *Lat. Am. J. Solids Struct.* **2015**, 12, 420.
- [10] M. Mehnert, M. Hossain, P. Steinmann, *Int. J. Non. Linear. Mech.* **2018**, 106, 13.
- [11] M. Herdy, *ViscoData* **2007**, 1.
- [12] MSC Software, *MSC. Softw. Corp.* **2014**, Volume A, 360.
- [13] X. Wang, X. Wang, T. Lin, *J. Mater. Res.* **2012**, 27, 3013.
- [14] MSC Software, *MSC. Softw. Corp.* **2014**, Volume B, 130.

# Chapter 4

## Improved electrode design for programmed surface oscillations

---

This chapter is partially reproduced from: 'Electric-field induced oscillating surface waves with programmable shapes' F.L.L. Visschers, D.J. Broer, D. Liu, *Proceedings of SPIE 11375, Electroactive Polymer Actuators and Devices XXII*, 2020, 113751F.

## 4.1 Introduction

In natural surfaces, many different micro- and nanostructures exist, each optimized for their specific function.<sup>[1]</sup> A surface covered with individual tooth-like scales is present on the surface of a Galapagos shark (*Carcharhinus galapagensis*), which reduces drag when moving through the water due to their longitudinal grooves.<sup>[2]</sup> A complex hierarchical structure of lamellae, setae, branches and spatula covers the surface of gecko's feet, designed for controlled adhesion when climbing vertical surfaces.<sup>[3-6]</sup> Hexagonally packed nanoscopic pillars shroud the surface of moth's eyes, resulting in very low reflectance of visible light from any direction.<sup>[7,8]</sup> A hierarchical structure of oriented hairs (microsetae) with fine nanogrooves and covered with cuticle wax makes the leg surfaces of pond skaters (*Gerris remiges*) superhydrophobic and water-resistant, which enables them to walk on water.<sup>[9]</sup> In plants, microscopic hairs on surfaces fulfill a variety of functions depending on their density, orientation, size and shapes.<sup>[10,11]</sup> The different functions include the reduction of movement of insects on the plant surface, reduction of mechanical abrasion by sand particles and increasing or decreasing the wettability and loss of water. From all these examples we can conclude that surfaces with different functions require various shapes of the microstructures. As such, the shape of the oscillating surface wave in our electric field responsive coatings should also be programmable to open options to more applications.

In chapter 2 we presented the design of a dielectric elastomer coating with an initially flat surface that deforms and oscillates between two active states upon application of a continuous AC electric field.<sup>[12]</sup> The device configuration consists of two patterned bottom indium tin oxide (ITO) electrodes and one continuous gold top electrode which sandwich an 8  $\mu\text{m}$  thick poly(dimethyl siloxane) (PDMS) coating that has been reinforced by a thin layer of silicon oxide (Figure 4.1a). The surface deformation is achieved by applying a potential difference over one of the bottom ITO electrodes and the continuous top electrode. The generated

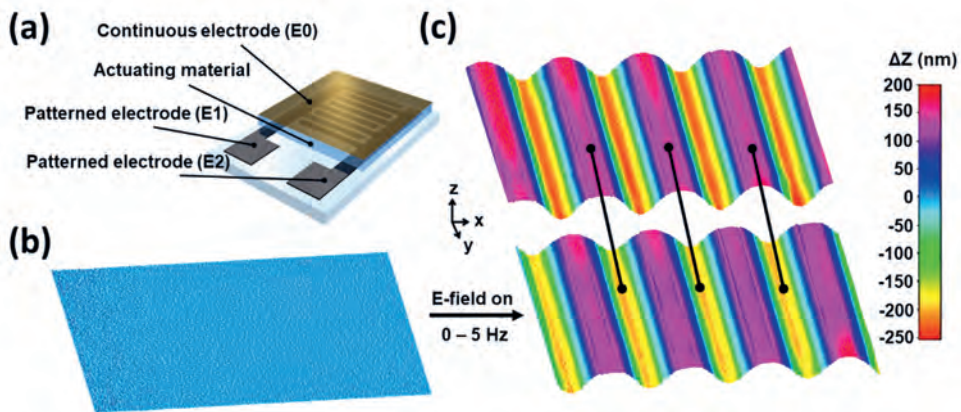


**Figure 4.1** | Device design and the oscillating surface waves in an elastomer fueled by an electric field. (a) Schematic representation of the device configuration. 3D images of the sample surface measured by DHM reveal (b) the initial flat surface without electric field and (c) the two active states between which the surface oscillates following the frequency of the applied electric field.

electric field induces localized Maxwell stresses that compress the coating and push excess volume towards the in-active areas, resulting in a surface wave. The wave is brought into oscillation by continuously inverting the polarity over either the patterned bottom electrodes or the continuous top electrode with an AC power source. The surface dynamics are verified experimentally by digital holographic microscopy (DHM) measurements (Figures 4.1b and 4.1c). In this chapter, we explore the use of new electrode designs and corresponding addressing schemes. First, we use DHM measurements to determine how the oscillating surface wave is affected by different electric circuits. Second, we use simulation with the finite element method (FEM) to change and optimize the shape of the surface wave with different electrode patterns. The simulated results are confirmed experimentally by DHM measurements, revealing four different types of oscillating surface waves that can be created.



## 4.2 Results and discussion

In the original circuit design described in Chapter 2 and modeled in Chapter 3 a continuous in-plane DC potential of 150 V is applied between E1 and E2 (Figure 4.2a). As previously described, this in-plane potential causes a surface relief in which the material above the positive electrode (1) forms a peak, while the material forms a valley at the location above the negative electrode (2). A consequence of this effect is a deformation asymmetry in the oscillating surface wave, where the protrusions above the positively charged electrode are larger than the protrusions above the negatively charged electrode (Figure 4.2b). In our

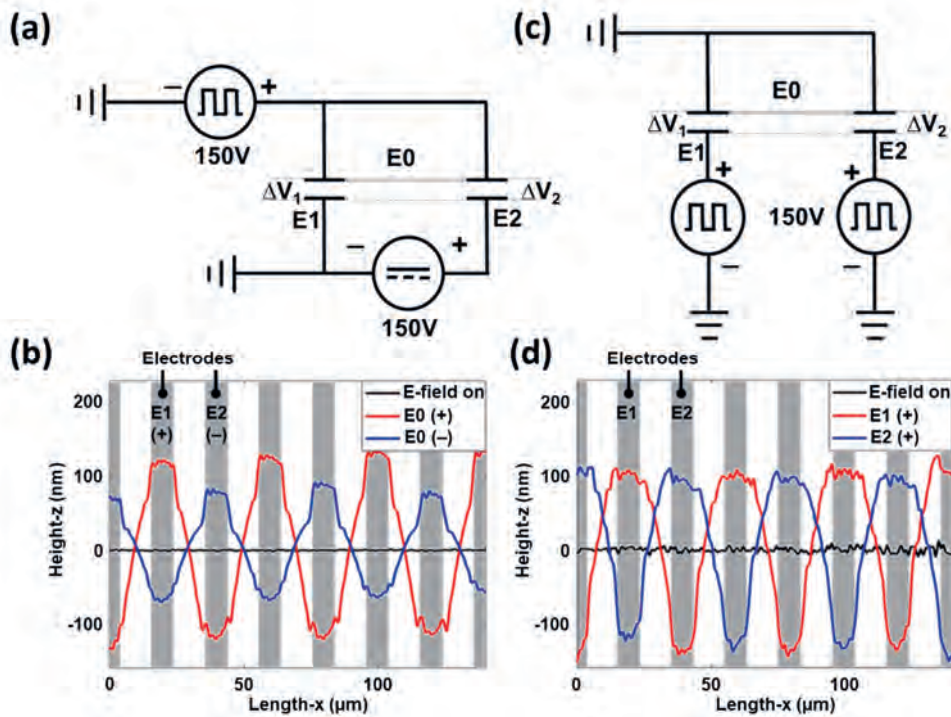


**Figure 4.2** | Details of the electric circuits of the tri-electrode driving schemes. (a) The previously used electric circuit with a continuous in-plane DC potential provided by the electrodes E1 and E2. (b) A 2D profile of the oscillating surface wave using the circuit scheme from Figure 4.2a. The two active states (red and blue) show different amplitudes of the wave. (c) The new design of the electric circuit in which the in-plane potential switches between +150 V and -150 V. (d) A 2D profile of the oscillating surface wave using the circuit scheme from Figure 4.2c. Both active states (red and blue) show a similar amplitude and shape of the wave.

new circuit design that we present here (Figure 4.2c), we prevent this effect by switching the polarity of the two bottom electrodes E1 and E2 instead of the top electrode E0. Now the in-plane potential switches between +150 V and -150 V. Consequently, the resulting ion-related deformation has a limited time to develop and the effect on the surface wave are measured to be equal in both states (Figure 4.2d). The new circuit design also provides an enhanced safety for potential users, because now the top surface of the device is grounded. In addition, because of its neutral charge it no longer attracts particles that are charged with static electricity. In all further experiments we use the circuit design from Figure 4.2c.

To analyze the application potential of new designs for the electrode patterns, we schematically reproduced the setup of our device in Marc Mentat using the coupled electrostatic-structural analysis model described in Chapter 3. Except for adjustments in the electrode pattern, we also applied the potential following the electric circuit design from Figure 4.2c. In Chapter 2 and 3, we used electrode patterns with both the gap distances and the electrode widths of 10  $\mu\text{m}$ . To estimate the influence of variations on these patterns, also in combination with the improved electrical addressing scheme, we simulated the response from a sample with varying gap distances between the electrodes. At a constant

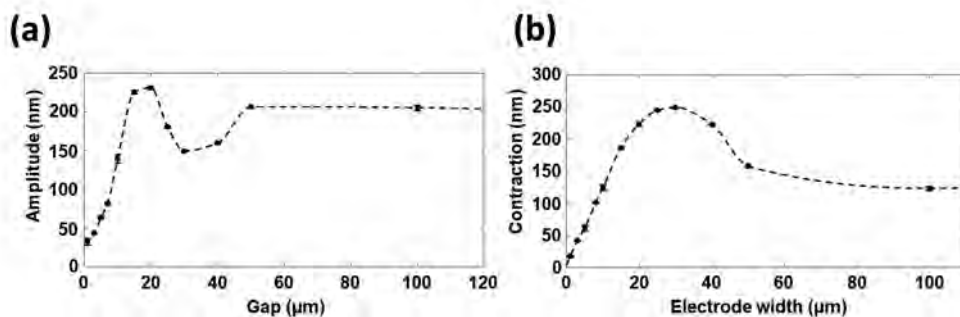


**Figure 4.3 |** Simulated effect of changing the geometry of E1 and E2. (a) At a constant electrode width of 10  $\mu\text{m}$  the amplitude of the oscillating wave changes as the width of the gap between E1 and E2 increases. An optimal gap distance of 20  $\mu\text{m}$  is found. (b) At a constant gap distance of 100  $\mu\text{m}$  the contraction depth above the electrodes changes as the width of the electrodes increases. An optimal electrode width of 30  $\mu\text{m}$  is determined.

electrode width of  $10\ \mu\text{m}$  the gap distance is varied between  $1$  and  $100\ \mu\text{m}$  and we calculated the amplitude of a wave oscillating at a frequency of  $1\ \text{Hz}$  (Figure 4.3a). Initially, the amplitude increases with increasing gap distance, because the compressed excess of volume can escape to larger neighboring areas. At gap distances above  $20\ \mu\text{m}$ , this trend is no longer continued. Now, the amplitude of the wave depends on how close the pattern of the electrodes matches the inherent shape of the surface wave. To understand this better, the shape of the wave at large gap distances of  $100\ \mu\text{m}$  is considered (Figure 4.4a). Here, the deformed area above E1 no longer overlaps with the deformation that occurs above E2, which leads to a situation where the two electrodes are mechanically 'decoupled'. From this unrestricted shape of the wave, the naturally occurring distance between the valley above the electrode and the peak above the gap is determined to be  $30\ \mu\text{m}$ . As the gap distance is decreased to  $50\ \mu\text{m}$ , the peaks created by contraction above E1 overlap with the peaks induced by contraction

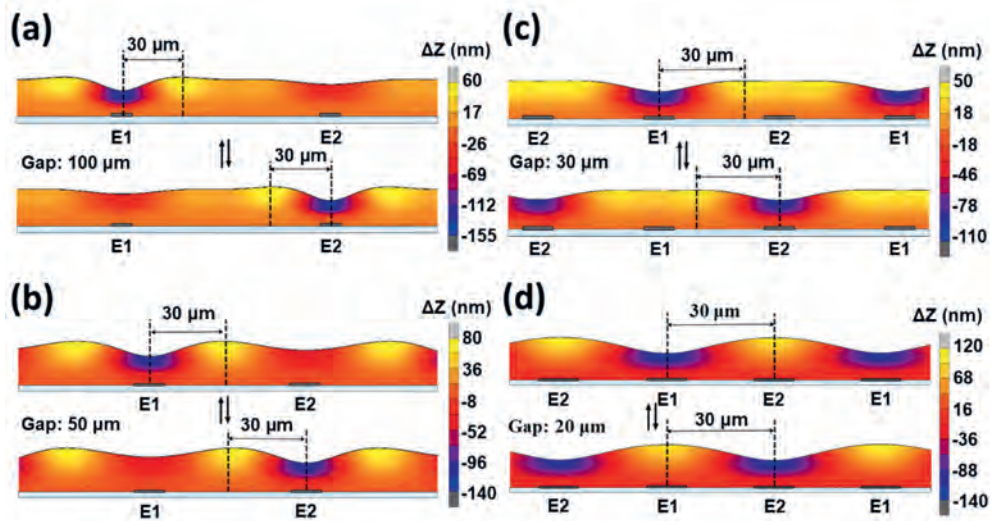


**Figure 4.4** | The calculated shapes of the surface wave at various gap distances. (a) A gap distance of  $100\ \mu\text{m}$ . E1 and E2 do not affect each other at this gap distance. (b) A gap distance of  $50\ \mu\text{m}$ . The peaks from E1 and E2 overlap, giving rise to static peaks and oscillating valley depths. (c) A gap distance of  $30\ \mu\text{m}$ . The peaks from E1 now overlap with the valleys of E2, while the distance is still too large for the peaks from two neighboring E1 (or E2) electrodes to overlap. (d) A gap distance of  $20\ \mu\text{m}$ . This gap distance enables the largest amplitude, because the peaks from two neighboring E1 (or E2) electrodes exactly overlap.

above E2 (Figure 4.4b). In this design, when the electric field is applied, static peaks are produced while the valleys directly above E1 and E2 oscillate in depth. By reducing the gap distance even further to 30  $\mu\text{m}$ , the peaks generated by E1 are pushed into the valleys occurring above E2, which diminishes the amplitude of the wave (Figure 4.4c). Finally, at a gap distance of 20  $\mu\text{m}$ , the peaks from two consecutive E1 (or E2) electrodes overlap exactly, which results in an optimal amplitude of the wave (Figure 4.4d).

Next, the influence of the width of the electrodes is investigated at a constant gap distance of 100  $\mu\text{m}$  (Figure 4.2b). This specific gap distance is selected to ensure E1 and E2 are completely mechanically decoupled. In this case, only the depth of the valley must be taken into consideration rather than the amplitude of the wave. Initially, the depth of the valley increases as the size of the electrodes increases, which is caused by the increased capacitance of the electrode. At a width of 30  $\mu\text{m}$ , the electrode covers exactly the area within the wave that is contracting when the inherent shape of the wave is preserved (Figure 5a). Increasing the electrode width even further causes a decrease in contraction, because the area that was previously expanding is now also forced into contraction. At broad electrode widths of over 100  $\mu\text{m}$ , this effect increases to the point where two separate valleys arise (Figure 4.5b). The valleys can only occur at the edge of the electrode, close to an expanding area where the compressed excess of volume can escape (Figure 4.5c). Furthermore, the finite element calculations indicate that within this geometry the in-plane motion of material ( $\Delta X$ ) is much larger than the out-of-plane motion ( $\Delta Z$ ).

Conclusively, it is possible to predict the optimum geometry for a symmetrical oscillating wave with a large amplitude. As indicated by the results from gap variations, for the selected set of materials parameters the optimum distance between the center of E1 and E2 should be 30  $\mu\text{m}$ . The results from electrode width variations indicate that the optimal width of E1 and E2 is also 30  $\mu\text{m}$ . Combining these two features, however, results in a gap distance of 0  $\mu\text{m}$  which

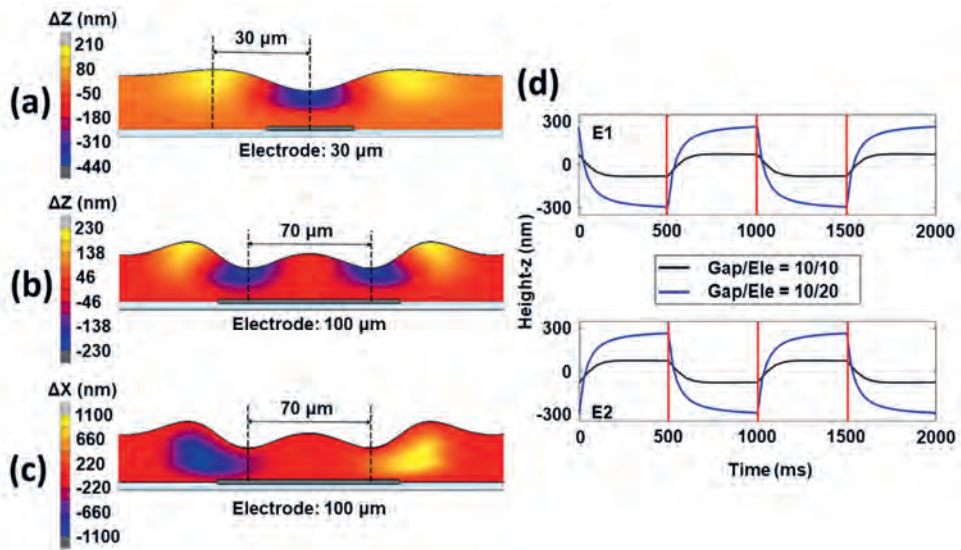


**Figure 4.5** | The calculated shapes of the surface wave at various electrode widths and the dynamics of a surface wave with optimized geometry. (a) An electrode width of 30  $\mu\text{m}$  performs best as the electrode exactly covers the contracting area of an unrestricted surface wave. (b) Contraction over an electrode width of 100  $\mu\text{m}$  leads to the formation of two separate valleys above one electrode. (c) The in-plane motion of material during contraction over an electrode with a width of 100  $\mu\text{m}$ . The compressed excess of material can only escape at the edges of the electrode. (d) The dynamics of the height change above E1 and E2 at a frequency of 1 Hz for the original (black) and optimized (blue) geometries. The vertical red lines indicate when the polarity of E1 and E2 switches.

would cause a short circuit. Therefore, a realistic alternative is a geometry with electrode widths of 20  $\mu\text{m}$  and gap distances of 10  $\mu\text{m}$ . The oscillating behavior of the standing wave in this geometry is now compared to the oscillating behavior of the original, which has electrode widths and gap distances of 10  $\mu\text{m}$  (Figure 4.5d). As expected, the simulations predict a large increase in the amplitude of the wave from 150 nm to 550 nm when using the optimized geometry, while the time-dependent behavior of the oscillations remains similar.

The FEM simulations discussed in the previous section demonstrate how the inherent shape of the surface wave can be used to not only optimize the amplitude of the oscillations but also how different shapes of the wave can be preprogrammed. Now, the predictions from our simulations are verified experimentally, to determine if it is indeed possible to enhance and preprogram the shape of the oscillating surface wave. At a frequency of 1 Hz, various electrode

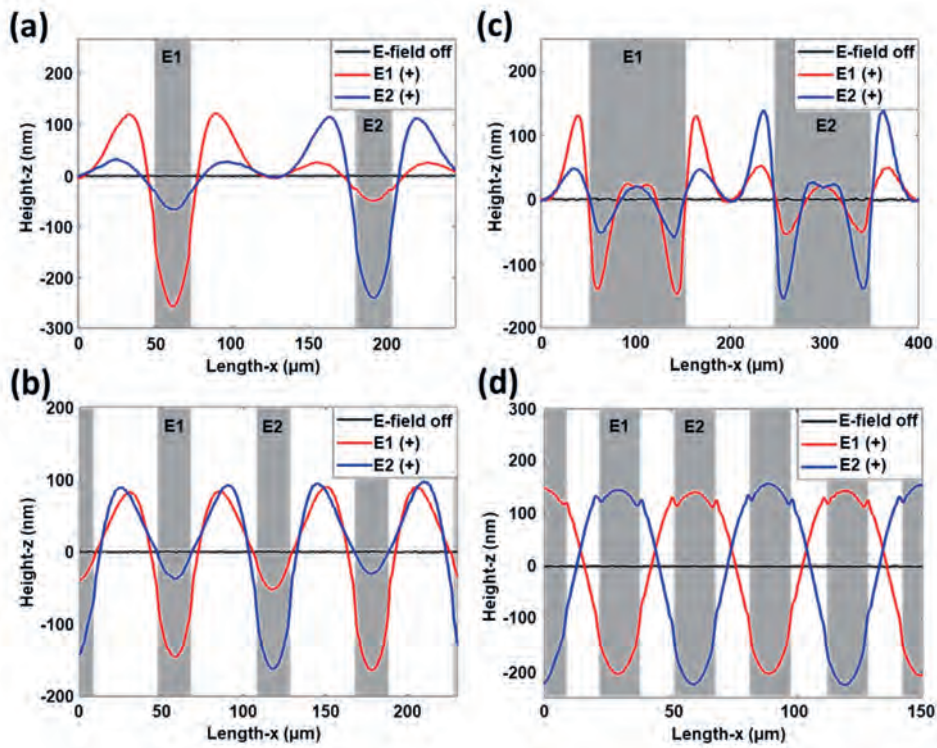


**Figure 4.6 |** The 2D profiles of oscillating surface waves generated by the tri-electrode driving scheme using various electrode geometries, measured by DHM at a frequency of 1 Hz. (a) Surface waves obtained by using an electrode geometry where width/gap = 22/105  $\mu\text{m}$ . E1 and E2 are completely decoupled. (b) Surface waves obtained by using an electrode geometry where width/gap = 20/35  $\mu\text{m}$ . The shape consists of static peaks and oscillating valley depths. (c) Surface waves obtained by using an electrode geometry where width/gap = 100/100  $\mu\text{m}$ . Two valleys are created above one electrode. (d) Surface waves obtained by using an electrode geometry where width/gap = 15/15  $\mu\text{m}$ . Symmetrical waves are generated with a large amplitude (360 nm).

patterns are used to bring the surface of our coating into motion, which is recorded by DHM measurements. First, a pattern with width/gap = 22/105  $\mu\text{m}$  is used, which results in a 'decoupled' oscillation (Figure 4.6a). Indeed, the shape of the two surface waves are similar to the ones predicted by the simulations. Exactly in the center of the gap area the surface remains static, even as the electric field is applied. Second, the electrode geometry with width/gap = 20/35  $\mu\text{m}$  is investigated, which produces a 'static peaks' oscillation (Figure 4.6b). Due to a small mismatch in the electrode geometry, the tops of the peaks shift about 5  $\mu\text{m}$  during the surface oscillations. The term 'static peaks' is justified as most of

the area covered by the peaks still overlaps in the two activated states. Next, an electrode pattern with width/gap = 100/100  $\mu\text{m}$  is considered, which prompts 'dual contraction' (Figure 4.6c). The surface deforms into an intriguing shape where two valleys and two peaks of different magnitudes follow consecutively. Interestingly, the area in the center of the electrodes seems to be expanding slightly, rather than contracting. This effect is caused by the inhomogeneity of the electric field above the electrode area. Near the edges of the electrode the coating contracts, reducing the distance between the top and bottom electrode, which then increases the electric field strength (and thus the Maxwell stresses) in this area. In the center of the electrodes, the coating is unable to contract so the electric field strength and the Maxwell stresses are smaller here. As a result, during contraction a small portion of the compressed excess of volume can be released at the center of the electrode, simply because the contraction is weaker in that area. Finally, a geometry with width/gap = 15/15  $\mu\text{m}$  is examined, which generates an optimized 'inversion' of the surface topography during the surface oscillation (Figure 4.6d). During the oscillation, maximum height differences of about 360 nm are determined between the top and bottom of the wave. In comparison with the results from chapter 2 where we used the electric circuit from Figure 4.1a and a non-optimized geometry, the amplitude has more than doubled. These results clearly indicate the importance of both electrode and circuit design on the dimensions and shape of the dynamic surface topographies. Lastly, we expect that the four mentioned types of the surface wave can be combined or altered to create other shapes of the surface wave. For example, the 'static peaks' could be combined with 'dual contraction' by reducing the gap distance of the latter from 100  $\mu\text{m}$  to 30  $\mu\text{m}$  while leaving the electrode width unchanged.

## **4.3 Conclusions**

In conclusion, we present an optimization of the circuit and electrode pattern design for a dielectric elastomer coating to produce oscillating surface topographies with increased amplitude and programmable shape. Finite element method simulations are utilized to gain insight into the inherent shape of the oscillating surface wave and how we can use that shape to our advantage. This knowledge is then tested in our experiments to create initially flat coatings that can develop into an oscillating wave with amplitudes of 360 nm, under the influence of a continuous AC electric field at a frequency of 1 Hz. Furthermore, we demonstrate the possibility to program four different types of waves into our coatings, by adjusting the design of our electrode pattern accordingly. The ability to not only control the frequency and amplitude of surface oscillations but also program the shape of the wave, makes these coatings appealing for many applications where surfaces need to perform multiple tasks or switch in functionality. The results of this chapter will be further employed in Chapter 5 where we will study the surface deformation behavior of responsive coatings on more complex, nonlinear electrode structures.

## **4.4 Experimental section**

### **4.4.1 Finite Element Method Simulations**

The electric field induced surface dynamics of the coating were simulated in 3D using Marc Mentat 2014.0.0.

### **4.4.2 Materials**

Interdigitated ITO electrodes were provided by South China Normal University. The poly(dimethyl-siloxane) (PDMS) elastomer and curing agent (Sylgard 184) were obtained from Dow Corning.



### 4.4.3 Sample preparation

The PDMS curing agent was added to the silicone elastomer in a concentration of 2 wt% to obtain a soft and flexible network. After thorough mixing of the two components, the trapped air in the sample was removed under reduced pressure. Before use, the interdigitated ITO substrates with various patterns were cleaned by ultrasonication for 20 min in acetone and isopropanol, respectively, and dried by an airflow. The PDMS mixture was applied on the substrates by spin coating at 7000 rpm (acceleration rate 1000 rpm s<sup>-1</sup>) for 2 min, which produced a coating thickness of 8 μm. The resulting layer of PDMS was cured overnight at 70 °C. After subjecting the PDMS surface to a 10 min UV-ozone treatment, a thin layer of gold (10 nm) was sputter-coated on top of the PDMS layer at a current of 30 mA for 18 s.

### 4.4.4 Characterization

The alternating electric field with a square pulse function was provided by a function generator (Tektronix AFG3252), which was amplified with an amplifier (Falco Systems WMA-300). An in-plane potential difference was generated by a DC Power Supply (3B Scientific U33000). The output voltage was measured with an oscilloscope (Keysight InfiniiVision DSO-X 3032T). The surface topographies were measured with a Digital Holography Microscope (Lyncée Tec.). The thickness of samples was measured by an interferometer (Fogale Nanotech Zoomsurf).

## 4.5 References

- [1] K. Koch, B. Bhushan, W. Barthlott, *Soft Matter* **2008**, *4*, 1943.
- [2] D. W. Bechert, M. Bruse, W. Hage, *Exp. Fluids* **2000**, *28*, 403.
- [3] K. Autumn, Y. A. Liang, S. T. Hsieh, W. Zesch, W. P. Chan, T. W. Kenny, R. Fearing, R. J. Full, *Nature* **2000**, *405*, 681.
- [4] Y. Tian, N. Pesika, H. Zeng, K. Rosenberg, B. Zhao, P. McGuiggan, K. Autumn, J. Israelachvili, *Proc. Natl. Acad. Sci. U. S. A.* **2006**, *103*, 19320.
- [5] B. Bhushan, *J. Adhes. Sci. Technol.* **2007**, *21*, 1213.
- [6] H. Gao, X. Wang, H. Yao, S. Gorb, E. Arzt, *Mech. Mater.* **2005**, *37*, 275.

- [7] J. Genzer, K. Efimenko, *Biofouling* **2006**, *22*, 339.
- [8] T. Mueller, *Natl. Geogr. Mag.* **2008**, *213*, 1.
- [9] X. Gao, L. Jiang, *Nature* **2004**, *432*, 36.
- [10] C. Martin, B. J. Glover, *Curr. Opin. Plant Biol.* **2007**, *10*, 70.
- [11] G. J. Wagner, E. Wang, R. W. Shepherd, *Ann. Bot.* **2004**, *93*, 3.
- [12] F. L. L. Visschers, H. Gojzewski, G. J. Vancso, D. J. Broer, D. Liu, *Adv. Mater. Interfaces* **2019**, *6*, 1.

## Chapter 4

# Chapter 5

## **Patterned surface dynamics at substrate-restricted electroactive silicone coatings**

---

This chapter is partially reproduced from: 'Patterned surface dynamics at substrate-restricted electroactive silicone coatings' F.L.L. Visschers, D.J. Broer, D. Liu, (submitted).

## 5.1 Introduction

In many physical objects, the texture of surfaces plays a crucial role as it affects friction,<sup>[1]</sup> (cell) adhesion,<sup>[2,3]</sup> heat transfer,<sup>[4]</sup> lubrication,<sup>[5]</sup> corrosion,<sup>[6]</sup> wear<sup>[7]</sup> and reflective properties.<sup>[8]</sup> Furthermore, the visual texture of a surface can be used in product design to trigger specific emotions and feelings. The neuropsychological and neuroaesthetic models behind the aesthetic perception of visual textures have been extensively researched.<sup>[9–17]</sup> Additionally, the quantitative characterization of surface textures has been reviewed in multiple books<sup>[18,19]</sup> and research papers,<sup>[20,21]</sup> which further endorses its importance. Nowadays, scientists are exploring methods to provide active control over surface textures by creating dynamic surface micro-structures. Control over these dynamic surfaces provides a major advantage as it grants inherent control over the many functionalities associated with surface textures. Moreover, dynamic surface textures can provide new aspects to aesthetic perceptions and lead to interesting new applications like active mixing in microfluidics or unidirectional transport of matter over a surface. In literature, many examples already exist of coatings that alter their surface structure in response to a variety of external stimuli like pH,<sup>[22]</sup> light,<sup>[23,24]</sup> temperature<sup>[25,26]</sup> and electric fields.<sup>[27–30]</sup> We argue that for electronics-related applications, active control is provided best by using electric fields as a stimulus, as it complies with already integrated driving schemes as for instance used in touch pads for computers and operating systems. In this context, we now present a method to create dynamic pre-programmed surface textures by using a continuously alternating electric field on coatings that consist of a silicon oxide reinforced viscoelastic poly(dimethyl siloxane) network. The principle is based on the results from Chapter 2 where we describe a method generate oscillating waves under a continuous AC electric field in a similar coating.<sup>[31]</sup> In this publication, we apply a similar coating but modify the electrode structures to add desired complexity to the deformation patterns. Based on our models we can predict the complex deformation figures and confirm them by time-resolved

experimental topographical surface analysis. Lastly, we also provide demonstrations of the optical effects that result from the change in texture of our coatings.

## 5.2 Results and discussion

In our approach towards complex surface deformation patterns, we chose a rigid glass substrate provided with lithographically etched indium tin oxide (ITO) electrode patterns. The spin coated electro-active polymer consists of a loosely crosslinked poly(dimethyl siloxane) (PDMS) elastomer that is provided with a thin silicon oxide top layer originated from a UV/ozone treatment.<sup>[31]</sup> On top of the silicon oxide, we sputter coated a thin gold layer which will act as the counter electrode. The sample design is shown in Figure 5.1a. The surface dynamics are induced by the local application of Maxwell stresses. Usually Maxwell stresses are

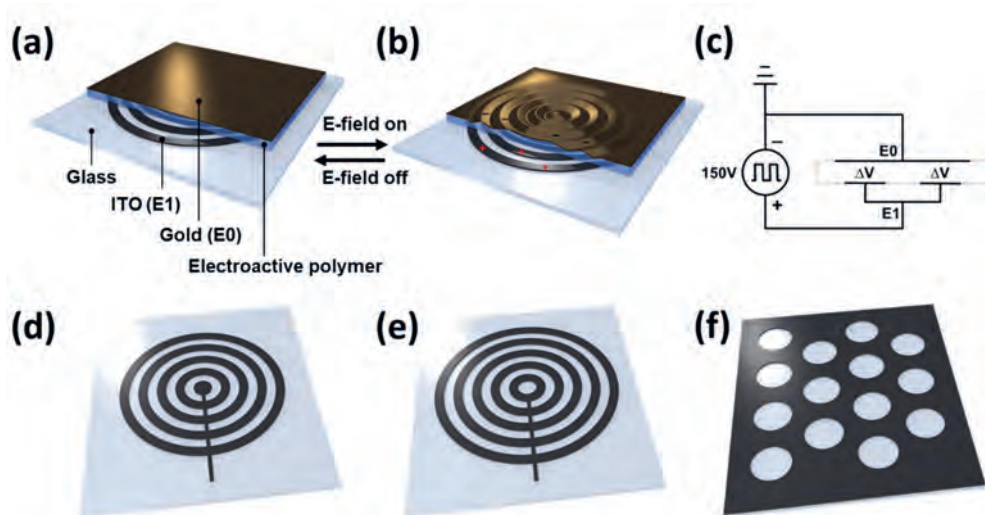


**Figure 5.1** | Design principle of an electroactive polymer coating with switchable surface textures. (a) Schematic representation of the device configuration. (b) By the flick of a switch the coating can alter its topography according to the shape of the ITO electrode underneath. The local application of an electric field induced Maxwell stresses that push excess material away from the ITO electrodes towards the areas in-between (gap). (c) The electric circuit of the device. The electroactive polymer and the two electrodes work as a two-plate capacitor when placed in the external electric field. (d) ITO pattern used to create concentric circles with a valley at the center. (e) ITO pattern used to create concentric circles with a hill at the center. (f) ITO pattern used to create an array of hills.

applied in dielectric elastomers in which two flexible electrodes compress a thin elastomeric film.<sup>[32–35]</sup> The electrostatic attraction between the opposite charges of the two electrodes creates a pressure that expands the surface area while decreasing the thickness of the film. Inspired by this concept we use Maxwell stresses to deform the surface of a coating that is restricted by a rigid substrate. In order to achieve surface deformation, a low modulus of the elastomer material is required. Additionally, Maxwell stresses must be applied locally by using patterned electrodes. When the electric field is applied, the global in-plane displacement is restricted by the rigid substrate. However, since the electric field is applied locally, the compressed excess of volume can escape by the expansion at the gap areas in-between the ITO electrode. The local expansion and contraction of the coating thickness result in a change of the surface's texture (Figure 5.1b). During activation, E0 and E1 are supplied with opposite polarity indicated by  $\Delta V$  in the electric circuit, while the PDMS functions as a capacitor (Figure 5.1c). Typically, the potential difference switches between 0 and 150 V at a frequency between 0 to 5 Hz. Further details of the device preparation and dimensions are provided in the Experimental Section.

In order to predict the deformation mechanics, we schematically reproduced the design of our system in a nonlinear finite element model. For this study, we used the Marc Mentat software with a coupled electrostatic-structural analysis, similar to the simulations used in Chapter 3.<sup>[36,37]</sup> Three different ITO patterns are used to generate three different textures: concentric circles with a valley at the center (CC1, Figure 5.1d), concentric circles with a hill at the center (CC2, Figure 5.1e) and an array of hills (ArC, Figure 5.1f). Upon application of the electric field, the coating contracts above the electrodes and expands above the gap areas in-between the electrodes. Consequently, the surface topography changes from flat and smooth to a shape that matches the pattern of the ITO electrodes underneath (Figures 5.2a to 5.2c). The width of the electrode lines, gap distances and radii of the circles are all 30  $\mu\text{m}$ . In Chapter 4 we have demonstrated that periodic electrode patterns with these proportions yield the best results due to an

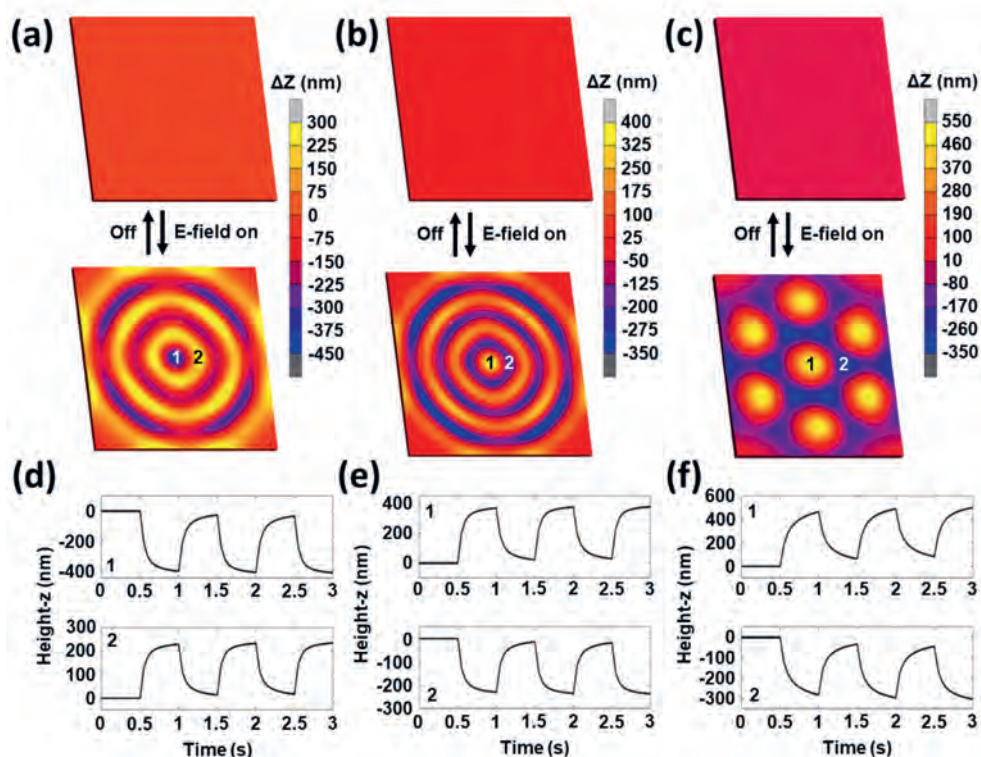


**Figure 5.2** | Simulated results of the electro-mechanical surface dynamics. 3D images showing the initial flat surface and the actuated coating surface when (a) using the CC1 texture, (b) using the CC2 texture and (d) using the ArC texture. The corresponding height changes of the surface from areas 1 and 2 as marked in the figure are shown for (d) the CC1 texture, (e) the CC2 texture and (f) the ArC texture.

optimized balance in electrically activated surface area (Capacitance) and maximum flow-distance of the viscoelastic material.<sup>[38]</sup> In the ArC electrode pattern, circles are packed in a hexagonal lattice to obtain the highest density of hills in the surface texture. In the simulations, the electric field is applied at a potential difference of 150 V and a frequency of 1 Hz. Next, the simulated responses of the coatings are monitored as a function of time at two adjacent locations: above the ITO electrode and above the gaps (Figures 5.2d to 5.2f). The responses obtained from the CC1 and CC2 textures show deformation in opposite directions with height differences of 600 nm, while the ArC texture produces hills with height differences of 780 nm. The difference between the deformation amplitude of ArC textures and CC1 or CC2 textures is caused by the different



shapes of the ITO electrode. The ratio ITO/glass in terms of surface area is larger for ArC textures, resulting in a larger capacitance. Furthermore, each hill created in the ArC texture is pushed upwards from all directions, while a ring in the CC1 or CC2 textures is pushed upwards from only two directions.

The previously discussed FEM simulations demonstrate how different electrode structures can be employed to obtain surface dynamics with complex deformation figures. Now, the predictions from our simulations are verified experimentally, by monitoring the surface topography of the coatings with digital holographic microscopy (DHM). The experiments demonstrate how the surface texture changes in-time as the electric signal is provided at a potential difference of 150 V and a frequency of 1 Hz. In accordance with our simulations, the CC1 pattern creates concentric circles with a valley at the center (Figure 5.3a), while the CC2 pattern results in concentric circles with a hill at the center (Figure 5.3b). Similarly, the ArC texture gives rise to an array of hexagonally packed hills (Figure 5.3c).

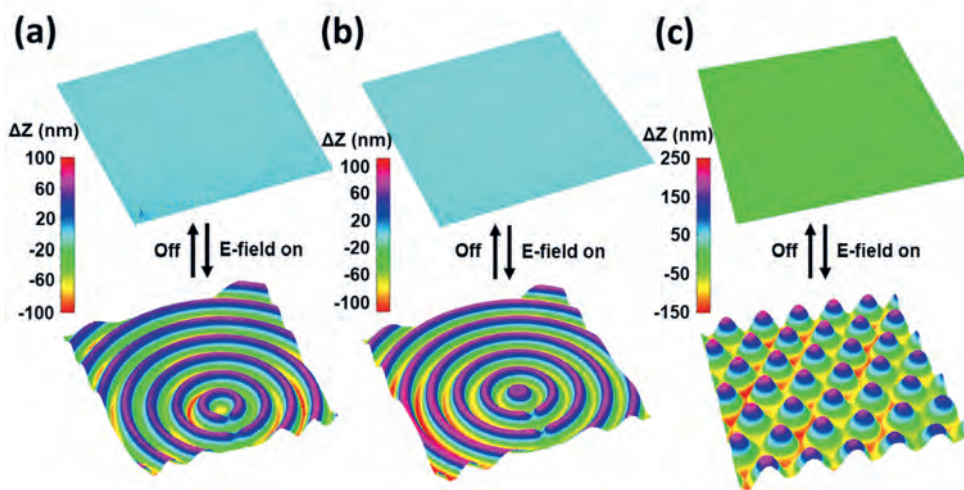


**Figure 5.3** | DHM measurements of the surface topography for different textures. (a) 3D images of the flat and corrugated surface consisting of concentric circles with a valley at the center (CC1). (b) 3D images of the flat and corrugated surface consisting of concentric circles with a hill at the center (CC2). (c) 3D images of the flat and corrugated surface consisting of an array of hexagonally packed hills (ArC)

Next, we further analyze the surface deformation by comparing profile plots of the surface before and after application of the electric field. The profile plots from CC1 and CC2 textures are obtained from the center of the pattern and follow the radius outward (Figures 5.4a and 5.4b). In these figures, the  $z=0$  line corresponds to the reference height at zero voltage. Contraction takes place above the ITO electrode, while expansion occurs in the gap areas in-between resulting in total height differences of 150 nm. The profile plot from the ArC texture covers three neighboring hills and shows total height differences of 300 nm (Figure 5.4c). The experimentally determined height differences are significantly smaller than those from our FEM simulations. This large difference is most likely caused by the resistance in the electrical circuit that results in lower voltage output. From our FEM model we can estimate that the effective potential difference in our device

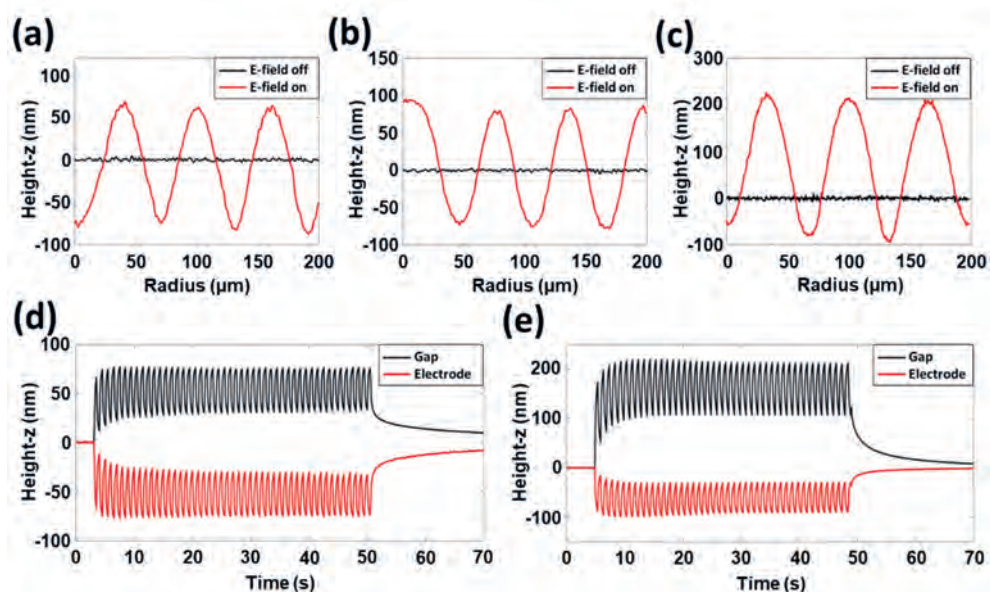


**Figure 5.4 |** Details of the surface deformations and dynamics. (a) The 2D profile of the concentric circles with a valley at the center, corresponding to Figure 5.2a. The profile is taken from the center of the pattern and follows the radius outward. (b) The 2D profile of the concentric circles with a hill at the center, corresponding to Figure 5.2b. The profile is taken from the center of the pattern and follows the radius outward. (c) The 2D profile with the array of hills, corresponding to Figure 5.2c. The profile is taken over three neighboring hills. (d) Dynamics of the surface topographies at a frequency of 1 Hz for a pattern of concentric circles. (e) Dynamics of the surface topographies at a frequency of 1 Hz for a pattern with an array of circles.

is 75V. Based on the exact correspondence between modeled and experimental deformations generated in the past, we anticipate that the experimental deformation can be further enhanced, for instance by selecting thicker ITO layers to reduce the resistance. To continue the analysis, we investigate the oscillating behavior of the CC1 and CC2 textures by monitoring the time-resolved electro-mechanic response of the coating above the ITO electrode and the gap areas in-between (Figure 5.4d). At a frequency of 1 Hz, the surface dynamics reach a steady state after the first four periods, at which point the structure oscillates 90 nm in height. After removal of the electric field, the surface relaxes back to its original flat shape in 40 seconds. The dynamics of the ArC textures show slightly different behavior (Figure 5.4e). At a frequency of 1 Hz, the surface dynamics now reach a steady state after six periods, which is caused by the larger scale of the deformation. The height change of the hills is 170 nm during the oscillations, while the relaxation of the surface still takes 40 seconds after removal of the electric field.

Lastly, we present demonstrations of the optical effects that occur when the surface of our coatings changes the texture. First, we use an optical microscope in the reflection mode to show how the reflection of collimated light from the top gold layer changes (Figure 5.5a). Initially, the surface is flat and with homogeneous brightness over the entire surface. As soon as the electric field is applied, the surface deforms which moves the hills of the surface into focus and increases the brightness locally. Simultaneously, the valleys move out of focus which decreases the brightness in these areas and is further enhanced by deflection of the light at oblique surfaces at the structure walls. As a result, the pattern of the surface deformation is visible by alternating dark and bright lines. This effect also occurs above the thin line connecting each ring in the ITO pattern. Second, we use a regular video camera to record the macroscopic effects of the surface deformations (Figures 5.5b and 5.5c). The camera is placed at an angle with respect to the normal of the surface, to capture the diffuse light that is reflected. Again, the initial surface is smooth and reflects light homogeneously

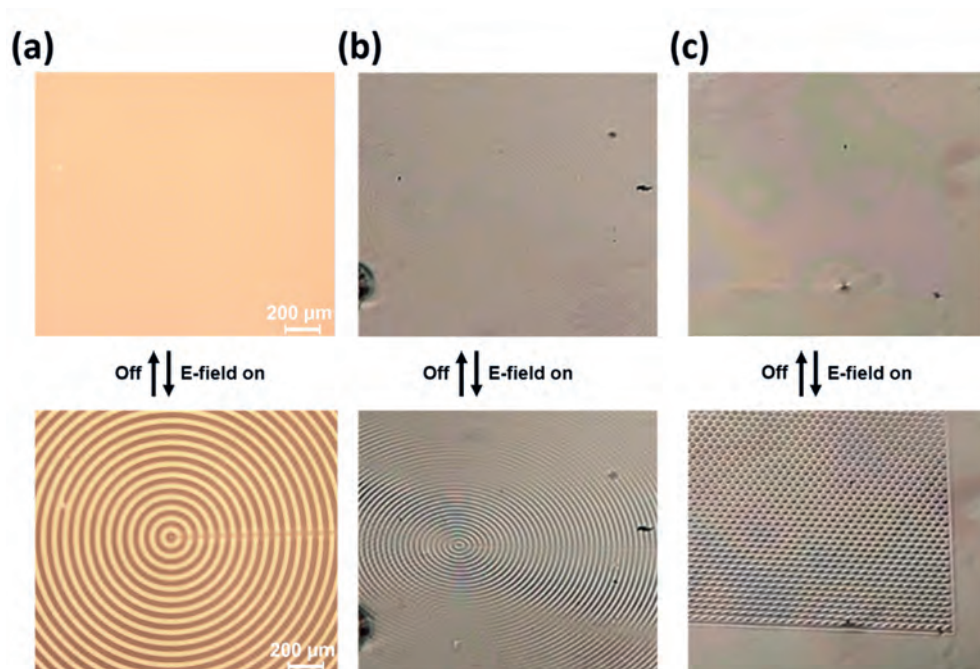


**Figure 5.5** | The visual changes in reflection resulting from the change in surface texture. (a) Images from an optical microscope using the reflection mode. Initially the surface reflects light homogeneously. After application of the electric field the reflection is changed by the pattern of the surface. (b) Images from a camera capturing the change in texture of the coating as the electric field is applied creating concentric circles. (c) Images from a camera capturing the change in texture of the coating as the electric field is applied creating an array of hills.

over the surface, while the pattern of ITO underneath the surface is hardly distinguishable. Next, the electric field is applied and the change in the texture of the surface is clearly visible. The gloss and reflective properties of the gold surface combined with the drastic change in surface topography are essential to obtain a visible change in the texture of the coating.

### 5.3 Conclusions

In conclusion, we have presented a method to obtain dynamic and reversible textural changes in the surface of a dielectric elastomer coating under an AC electric field. The pattern of the textures is controlled by the pattern of the ITO electrode, hidden underneath the surface of the elastomer. The height of the micro-structures is controlled by the electric field strength and can oscillate at

frequencies between 0 and 5 Hz. Finite element method simulations are applied to support our experimental results and predict further optimization of the deformation is possible by improvement of the connections within our electrical circuit. The simulations can also be used to predict the results of experiments with complex ITO patterns and electric circuits to obtain more interesting surface textures. The optical effects of the changing surface structures are demonstrated microscopically and macroscopically.

## **5.4 Experimental section**

### **5.4.1 Finite Element Method Simulations**

The electric field induced surface dynamics of the coating were simulated in 3D using Marc Mentat 2014.0.0.

### **5.4.2 Materials**

Glass substrates with the patterned ITO electrodes were provided by South China Normal University. The poly(dimethyl-siloxane) (PDMS) elastomer and curing agent (Sylgard 184) were obtained from Dow Corning.

### **5.4.3 Sample preparation**

The PDMS curing agent was added to the silicone elastomer in a concentration of 2 wt% to obtain a soft and flexible network. After thorough mixing of the two components, the trapped air in the sample was removed under reduced pressure. Prior to use, the ITO substrates with various patterns were cleaned by ultrasonication for 20 min in acetone and isopropanol, respectively, and dried by an air-flow. The PDMS mixture was applied on the substrates by spin coating at 7000 rpm (acceleration rate  $1000 \text{ rpm s}^{-1}$ ) for 2 min, which produced a coating thickness of 8  $\mu\text{m}$ . The resulting layer of PDMS was cured overnight at 70 °C.

After subjecting the PDMS surface to a 10 min UV-ozone treatment, a thin layer of gold (10 nm) was sputter coated on top of the PDMS layer at a current of 30 mA for 18 s.

#### 5.4.4 Characterization

The alternating electric field with a square pulse function was provided by a function generator (Tektronix AFG3252), which was amplified with an amplifier (Falco Systems WMA-300). The output voltage was measured with an oscilloscope (Keysight InfiniiVision DSO-X 3032T). The surface topographies were measured with a Digital Holography Microscope (Lyncée Tec.). The thickness of samples was measured by an interferometer (Fogale Nanotech Zoomsurf). The microscope images were obtained from a polarized optical microscope (Leica DM2700) in reflection mode. Photographs and movies were taken with a digital camera (Nikon D7200, Olympus OM-D E-M10 Mk III) in manual mode.

## 5.5 References

- [1] M. M. Koura, *Wear* **1980**, *63*, 1.
- [2] J. Chen, S. Mwenifumbo, C. Langhammer, J. P. McGovern, M. Li, A. Beye, W. O. Soboyejo, *J. Biomed. Mater. Res. - Part B Appl. Biomater.* **2007**, *82*, 360.
- [3] A. K. Geim, S. V. Dubonos, I. V. Grigorieva, K. S. Novoselov, A. A. Zhukov, S. Y. Shapoval, *Nat. Mater.* **2003**, *2*, 461.
- [4] D. Attinger, C. Frankiewicz, A. R. Betz, T. M. Schutzius, R. Ganguly, A. Das, C.-J. Kim, C. M. Megaridis, *MRS Energy Sustain.* **2014**, *1*, 1.
- [5] Y. H. Lee, J. K. Schuh, R. H. Ewoldt, J. T. Allison, *J. Mech. Des. Trans. ASME* **2017**, *139*, 1.
- [6] P. R. Seré, J. D. Culcasi, C. I. Elsner, A. R. Di Sarli, *Surf. Coatings Technol.* **1999**, *122*, 143.
- [7] A. Khellouki, J. Rech, H. Zahouani, *Wear* **2007**, *263*, 81.
- [8] S. C. Baker-Finch, K. R. McIntosh, *Prog. Photovoltaics Res. Appl.* **2011**, *19*, 406.
- [9] A. Chatterjee, O. Vartanian, *Ann. N. Y. Acad. Sci.* **2016**, *1369*, 172.
- [10] S. Koelsch, A. M. Jacobs, W. Menninghaus, K. Liebal, G. Klann-Delius, C. von Scheve, G. Gebauer, *Phys. Life Rev.* **2015**, *13*, 1.
- [11] L. P. Kirsch, C. Urgesi, E. S. Cross, *Neurosci. Biobehav. Rev.* **2016**, *62*, 56.
- [12] H. Leder, B. Belke, A. Oeberst, D. Augustin, *Br. J. Psychol.* **2004**, *95*, 489.
- [13] H. Leder, M. Nadal, *Br. J. Psychol.* **2014**, *105*, 443.
- [14] J. Liu, E. Lughofer, X. Zeng, *Neurocomputing* **2015**, *168*, 947.
- [15] J. Liu, E. Lughofer, X. Zeng, *Front. Comput. Neurosci.* **2015**, *9*, 1.
- [16] S. Thumfart, R. H. A. H. Jacobs, E. Lughofer, C. Eitzinger, F. W. Cornelissen, W. Groissboeck,

- R. Richter, *ACM Trans. Appl. Percept.* **2011**, *8*.
- [17] C. Redies, *Front. Hum. Neurosci.* **2015**, *9*, 1.
- [18] R. Leach, *Characterisation of areal surface texture*, Leach, R., Ed.; Springer: Teddington, 2013.
- [19] L. Blunt, X. Jiang, *Assessment Surface Topography*, 2003.
- [20] L. De Chiffre, P. Lonardo, H. Trumpold, D. A. Lucca, G. Goch, C. A. Brown, J. Raja, H. N. Hansen, *CIRP Ann.* **2000**, *49*, 635.
- [21] S. Pomberger, M. Stoschka, M. Leitner, *Precis. Eng.* **2019**, *60*, 465.
- [22] Z. Dang, L. Liu, Y. Li, Y. Xiang, G. Guo, *ACS Appl. Mater. Interfaces* **2016**, *8*, 31281.
- [23] G. Babakhanova, H. Yu, I. Chaganava, Q. H. Wei, P. Shiller, O. D. Lavrentovich, *ACS Appl. Mater. Interfaces* **2019**, *11*, 15007.
- [24] D. Liu, D. J. Broer, *Angew. Chemie Int. Ed.* **2014**, *53*, 4542.
- [25] Q. Hao, W. Li, H. Xu, J. Wang, Y. Yin, H. Wang, L. Ma, F. Ma, X. Jiang, O. G. Schmidt, P. K. Chu, *Adv. Mater.* **2018**, *30*, 1.
- [26] B. Wang, X. Xue, X. Liu, P. Neuzžil, B. Ma, W. Yuan, J. Luo, C. Jiang, *Appl. Mater. Today* **2018**, *13*, 271.
- [27] S. Shian, D. R. Clarke, *Soft Matter* **2016**, *12*, 3137.
- [28] W. Feng, D. J. Broer, D. Liu, *Adv. Mater.* **2018**, *1704970*, 1.
- [29] D. Pyo, S. Ryu, K. U. Kyung, S. Yun, D. S. Kwon, *Appl. Phys. Lett.* **2018**, *112*, 1.
- [30] E. M. Henke, K. E. Wilson, I. A. Anderson, *Bioinspiration and Biomimetics* **2018**, *13*, 1.
- [31] F. L. L. Visschers, H. Gojzewski, G. J. Vancso, D. J. Broer, D. Liu, *Adv. Mater. Interfaces* **2019**, *6*, 1.
- [32] S. M. Ha, W. Yuan, Q. Pei, R. Pelrine, S. Stanford, *Adv. Mater.* **2006**, *18*, 887.
- [33] N. America, B. C. Burchfiel, P. W. Lipman, T. Parsons, G. Soc, A. Bull, A. Tovish, G. Schubert, B. P. Luyendyk, R. Pelrine, R. Kornbluh, Q. Pei, J. Joseph, *Science.* **2000**, *287*, 836.
- [34] S. Michel, X. Q. Zhang, M. Wissler, C. Löwe, G. Kovacs, *Polym. Int.* **2010**, *59*, 391.
- [35] R. E. Pelrine, R. D. Kornbluh, J. P. Joseph, *Sensors Actuators, A Phys.* **1998**, *64*, 77.
- [36] MSC Software, *MSC. Softw. Corp.* **2014**, *Volume A*, 360.
- [37] MSC Software, *MSC. Softw. Corp.* **2014**, *Volume B*, 130.
- [38] F. Visschers, D. J. Broer, D. Liu, *Proc. SPIE* **2020**, *11375*, 1.

# Chapter 6

## High-frequency surface dynamics in electroactive polymer coatings with SU-8 microstructures

---

This chapter is partially reproduced from: 'High-frequency surface dynamics in electroactive polymer coatings with SU-8 microstructures' F.L.L. Visschers, J. Massaad, P. van Neer, D. Liu, D.J. Broer (manuscript in preparation).



## 6.1 Introduction

In nature, surfaces that separate organisms from their environment are often modified to perform a specific task such as self-cleaning,<sup>[1,2]</sup> (anti)-adhesion,<sup>[3-6]</sup> camouflage,<sup>[7]</sup> signaling<sup>[8]</sup> and temperature control.<sup>[9]</sup> Inspired by nature, many coatings have been developed that add dynamic properties like switchable surface morphologies in response to external stimuli like pH,<sup>[10]</sup> light,<sup>[11,12]</sup> temperature<sup>[13,14]</sup> and electric fields.<sup>[15-20]</sup> As mentioned in Chapter 1, electric field responsive coatings in particular, have the opportunity to provide a high-frequency input, which in turn can potentially lead to a high-frequency output in terms of surface dynamics. So far however, electric-field responsive coatings have demonstrated surface dynamics that are still in the low-frequency range below 1 kHz. Coatings that would display dynamic morphologies at higher frequencies could expand the range of applications to, for instance, acoustics (non-destructive testing<sup>[21]</sup> and medical imaging<sup>[22]</sup>) and communication optics.<sup>[23]</sup>

The previous chapters in this thesis described methods to generate dynamic surface topographies at soft viscoelastic polymer coatings. Although we have demonstrated great control over the shape and amplitude of the formed topographies in these systems, the frequency range is still limited to a maximum of 5 Hz by the viscoelastic properties. In this context, we now present a new method to create high-frequency surface dynamics controlled by continuously alternating electric fields on a coating that consists of an elastic poly(dimethyl siloxane) network supported by SU-8 microstructures. Finite element method (FEM) simulations are employed to guide our experimental setup and to help with the understanding of the deformation under a DC electric field. Digital holographic microscopy (DHM) measurements are used to confirm the predicted deformations at relatively low frequencies. Excitingly, and in agreement with the objectives of this chapter, when using alternating electric fields, we discovered resonance effects that occur at frequencies up to 230 kHz. Controlled by the high

frequency alternating electric field, the local surface vibrations demonstrate impressive amplitudes and speeds.

## 6.2 Results and discussion

In our method to obtain high-frequency surface dynamics, we have created SU-8 microstructures on a rigid glass substrate provided with a continuous conductive layer of indium tin oxide (ITO, E1). The microstructures support a spin coated electroactive polymer that consists of a poly(dimethyl-siloxane) (PDMS) elastomer with a higher crosslink density than in the previous chapters, to reduce the viscoelastic component in the mechanical dynamics. On top of the PDMS elastomer we sputter coated a thin layer of gold which serves as a flexible top electrode (E0). The sample design is shown in Figure 6.1a. The surface vibrations

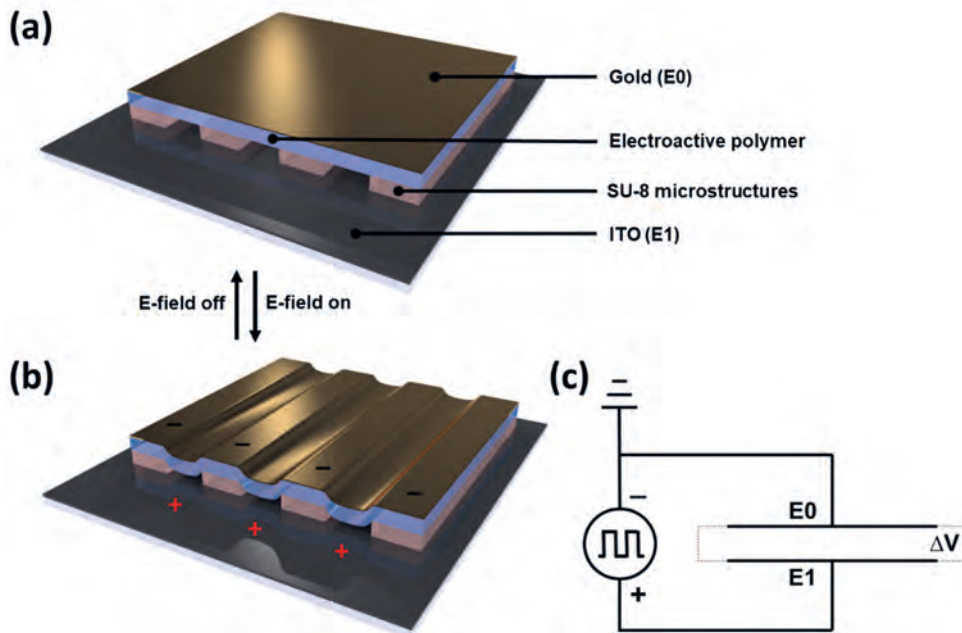


**Figure 6.1** | Design principle of an electroactive polymer coating with switchable surface topography. (a) Schematic representation of the device configuration. (b) After application of the electric field, the surface can alter its topography according to the programmed SU-8 structure underneath. As the pockets collapse, their content is pushed out of the sample via escape points at the edges of the samples. (c) The electric circuit of the device. The electroactive polymer combined with the microstructured SU-8 work as a two-plate capacitor when placed in the external electric field.

are produced by periodically induced Maxwell stresses, commonly used to compress dielectric elastomers where a thin elastomeric film is sandwiched between two flexible electrodes in a two-plate capacitor setup.<sup>[24-27]</sup> When Maxwell stresses compress our coatings, the global in-plane displacement is locally prohibited by the rigid microstructures on the substrate. In-between the microstructures however, the film can be stretched to fill the previously unoccupied space resulting in a deformation of the coating's surface (Figure 6.1b). As the pockets collapse, air can freely flow out of the coating via escape points at the edges of the sample. To initiate a surface deformation, E0 and E1 are supplied with opposite polarity indicated by  $\Delta V$  in the electric circuit (Figure 6.1c), typically the voltage ranges from 150 V to 210 V. Further details of the device preparation and dimensions are provided in the Experimental Section.

To predict the deformation mechanics and to guide our experimental setup, we schematically reproduced the design of our system in the nonlinear FEM software of Marc Mentat, using a coupled electrostatic-structural analysis. The mechanical properties of the elastomer in the model have been adjusted and are now different from previous chapters. In the simulations the gap distances between the microstructures are 100  $\mu\text{m}$ , which is also the width of the microstructures themselves. Upon applying an electric field with a potential of 210 V, the surface topography changes dramatically due to a partial collapse of the air pockets (Figures 6.2a and 6.2b). Directly above the microstructures, the Maxwell stresses are resisted and no significant contraction is determined. In-between the microstructures, only the elastic PDMS counteracts the Maxwell stress and a contraction of more than 3  $\mu\text{m}$  is observed. Next, the contraction above the gap areas is calculated using various gap distances and plotted as a function of the applied potential difference (Figure 6.2c). The results indicate that the gap distance has a large influence on the magnitude of the contraction. This effect is explained by the decrease of the elastic counter-force as the gap distance between the microstructures increases. On top of that, a larger gap distance increases the effective surface area where the Maxwell stress is applied, which results in a larger

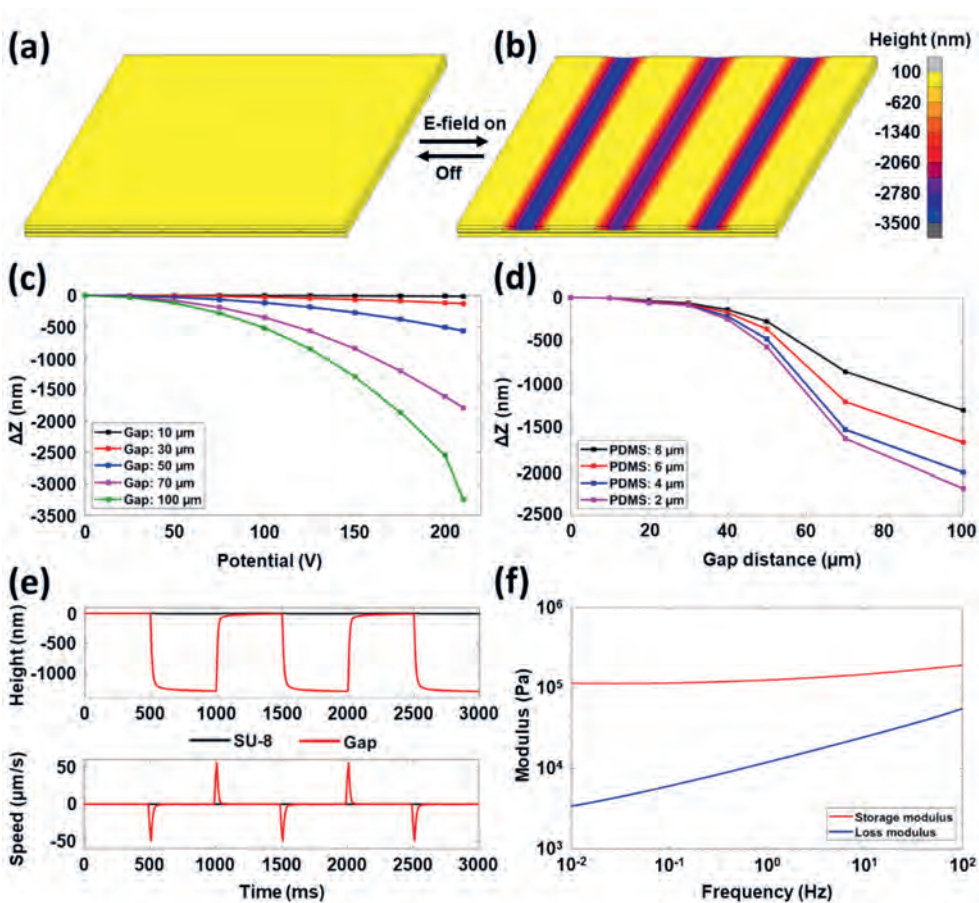


**Figure 6.2** | Simulated results of the electro-mechanical surface dynamics. Simulated 3D images showing (a) the initial coating surface and (b) the actuated coating surface when subjected to an electric field at a DC potential of 210 V. (c) Influence of the applied potential difference on the deformation amplitude at various gap distances. (d) Influence of the gap distance on the deformation amplitude using various thicknesses of the elastic PDMS at DC potentials of 150 V. (e) The predicted change in surface height and deformation speed above the SU-8 (black) and above the gap area (red). The gap distance is 100  $\mu\text{m}$  and the electric field switches at a frequency of 1 Hz between 0 and 150 V. (f) Measured storage modulus  $G'$  and loss modulus  $G''$  when the coating is subjected to a frequency sweep at 5% strain.

compressive force. To continue our analysis, we simulate how the thickness of the PDMS top film affects the contraction occurring at several different gap distances (Figure 6.2d). In these simulations the applied potential difference is lowered from 210 V to 150 V, to prevent compilation errors that occur when large strains are generated. The results indicate that a thinner PDMS layer results in a larger contraction, which is explained by the increase in the electric field strength

as well as by the decrease in elastic counterforce. Moving forward, we use the developed model to also predict the kinetics of the surface dynamics. The surface is brought into motion using an alternating electric field at a frequency of 1 Hz with a peak to peak potential difference of 150 Vpp. The simulated response of the coating is monitored as a function of time at two adjacent locations: above the SU-8 and above the gap (Figure 6.2e). The simulations predict a height difference of more than 1  $\mu\text{m}$  occurring at a maximum speed of 50  $\mu\text{m/s}$ . The quick response of the coating to the alterations in the electric field indicates that the elastic properties of the material control the deformation. The fast elastic response is expected as the frequency-dependent storage ( $G'$ ) and loss ( $G''$ ) moduli, which were used to describe the viscoelastic properties in the FEM model, do not indicate the presence of a strong viscous component (Figure 6.2f).

The previously discussed FEM simulations predict a quick response and large surface deformation for our coating design. Now, the proposed actuation principle is demonstrated experimentally by monitoring the surface deformation with DHM measurements. Prior to actuation, the coating surface shows a small relief matching the shape of the SU-8 microstructures underneath, which is a result of the fabrication process (Figures 6.3a and 6.3c (black curve)). Upon applying the electric field with a potential of 210 V, the air pockets in-between the SU-8 microstructures partially collapse resulting in a large surface deformation with contraction of more than 2  $\mu\text{m}$  (Figures 6.3b and 6.3c (red curve)). Next, we further analyze the surface deformation by extracting the time-resolved electro-mechanical response of the coating at two adjacent locations (Figure 6.3d). The first location is positioned directly above the SU-8 material, while the second location is placed above the center of the gap area. The initial deformation occurs fast with a slight overshoot that takes a few minutes to equilibrate. The long equilibration time, compared to the fast initial surface deformation, is caused by the interplay between the Maxwell stress and the elastic counter-force. During the overshoot, the electric field strength in the gap area increases significantly because the top and bottom electrodes draw closer (Figure 6.3f). As a result, the

Maxwell stress also increases and works against the elastic-counter force, which prolongs the equilibration process of the surface deformation. To continue the analysis of the deformation, the influence of the gap distance in-between the microstructures is also determined at various DC potentials (Figure 6.3e). As predicted by our FEM simulations, adjusting the geometry of the microstructures has a large impact on the maximum contraction of the surface.

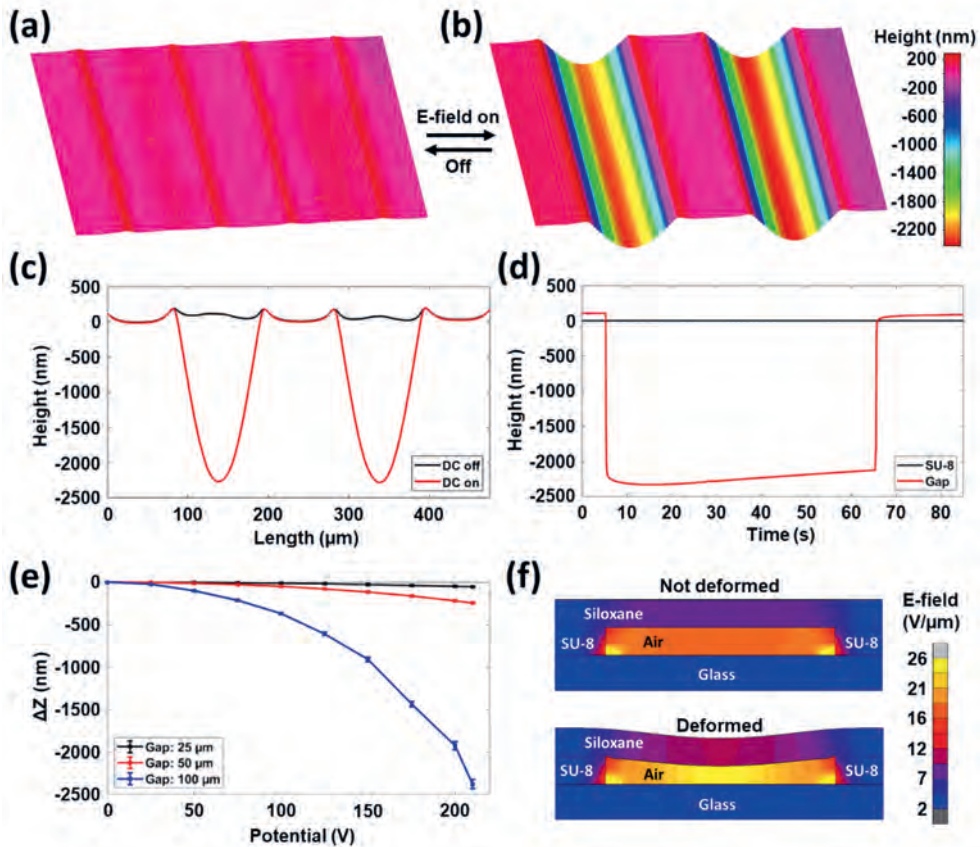


**Figure 6.3** | Details of the electro-mechanical surface deformation. 3D images measured by DHM show (a) the small surface relief without electric field and (b) the surface of the coating when subjected to an electric field at a DC potential of 210 V. (c) The corresponding 2D profile of Figures 6.3a and 6.3b. The black curve shows the surface profile without electric field, while the red curve is measured when the electric field is applied. (d) Measured change of the surface height above the SU-8 (black) and above the gap area (red). (e) Influence of the electric field strength on the contraction above the gap area for microstructures with various gap distances. (f) The results from FEM simulations of the electric field distribution in cross sections of the coating. The top image shows the electric field distribution in the original shape, while the bottom image shows how the field distribution changes as the coating deforms.

Finally, the kinetics of the surface dynamics are extracted from the time-resolved DHM measurements. First, the surface is brought into a vibrating motion using a pulse generator at a frequency of 1 Hz with a peak-to-peak potential difference of 150 Vpp, similar to our FEM simulation. Two key locations above the SU-8 and the center of the gap are tracked while monitoring the applied electric field (Figure 6.4a). In close resemblance to our predictions, the surface reacts with a rapid elastic like deformation upon switching of the electric field. Height differences of more than 800 nm are measured at a maximum deformation speed of 20  $\mu\text{m/s}$ . Interestingly, both experimental and simulated results show that the return of the coating to its original shape occurs faster than the initial deformation. This effect is caused by the instant release of the stored elastic energy in the coating when the pressure from the electric field is removed. Subsequently, the surface vibrations are measured during a frequency sweep (Figure 6.4b). Initially, as the frequency increases, the amplitude of the deformation dwindles. However, within the frequency range from 100 to 10 000 Hz, the contraction magnitude remains consistent between 150 and 200 nm. Then, remarkably, the amplitude of the surface vibrations increases again, and a resonance frequency is discovered at 230 kHz. A more detailed analysis of the surface vibration at this resonance frequency reveals a sine shaped temporal motion of the PDMS film (Figure 6.4c). The obtained deformation amplitude is 600 nm, which is generated at a maximum speed of almost 500  $\mu\text{m/s}$ . In comparison, we achieved maximum surface displacement speeds of 5  $\mu\text{m/s}$  in our previously described systems (Chapter 2).<sup>[18]</sup>

To obtain a better understanding of the surface vibrations, we take a closer look at how the shape of the temporal wave changes as the frequency is increased (Figure 6.4d). Increasing the frequency from 1 Hz to 10 Hz to 1000 Hz, results in a shape change from a square wave to a triangle wave and back to a square wave. We postulate that at 10 Hz this shape change is related to the time required by the electric field to overcome an energy threshold generated by the elastic counter-force. At 100 Hz the deformation becomes sufficiently small to be less

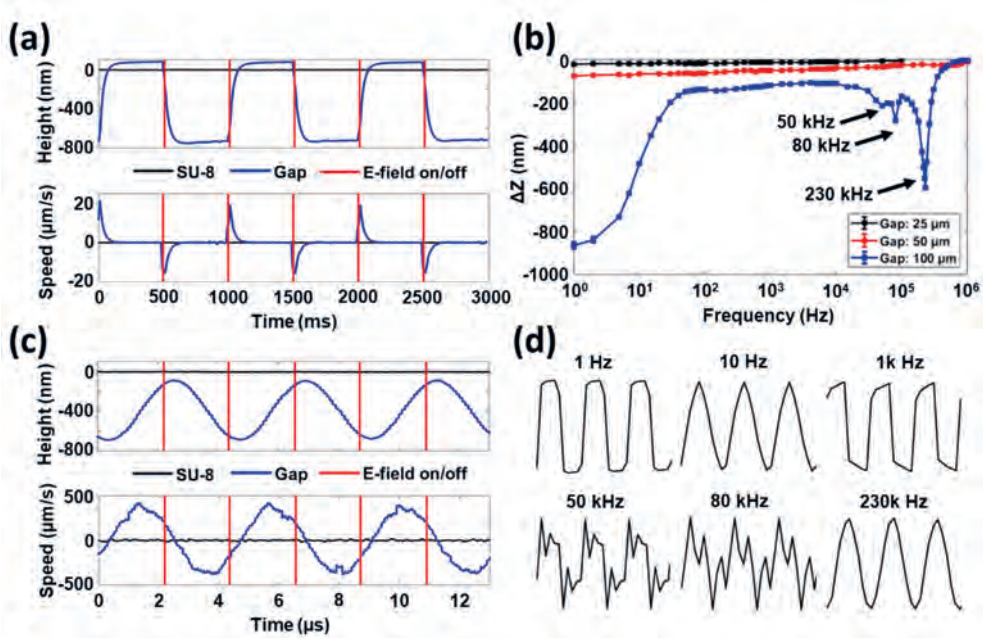


**Figure 6.4** | DHM measurements from electric field induced surface vibrations. (a) The change in surface height and deformation speed using an AC potential of 150 Vpp at a frequency of 1 Hz. The gap distance is 100  $\mu\text{m}$ . Vertical red lines indicate the moment the electric field switches on or off. (b) Influence of the frequency on the deformation amplitude. (c) The change in surface height and deformation speed using an AC potential of 150 Vpp at a frequency of 230 kHz. (d) The shape of the temporal wave measured at several key frequencies.

hindered by this restriction and a square response is the result. Then, the frequency is increased further and a small peak in amplitude is observed at a frequency of 50 kHz. At this frequency, the sampling rate is high enough to distinguish a ringing effect, which occurs in signals that are produced with a square wave. When using a square wave, the device is offered an infinitely broad frequency spectrum of excitations, including the eigen frequencies of the system. At a frequency of 50 kHz, the timing of the electric field lines up with the ringing effect and five oscillations take place during one period of the applied electric field. This constructive interference enhances the amplitude of the surface vibrations. Similarly, at 80 kHz three oscillations of the ringing effect take place during one period of the applied electric field. Finally, the shape of the wave changes to a sine at a frequency of 230 kHz, which signifies the surface vibrates at a fundamental frequency. The position of the resonance peak is determined



by the geometric constraints of the microstructure and the thickness and modulus of the PDMS film. Future experiments are planned to further tune the fundamental frequency by altering these parameters.

## **6.3 Conclusions**

In conclusion, we have developed a new method to obtain large topographical changes in the surface of a coating under a DC electric field, as well as high-frequency surface vibrations triggered by an AC electric field. Our approach is based on the generation of Maxwell stress in a film supported by SU-8 microstructures. The air pockets in-between the micro-structures can partially collapse under the pressure from the electric field, resulting in a large change of the surface topography, as supported by finite element method simulations. When using AC electric fields, the surface vibrates and a fundamental frequency is discovered at 230 kHz. The obtained deformation amplitude of 600 nm is reached at a speed of almost 500  $\mu\text{m/s}$ . Due to the combination of high-frequency vibrations and large deformation amplitudes, we anticipate that the application potential is large, ranging from haptics and microfluidics to acoustics and optics. Future research is focused on obtaining control over the position of the resonance frequency and the application in acoustic devices by producing sound waves underwater.

## **6.4 Experimental section**

### **6.4.1 Finite Element Method Simulations**

The electric field induced surface deformations of the coating were simulated in 3D using Marc Mentat 2014.0.0.

## 6.4.2 Materials

Glass substrates with a continuous ITO electrode were obtained from GemTech Optoelectronics. The poly(dimethyl-siloxane) (PDMS) elastomer and curing agent (Sylgard 184) were obtained from Dow Corning. The SU-8 2010 microresist was obtained from MicroChem.

## 6.4.3 Sample preparation

The PDMS curing agent was added to the silicone elastomer in a ratio of 1:10 (as recommended by the manufacturer) to obtain a flexible elastomer network. After thorough mixing of the two components, the trapped air in the sample was removed under reduced pressure. The substrates with the ITO electrode (100 nm thickness) were cleaned by ultrasonication for 20 minutes in acetone and isopropanol, respectively, and dried with air-flow. Subsequently, the clean substrates were subjected to a UV-ozone treatment for 20 minutes. The SU-8 2010 was applied on the substrates by spincoating first at 500 rpm (acceleration rate 100 rpm/s) for 5 seconds and then at 4000 RPM (acceleration rate 300 rpm/s) for 30 seconds, which resulted in a thickness of 9  $\mu\text{m}$ . After a softbake of 10 minutes at 95  $^{\circ}\text{C}$ , the sample was exposed to UV light through a photomask at 10  $\text{mW}/\text{cm}^2$  for 12.5 seconds. Next, the PDMS mixture was applied on the substrates by spincoating at 7000 rpm (acceleration rate 1000 rpm/s) for 2 minutes, which resulted in a thickness of 7  $\mu\text{m}$ . The samples were then heated to 95  $^{\circ}\text{C}$  for 1 hour for the curing of the PDMS and the post-exposure bake of the SU-8. After the post-exposure bake, the samples were developed in propylene glycol monomethyl ether acetate for 3 days. A thin layer of gold (10 nm) was sputtercoated on top of the PDMS layer at a current of 65 mA for 11 seconds.

#### 6.4.4 Characterization

The alternating electric field with a square pulse function was provided by a function generator (Tektronix AFG3252). The electric signal from the function generator was then amplified with an amplifier (Falco Systems WMA-300). The DC potential difference was generated by a DC Power Supply (3B Scientific U33000). The output voltage was measured with an oscilloscope (Keysight InfiniiVision DSO-X 3032T). The surface topographies were measured with a Digital Holography Microscope (Lyncée Tec.). The thickness of samples was measured by an interferometer (Fogale Nanotech Zoomsurf). The mechanical properties of PDMS were measured with an oscillatory frequency sweep by a rheometer (AR-G2, TA instruments) with a strain of 5%.

#### 6.5 References

- [1] C. Neinhuis, W. Barthlott, *Ann. Bot.* **1997**, *79*, 667.
- [2] R. Fürstner, W. Barthlott, C. Neinhuis, P. Walzel, *Langmuir* **2005**, *21*, 956.
- [3] L. Q. Ren, S. J. Wang, X. M. Tian, Z. Q. Han, L. N. Yan, Z. M. Qiu, *J. Bionic Eng.* **2007**, *4*, 33.
- [4] Y. Tian, N. Pesika, H. Zeng, K. Rosenberg, B. Zhao, P. McGuiggan, K. Autumn, J. Israelachvili, *Proc. Natl. Acad. Sci. U. S. A.* **2006**, *103*, 19320.
- [5] K. Autumn, Y. A. Liang, S. T. Hsieh, W. Zesch, W. P. Chan, T. W. Kenny, R. Fearing, R. J. Full, *Nature* **2000**, *405*, 681.
- [6] R. Leach, *Characterisation of areal surface texture*; Leach, R., Ed.; Springer: Teddington, 2013.
- [7] J. Teyssier, S. V. Saenko, D. Van Der Marel, M. C. Milinkovitch, *Nat. Commun.* **2015**, *6*, 1.
- [8] H. C. Hoch, R. C. Staples, B. Whitehead, J. Comeau, E. D. Wolf, *Science*. **1987**, *235*, 1659.
- [9] L. B. Pérez-Estrada, Z. Cano-Santana, K. Oyama, *Tree Physiol.* **2000**, *20*, 629.
- [10] Z. Dang, L. Liu, Y. Li, Y. Xiang, G. Guo, *ACS Appl. Mater. Interfaces* **2016**, *8*, 31281.
- [11] G. Babakhanova, H. Yu, I. Chaganava, Q. H. Wei, P. Shiller, O. D. Lavrentovich, *ACS Appl. Mater. Interfaces* **2019**, *11*, 15007.
- [12] D. Liu, D. J. Broer, *Angew. Chemie Int. Ed.* **2014**, *53*, 4542.
- [13] Q. Hao, W. Li, H. Xu, J. Wang, Y. Yin, H. Wang, L. Ma, F. Ma, X. Jiang, O. G. Schmidt, P. K. Chu, *Adv. Mater.* **2018**, *30*, 1.
- [14] B. Wang, X. Xue, X. Liu, P. Neuzžil, B. Ma, W. Yuan, J. Luo, C. Jiang, *Appl. Mater. Today* **2018**, *13*, 271.
- [15] D. Liu, N. B. Tito, D. J. Broer, *Nat. Commun.* **2017**, *8*, 1.
- [16] D. Pyo, S. Ryu, K. U. Kyung, S. Yun, D. S. Kwon, *Appl. Phys. Lett.* **2018**, *112*, 1.
- [17] S. Shian, D. R. Clarke, *Soft Matter* **2016**, *12*, 3137.
- [18] F. L. L. Visschers, H. Gojzewski, G. J. Vancso, D. J. Broer, D. Liu, *Adv. Mater. Interfaces* **2019**,

6, 1.

- [19] F. Visschers, D. J. Broer, D. Liu, *Proc. SPIE* **2020**, 11375, 1.
- [20] E. M. Henke, K. E. Wilson, I. A. Anderson, *Bioinspiration and Biomimetics* **2018**, 13, 1.
- [21] S. K. Dwivedi, M. Vishwakarma, P. A. Soni, *Mater. Today Proc.* **2018**, 5, 3690.
- [22] A. P. Sarvazyan, M. W. Urban, J. F. Greenleaf, *Ultrasound Med. Biol.* **2013**, 39, 1133.
- [23] V. Sasikala, K. Chitra, *J. Opt.* **2018**, 47, 307.
- [24] S. M. Ha, W. Yuan, Q. Pei, R. Pelrine, S. Stanford, *Adv. Mater.* **2006**, 18, 887.
- [25] N. America, B. C. Burchfiel, P. W. Lipman, T. Parsons, G. Soc, A. Bull, A. Tovish, G. Schubert, B. P. Luyendyk, R. Pelrine, R. Kornbluh, Q. Pei, J. Joseph, *Science*. **2000**, 287, 836.
- [26] S. Michel, X. Q. Zhang, M. Wissler, C. Löwe, G. Kovacs, *Polym. Int.* **2010**, 59, 391.
- [27] R. E. Pelrine, R. D. Kornbluh, J. P. Joseph, *Sensors Actuators, A Phys.* **1998**, 64, 77.

## Chapter 6

# Chapter 7

## Technology assessment

## 7.1 Introduction

In this thesis, the development of dynamic surface topographies in electroactive PDMS coatings has been reported. As intended, the surface dynamics demonstrated respond quickly to an electrical stimulus, while the common issues that occur in dielectric elastomer coatings have been tackled. The driving potentials and applied electrical fields from the literature have been lowered from 1-10 kV and  $\sim 100$  V/ $\mu\text{m}$  to 150-210 V and  $\sim 20$  V/ $\mu\text{m}$ .<sup>[1-3]</sup> Furthermore, the shape of the surface deformations is programmable by the patterning of the ITO electrodes or SU-8 microstructures. Lastly, air pockets have been successfully incorporated in our coatings to generate dynamic topographies that have raised the maximum vibrational responses found in literature<sup>[2,3]</sup> from 400 Hz to 230 kHz. Throughout the thesis, an in-depth explanation and understanding of the mechanisms that drive the surface deformations are provided by comparing the experimental results with finite element method simulations.

Fortunately for future scientists performing research in this interesting field, the story does not end here. Many more challenges, or rather opportunities, still exist and will be discussed in this final chapter. More specifically, the limitations of our systems with respect to different potential applications are discussed and suggestions for future research are provided.

## 7.2 Application prospects

### 7.2.1 Adaptive optics

Mirrors, lenses and diffraction gratings are all optical components that are usually fabricated from rigid materials such as glass, metals, quartz or densely crosslinked polymers. Certain applications, however, require optical elements that can be modified quickly and remotely, without physical replacement of the component itself.<sup>[4,5]</sup> Such applications, ranging from telescopes used in astronomy to retinal

imaging in medicine, require systems based on adaptive optics. The change in reflection that occurs as a result from the deformation of our reflective gold surfaces could potentially be useful in this field. In chapter 5, the change in reflective properties occurring our system is already briefly discussed. Taking another step forward, the dynamic surfaces can also be used to change the diffraction pattern of a laser beam reflected by our coating. In this experiment, the beam of a laser is reflected on the surface of a coating from Chapter 2 at an incoming angle of 20 degrees. Initially, a diffraction pattern is observed resulting from the line grating (the distance between the center of two lines is  $20\ \mu\text{m}$ ) of our interdigitating ITO electrodes (Figure 7.1a). Upon application of the electric field, a secondary diffraction pattern becomes visible, resulting from the standing wave (the distance between the center of two neighboring hills is  $40\ \mu\text{m}$ ) in the gold surface (Figure 7.1b). Furthermore, it should also be possible to switch between undiffracted and diffracted light if that is preferable in the future. Simply

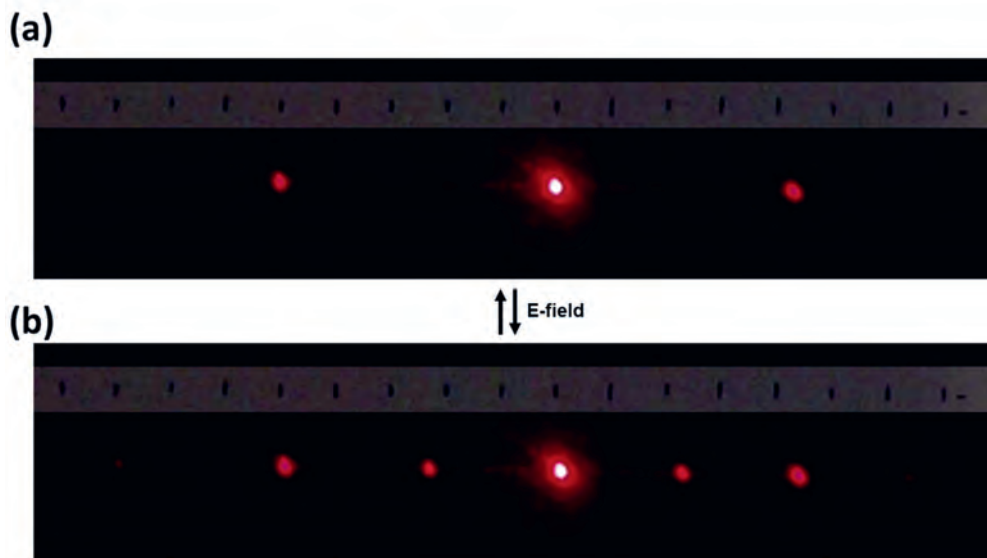


**Figure 7.1 |** Towards applications in adaptive optics. (a) The diffraction pattern observed by reflection of a red laser at an incoming angle of 20 degrees. (b) The diffraction pattern after application of the electric field that create a wave in the gold surface of our coating. A secondary diffraction pattern becomes visible.



adding a black dye to the elastomeric material might already prevent reflection from the ITO pattern underneath the surface.

### **7.2.2 Haptics**

Haptics is the science of sensing and manipulation through touch. In humans, tactile perception is mediated by two subsystems, cutaneous and kinesthetic.<sup>[5]</sup> Cutaneous sensations are pressure, shear or vibrations that can be perceived by the skin, while kinesthetic sensations refer to forces and motions perceived by muscles, tendons and joints. Current technology focusses on various methods to artificially recreate those sensations to enhance realism in virtual worlds or to aid in human performance.<sup>[6]</sup> The electroactive polymer coatings described in this thesis have the potential to be applied in this field. The lowest amplitude of surface wrinkles that can be distinguished by the human finger is approximately 10 nm,<sup>[7]</sup> while the amplitudes of the surface deformations in all our systems are well above this limit. Furthermore, humans can also sense vibrations via two distinct types of mechanoreceptors. The Meissner corpuscles perceive low frequency vibrations ranging from 5 to 50 Hz, while the Pacinian corpuscles register vibrations in the frequency range from 40 to 400 Hz.<sup>[8,9]</sup> As the micro-structured coatings described in Chapter 6 produce vibrations that cover this entire frequency range, we envision that they can also be used to provide vibrational tactions.

To bridge the gap between academic research and real haptic applications, several engineering improvements must be made to ensure the safety of potential users. First, the electroactive polymer coatings can be equipped with a thin and flexible protective layer that provides protection from the electric field and adds resistance against wear. Second, the driving potential of our systems needs to be reduced further to prevent exposure to high voltages. A well-known method to

decrease the driving potential is by increasing the dielectric constant of the elastomer. The dielectric constant can be improved by using polymers that contain large dipoles or by using fillers with a high dielectric constant.<sup>[10]</sup> Alternatively, the driving potential can also be reduced by introducing collapsible pockets of air as we have demonstrated in Chapter 6. Kang et al.<sup>[11]</sup> have shown that porosity in PDMS coatings can also be introduced by using polystyrene (PS) microbeads. In their method, the microbeads are stacked on a Si substrate (Figure 7.2a) and subsequently coated with PDMS (Figure 7.2b). The polymer beads are then removed by submersion in acetone and DMF, which dissolves polystyrene microbeads and detaches the film from the substrate (Figure 7.2c). The stacking of microbeads on our substrate (Figure 7.2d) and the subsequent filling with PDMS could easily be replicated (Figure 7.2e). However, in our systems

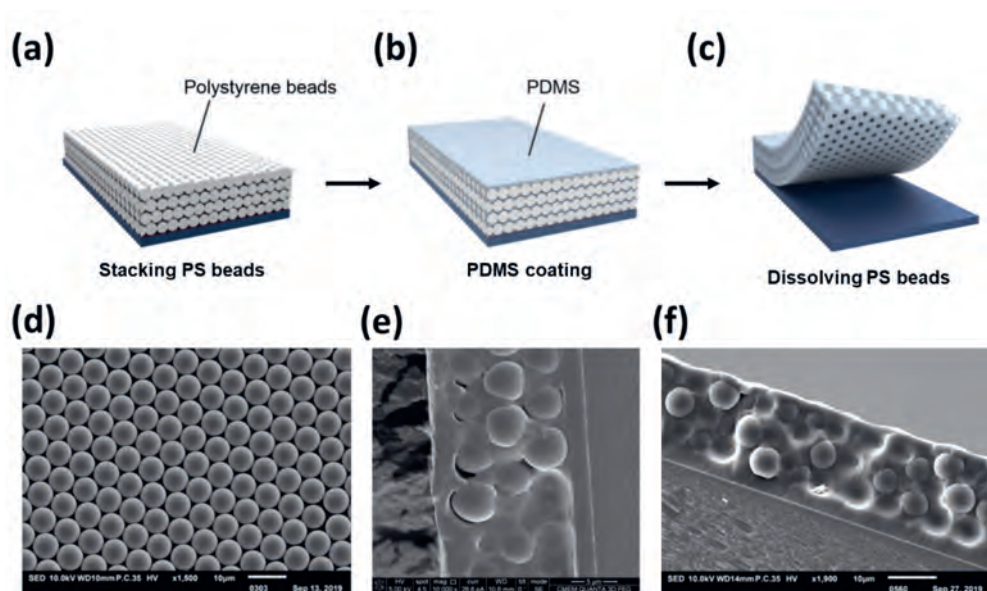


**Figure 7.2** | The use of polystyrene microbeads to create porosity in PDMS coatings. (a) Polymer microbeads are stacked on a Si substrate. (b) The stacked microbeads are coated with PDMS, which fills the space in-between the spheres. (c) The polymer beads are etched by immersing the sample in organic solution, which also results in the detachment of the coating from the substrate. (d) Scanning electron microscopy (SEM) image of a hexagonally packed layer of polystyrene microbeads. (e) SEM image of a cross section of the PDMS coating before etching with organic solvent. (f) SEM image the PDMS coating after etching in organic solvents for 48 hours. Without detachment of the coating, the microbeads can survive the etching treatment.

detachment of the thin coating from the substrate is not desired since the resulting film is fragile and wraps around itself. Unfortunately, complete removal of the PS microbeads while the coating is firmly attached to the substrate could not be achieved with solvents like acetone, DMF or a combination of *n*-heptane and toluene (Figure 7.2f). The use of alternative solvents like chloroform, with a strong swelling effect on PDMS, again caused detachment and tearing of the coating. As a result of the difficulties experienced during the fabrication of these microporous systems, we have explored alternative methods like photolithography with SU-8 to create air pockets in our coatings as described in Chapter 6.

### 7.2.3 Material transport

The displacement of particles induced by changes in surface morphology is useful in applications like self-cleaning. In nature, self-cleaning is usually achieved by creating superhydrophobic surfaces via a combination of microstructures and epicuticular wax.<sup>[12-14]</sup> The water-repellent properties of the surface are used to remove contaminating particles by water droplets, also known as the Lotus effect. Based on this effect, many artificial superhydrophobic coatings have already been developed for self-cleaning purposes.<sup>[15-17]</sup> This self-cleaning mechanism, however, is dependent on wet conditions and therefore ineffective in dry areas like arid deserts where rain is less prevalent. As a solution, the coatings described in this thesis might be applied to mechanically remove dry particles from surfaces, either by changing their morphology or by using high frequency vibrations. The effectiveness of this concept has already been demonstrated in coatings based on liquid crystalline networks, where chaotic oscillatory surface fluctuations result in a fast cleaning of a surface tilted at an angle of 37°.<sup>[18]</sup> Considering the large amplitudes and tunable frequency output of the surface vibrations demonstrated in Chapter 6, these coatings show great potential for use in self-cleaning

applications. As mentioned before, the addition of a thin and flexible protective layer that provides resistance against wear might be necessary for these applications. Also, transparent and flexible electrodes like graphene should be considered as an alternative to the reflective gold electrodes when applied on windows or solar panels.

To continue this topic, it might also be desirable to move material from horizontally placed surfaces, which will require unidirectional motion of the particles similar to the work of Murase et al.<sup>[19]</sup> (Figure 7.3). Mobility of particles in a single direction can be accomplished by introducing asymmetry in either the surface structure or the surface motion figures. An asymmetric surface structure could be introduced on the additional protective layer by equipping it with a ratchet-like structure. An asymmetric surface motion might be achieved by slightly altering the periodicity of the surface microstructures, to create a spectrum of resonance frequencies that can be excited along one direction of the surface. Alternatively, an asymmetric surface motion can also be created by the

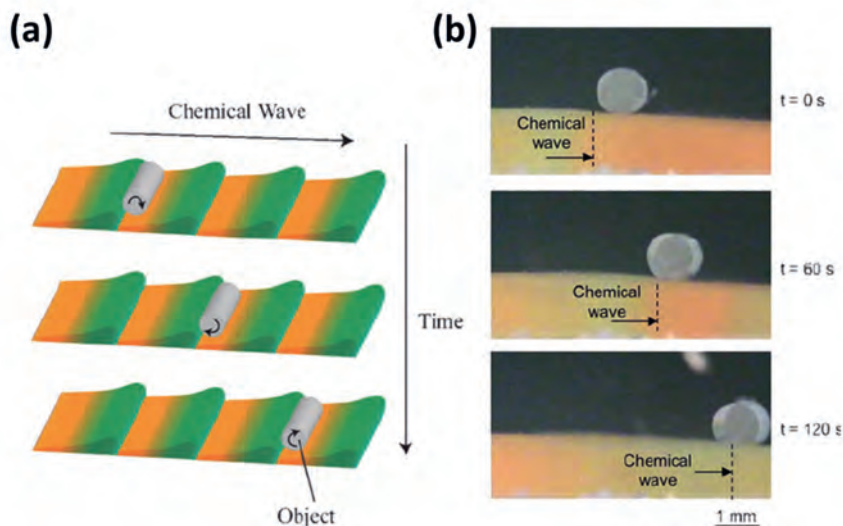


**Figure 7.3** | An example of a surface that can transport mass. (a) Schematic illustration of the peristaltic surface motion. (b) Transportation of a small cylinder over the surface. Reproduced from reference 19.

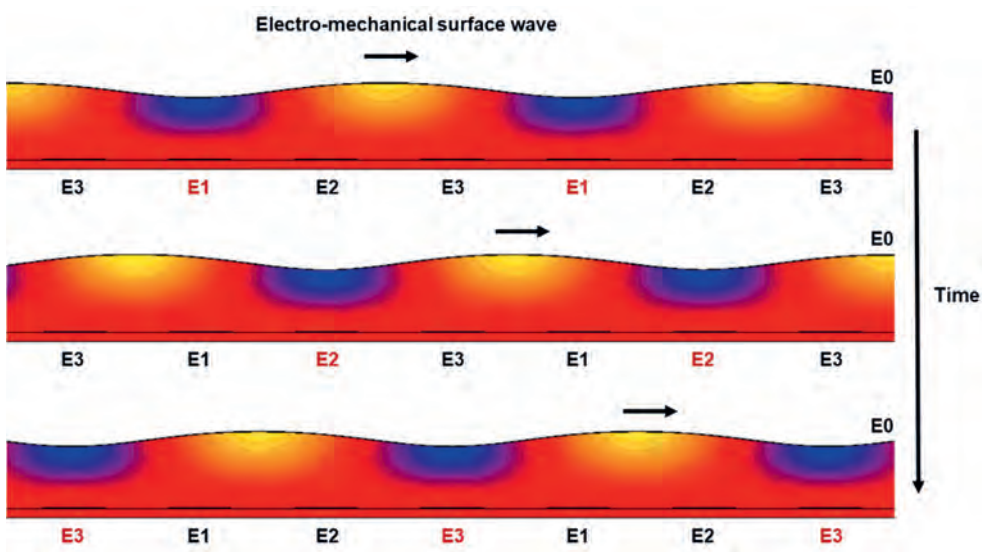


**Figure 7.4 |** Finite element method simulations of a surface wave moving in one direction. During each time-step one ITO electrode is activated (indicated by a red color), which pushes the surface wave forward.

consecutive addressing of multiple ITO electrodes underneath the surface, which will require more complex circuit design. To demonstrate this principle, we have simulated such a system (Figure 7.4) using the finite element method model from Chapter 3. Instead of two ITO electrodes there are now three separate electrodes (E1, E2 and E3) that can be provided with an electrical signal. The width and gap distances of the electrodes are  $10\ \mu\text{m}$ , resulting in an optimal distance of  $30\ \mu\text{m}$  between the hills and the valleys. During actuation, each ITO electrode is activated consecutively, which pushes the surface wave into one direction. The direction of the wave is controlled by the activation sequence of the electrodes (E1-E2-E3 or E3-E2-E1).

#### 7.2.4 Microfluidics

The dynamic surface structures described in this thesis also have the potential to be useful in the field of microfluidics. We envision they can perform two possible functions in microfluidic devices: active mixing and pumping. In typical water

based microfluidic systems, the channels have a width of 100  $\mu\text{m}$  and turbulent mixing does not occur.<sup>[20]</sup> Consequently, researchers are forced to use diffusive mixing, which is an inherently slow process. Passive mixing devices can improve the mixing speed by designing a configuration of microchannels that fold solutions multiple times while flowing through the mixing channel.<sup>[21]</sup> As an alternative, active mixing devices can enhance the mixing efficiency within shorter mixing channels to reduce the size of the device. Several types of active micromixers already exist, ranging from acoustic to dielectrophoretic.<sup>[22–24]</sup> When the dynamic microstructures from our coatings are placed on the inside of the microchannels, they might display comparable mixing efficiency without additional heat generation or direct exposure to electric fields. For acoustic mixing with air bubbles maximum membrane oscillations of 8  $\mu\text{m}$  are used at frequencies of 80 kHz.<sup>[22]</sup> Our devices operate within that frequency range although the amplitudes still need to be improved. Additionally, the surface deformations can exert forces on the liquids that might result in a pumping effect when combined with a valve that only allows flow in a single direction. In future research the amplitudes of our surface dynamics need to be improved further to compete with the existing methods used in pumping or mixing applications.

### **7.2.5 Acoustics**

In Chapter 1 we discussed our interest in increasing the frequency range at which the surface dynamics take place to expand the range of applications of our electroactive polymer coatings to acoustics and communications optics. In Chapter 6 we succeeded in increasing that frequency range to 230 kHz by using resonance effects in elastic poly(dimethyl siloxane) (PDMS) films supported by SU-8 microstructures. To determine if these coatings can be used as transducers in acoustic applications, we now measure the acoustic waves generated by our coating under water using a hydrophone. First, the coating is activated with a sine shaped pulse with a potential of 150 Vpp at a frequency of 230 kHz (Figure

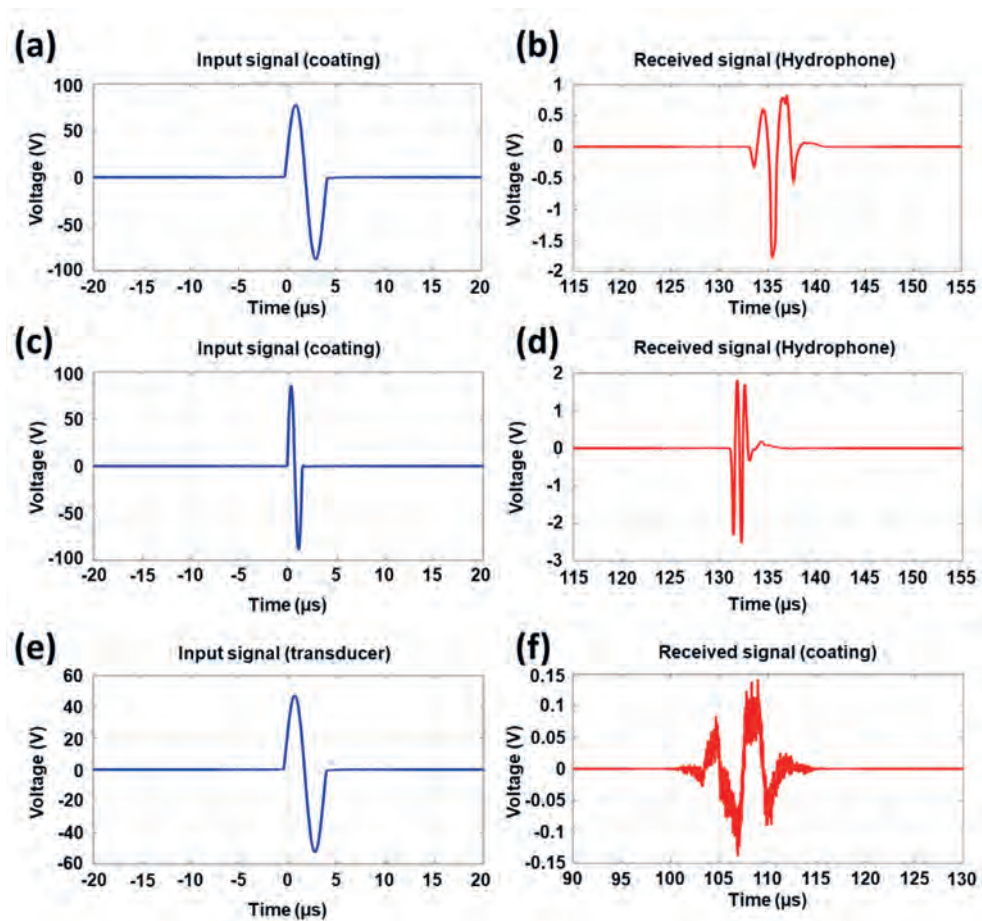


**Figure 7.5** | Results from acoustic characterization of the electroactive polymer coatings under water. (a) The input signal provided to the coatings at a frequency of 230 kHz. (b) The signal received by the hydrophone when a sine shaped pulse at 230 kHz is provided to the coatings. (c) The input signal provided to the coatings at a frequency of 650 kHz. (d) The signal received by the hydrophone when a sine shaped pulse at 650 kHz is provided to the coatings. (e) The input signal provided to a commercial transducer at a frequency of 230 kHz. (f) The signal received by the coatings from a commercial transducer.

7.5a). The hydrophone, placed at a distance of 200 mm, receives the signal after a delay of 133  $\mu\text{s}$  (Figure 7.5b). The received signal has a good signal to noise ratio and a frequency two times larger than the input signal, which indicates the coating oscillates twice during the activation. Second, the frequency of the input signal is increased to 650 kHz (Figure 7.5c). At this frequency, the amplitude of the received signal from the hydrophone is optimal with a potential of 4 Vpp (Figure 7.5d). Again, the frequency of the received signal is twice the frequency

of the input signal and the shape indicates that two vibrations take place at the surface of the coating. The results seem to indicate that the fundamental frequency of the coatings underwater is almost four times higher than in air. Experiments where the input signal consists of a block pulse at a frequency of 1.3 MHz are planned for the near future and should provide a definitive answer. Finally, to further prove the applicability of our coatings in sound transducers, we explore their potential to also receive sound signals. A commercial transducer is used to generate sound waves with a potential of 100 Vpp at a frequency of 230 kHz (Figure 7.5e). The coating, placed at a distance of 150 mm, receives the signal after a delay of 100  $\mu$ s (Figure 7.5b). The received signal shows some random oscillations due to inconsistencies in the coating, but it still indicates that our coatings can receive and detect sound waves. We anticipate that the coatings can still be optimized further by tuning the fundamental frequency with geometrical adjustments and by reducing the thickness of the elastic PDMS film. Nevertheless, the results are very promising and we envisage that after some optimization our coatings can be applied in non-destructive testing<sup>[25]</sup> and medical imaging.<sup>[26]</sup>

### 7.3 Conclusion

In this thesis, we have demonstrated new methods to bring static surfaces into motion by employing electroactive polymers. The use of finite element method simulations has proven invaluable to improve our existing experimental methods or to propose completely new experimental designs. As a result, the systems we have described show potential in a large variety of applications. In this final chapter, we have discussed how some of these applications can benefit from our electric field responsive coatings and what future research is required to make it a reality. We foresee that, although each targeted application presents its own challenges, our electroactive polymer coatings could play an important role in bringing the surfaces of many future devices to life.



## 7.4 References

- [1] S. Shian, D. R. Clarke, *Soft Matter* **2016**, *12*, 3137.
- [2] D. Pyo, S. Ryu, K. U. Kyung, S. Yun, D. S. Kwon, *Appl. Phys. Lett.* **2018**, *112*, 1.
- [3] W. H. Park, T. H. Yang, Y. Yoo, S. Choi, S. Y. Kim, *IEEE World Haptics Conf. WHC 2015* **2015**, 165.
- [4] J. L. Wilbur, R. J. Jackman, G. M. Whitesides, E. L. Cheung, L. K. Lee, M. G. Prentiss, *Chem. Mater.* **1996**, *8*, 1380.
- [5] S. J. Lederman, R. . Klatzky, *Attention, Perception, Psychophys.* **2009**, *71*, 1439.
- [6] H. Culbertson, S. B. Schorr, A. M. Okamura, *Annu. Rev. Control. Robot. Auton. Syst.* **2018**, *1*, 385.
- [7] L. Skedung, M. Arvidsson, J. Y. Chung, C. M. Stafford, B. Berglund, M. W. Rutland, *Sci. Rep.* **2013**, *3*.
- [8] R. S. Johansson, J. R. Flanagan, *Nat. Rev. Neurosci.* **2009**, *10*, 345.
- [9] K. O. Johnson, T. Yoshioka, F. Vega Bermudez, *J. Clin. Neurophysiol.* **2000**, *17*, 539.
- [10] J. Biggs, K. Danielmeier, J. Hitzbleck, J. Krause, T. Kridl, S. Nowak, E. Orselli, X. Quan, D. Schapeler, W. Sutherland, J. Wagner, *Angew. Chemie - Int. Ed.* **2013**, *52*, 9409.
- [11] S. Kang, J. Lee, S. Lee, S. G. Kim, J. K. Kim, H. Algadi, S. Al-Sayari, D. E. Kim, D. E. Kim, T. Lee, *Adv. Electron. Mater.* **2016**, *2*, 1.
- [12] R. Fürstner, W. Barthlott, C. Neinhuis, P. Walzel, *Langmuir* **2005**, *21*, 956.
- [13] W. Barthlott, C. Neinhuis, *Planta* **1997**, *202*, 1.
- [14] C. Neinhuis, W. Barthlott, *Ann. Bot.* **1997**, *79*, 667.
- [15] Y. Lu, S. Sathasivam, J. Song, C. R. Crick, C. J. Carmalt, I. P. Parkin, *Science* **2015**, *347*, 1132.
- [16] K. Liu, L. Jiang, *Annu. Rev. Mater. Res.* **2012**, *42*, 231.
- [17] S. Nishimoto, B. Bhushan, *RSC Adv.* **2013**, *3*, 671.
- [18] W. Feng, D. J. Broer, D. Liu, *Adv. Mater.* **2018**, *1704970*, 1.
- [19] Y. Murase, S. Maeda, S. Hashimoto, R. Yoshida, *Langmuir* **2009**, *25*, 483.
- [20] C. Y. Lee, C. L. Chang, Y. N. Wang, L. M. Fu, *Int. J. Mol. Sci.* **2011**, *12*, 3263.
- [21] Z. Chen, M. R. Bown, B. O'Sullivan, J. M. MacInnes, R. W. K. Allen, M. Mulder, M. Blom, R. van't Oever, *Microfluid. Nanofluidics* **2009**, *6*, 763.
- [22] D. Ahmed, X. Mao, B. K. Juluri, T. J. Huang, *Microfluid. Nanofluidics* **2009**, *7*, 727.
- [23] T. D. Luong, V. N. Phan, N. T. Nguyen, *Microfluid. Nanofluidics* **2011**, *10*, 619.
- [24] M. Campisi, D. Accoto, F. Damiani, P. Dario, *J. Micro-Nano Mechatronics* **2009**, *5*, 69.
- [25] S. K. Dwivedi, M. Vishwakarma, P. A. Soni, *Mater. Today Proc.* **2018**, *5*, 3690.
- [26] A. P. Sarvazyan, M. W. Urban, J. F. Greenleaf, *Ultrasound Med. Biol.* **2013**, *39*, 1133.

# Summary

## Bringing coating surfaces to life

### Electric field-driven surface dynamics of PDMS

This thesis reports on the characterization, potential applications and various approaches to generate dynamic surface topographies in siloxane coatings by applying electric fields. Static micro- and nanostructured coatings provide a huge variety of functions that are useful in applications like self-cleaning, adhesive tapes, drag reduction, anti-icing, anti-fogging and anti-reflection. As a next step in coatings technology, we bring static surfaces into motion to not only provide control over these functionalities, but also to increase their overall effectiveness. Previously, our group has reported on several methods to generate surface dynamics in coatings consisting of liquid crystal polymer networks. These coatings are versatile as the shape of their micro- and nanostructures can be pre-programmed and made responsive to various stimuli like light, temperature, humidity or electricity. Unfortunately, the response time of the coatings is usually about 10 seconds, which limits the frequency of the surface dynamics to maximum of 50 mHz. As such, we decided to explore alternative materials that can respond faster and open the path to high frequency surface dynamics. Furthermore, electricity or electric fields are preferred as a stimulus for these surface dynamics to allow for easy incorporation into electrical devices, but also to provide active control most efficiently.

A well-known method to create electro-mechanical deformations in polymers is by using Maxwell stresses. These Maxwell stresses are

commonly used in dielectric elastomers where a thin free-standing elastomeric film is sandwiched between two flexible electrodes in a two-plate capacitor setup. We expanded on this concept and present methods to obtain electro-mechanical deformations in coatings firmly adhering to rigid substrates by using siloxanes. One method to generate an oscillating wave in a soft siloxane network is by triggering the Maxwell stresses locally in a tri-electrode configuration that contains lateral escape routes for the compressed excess of volume. Despite the viscoelastic properties that allow the siloxane polymer to deform easily, the maximum protrusion height is still obtained within 100 ms after triggering the electric field. Additionally, we use a continuous AC electric field that provides full control over the surface dynamics in terms of frequency (up to 5 Hz), amplitude and start/stop time.

To gain more insight into the deformation mechanics, we performed finite element method simulations of the previously described system. For this study, we used the Marc Mentat nonlinear finite element software with a coupled electrostatic-structural analysis. With the input of the viscoelastic data into the finite element model, we obtain reasonably good agreement between experiment and simulation. Moreover, this tool can be used to predict the outcome of future experiments.

Similar to the liquid crystal network coatings, we also desire to have control over the shape of the surface dynamics. To start off, we determined how the shape is affected by different electric circuits. Next, we employed the previously discussed finite element model to change and optimize the shape of the surface wave with different electrode patterns. Finally, the simulated results are confirmed experimentally, revealing four different types of oscillating surface waves that can be created.

To add desired complexity to the deformation patterns in the electroactive polymer coatings we further modified the electrode structures. Finite element modelling is used to predict the complex deformation figures. Supported by the simulations we created those deformation patterns experimentally and demonstrated the optical effects that result from the change in surface texture.

At this point we have a well described and understood system with great control of the surface dynamics. The only limitations of these coatings are their softness and maximum frequency, both related to the viscoelastic properties of the siloxane. To overcome these limits, we presented a new method to create high frequency surface dynamics using a tougher coating that consists of a densely crosslinked elastic siloxane network supported by SU-8 microstructures. Dependent on the shape of the SU-8 structures resonance frequencies as high as 230 kHz are discovered where the surface vibrates at significantly increased amplitudes and speeds.



# Samenvatting

## Bringing coating surfaces to life

### Electric field-driven surface dynamics of PDMS

Dit proefschrift beschrijft de karakterisatie, potentiële toepassingen en verschillende methodes om dynamische oppervlakte-topografieën te maken in coatings van siloxaan door gebruik te maken van elektrische velden. Coatings met statische micro- en nanostructuren kunnen in een groot aantal gebieden worden toegepast zoals in zelfreinigende oppervlaktes, plakband, frictie-verlaging, anti-bevriezing, anti-condensatie en anti-reflectie. Om de coatings verder te ontwikkelen, hebben wij die statische oppervlaktes in beweging gebracht. Op die manier krijgen we niet alleen meer controle over de functies, maar wordt ook hun effectiviteit verhoogd. In het verleden heeft onze onderzoeksafdeling gedemonstreerd hoe het oppervlak van coatings in beweging kan worden gebracht door gebruik te maken van een netwerk van gepolymeriseerde vloeibare kristallen. Deze coatings zijn veelzijdig, aangezien de vorm van de micro- en nanostructuren vooraf kan worden geprogrammeerd. Daarnaast kunnen ze reageren op verschillende prikkels zoals licht, temperatuur, vochtigheid of elektriciteit. Het nadeel van deze coatings is de snelheid waarmee ze reageren op een prikkel. Meestal duurt het vervormings-proces ongeveer 10 seconden, waardoor de frequentie van de oppervlakte bewegingen gelimiteerd is tot een maximum van 50 mHz. Om deze limitatie te omzeilen zijn wij op zoek gegaan naar alternatieve materialen die sneller reageren op prikkels en oppervlakte-bewegingen met hogere frequenties mogelijk maken. Daarnaast geven we de voorkeur aan elektriciteit of elektrische

velden als prikkel voor de oppervlakte-bewegingen, omdat de technologie dan makkelijk kan worden ingebouwd in bestaande elektronische apparatuur en tegelijkertijd actieve controle biedt.

Het gebruik van Maxwell stress is een bekende methode om polymeren te vervormen met behulp van elektriciteit. Deze Maxwell stress wordt veelal gebruikt in 'dielektrische elastomeren' waarbij flexibele elektrodes zijn aangebracht aan twee kanten van een dunne laag vrij-staand elastomeer, vergelijkbaar met de opbouw van een condensator. Wij hebben dit concept uitgebreid en presenteren methodes om coatings van siloxanen elektro-mechanisch te vervormen, terwijl ze stevig vastzitten aan een hard oppervlak. Een van de methodes maakt gebruik van drie verschillende elektrodes om de Maxwell stress lokaal aan te brengen, waardoor tussenliggende vluchtroutes ontstaan voor het overtollige volume. Met deze methode is het mogelijk om een oscillerende golf te creëren in het zachte siloxaan netwerk. Ondanks de visco-elastische eigenschappen die ervoor zorgen dat het siloxaan makkelijk vervormt worden de maximale hoogtes van de oppervlaktestructuren bereikt binnen 100 ms na het aanbrengen van het elektrisch veld. Daarnaast maken we gebruik van een continu wisselend elektrisch veld waardoor we volledige controle hebben over de oppervlakte bewegingen op het gebied van frequentie (tot 5 Hz), amplitude en start/stop tijd.

Om meer inzicht te krijgen in de manier waarop de oppervlakte deformatie plaatsvindt, hebben we simulaties uitgevoerd met een eindige-elementenmethode. Voor dit onderzoek hebben we de niet-lineaire software van Marc Mentat gebruikt met een gekoppelde elektrostatic-structurele analyse. Met de invoer van de visco-elastische eigenschappen van het materiaal komen de resultaten van de simulatie goed overeen met

de experimentele data. Daarnaast kan dit model worden gebruikt als hulpmiddel om de resultaten van toekomstige experimenten te voorspellen.

Net zoals bij de coatings van gepolymeriseerde vloeibare kristallen, willen we ook bij de siloxaan coatings controle hebben over de vorm van de oppervlakte bewegingen. Allereerst hebben we onderzocht hoe de vorm wordt beïnvloed door verschillende elektrische circuits. Vervolgens hebben we het eerder besproken eindige-elementenmodel gebruikt om de vorm van de oppervlaktegolf met verschillende elektrodepatronen aan te passen en te optimaliseren. Tenslotte hebben we de gesimuleerde resultaten experimenteel bevestigd, waaruit bleek dat er vier verschillende soorten oppervlaktegolven kunnen worden gecreëerd.

Om de vervormbare oppervlaktepatronen nog complexer te maken, hebben we de structuur van de elektrodes verder aangepast. Wederom is het eindige-elementenmodel gebruikt om de complexe vervormingen te voorspellen. Met ondersteuning van de simulaties zijn de complexere vervormingspatronen gemaakt en de optische effecten die ontstaan door de verandering van de textuur van het oppervlak aangetoond.

Op dit punt hebben we een goed gedefinieerd en begrepen systeem met veel controle over de bewegingen van het oppervlak. De enige beperkingen van deze coatings zijn hun zachtheid en maximaal haalbare frequentie, die beiden gerelateerd zijn aan de visco-elastische eigenschappen van het siloxaan. Om deze beperkingen te omzeilen, hebben we een nieuwe methode gepresenteerd om hoogfrequente oppervlaktebewegingen te creëren. Deze nieuwe methode maakt gebruik van een stevigere coating die bestaat uit een siloxaan netwerk met een hogere vernettingsdichtheid, ondersteund door microstructuren van SU-8. Afhankelijk van de vorm van



de SU-8 structuren kan het oppervlak resoneren op frequenties tot 230 kHz, waarbij het oppervlak trilt met aanzienlijk grotere amplitudes en snelheden.

# Acknowledgments

Na ruim vier jaar intensief onderzoek ben ik aan het einde gekomen van mijn promotietraject en kan ik vol trots mijn proefschrift uitdelen. Tijdens deze periode heb ik ontzettend veel steun gekregen van mijn collega's, vrienden en familie. Zonder jullie hulp had was ik nooit zo ver gekomen.

Allereerst wil ik graag mijn promotoren prof. Dick Broer en prof. Albert Schenning bedanken. Dick, bedankt voor alle creatieve en uitdagende ideeën die je met mij deelde om mijn onderzoek vooruit te helpen. Met een schijnbaar onuitputtelijke bron kennis heb je mij keer op keer weten te inspireren. Zelfs wanneer de resultaten tegenvielen straalde je vertrouwen uit, waardoor ik weer met enthousiasme aan de slag kon met nieuwe suggesties. Albert, bedankt voor alle doortastende vragen en opmerkingen tijdens de SFD meetings. Ze hebben mij geholpen mijn onderzoek te verbeteren. Verder heb ik de afgelopen jaren vollop genoten van de prettige en stimulerende werkomgeving die heerst binnen SFD. Jij hebt deze sfeer gecreëerd door de groep op een enthousiaste, open en efficiënte manier te leiden.

I also want to thank my copromotor, dr. Danqing Liu. Danqing, thank you for all your encouragement and support throughout the last four years. Under your supervision I have learned to perform results focused experiments, critically evaluate my data, write with vision and persevere when experiments have unexpected outcomes. You have helped me grow professionally and personally.

Furthermore, I would like to thank prof. Kitty Nijmeijer, prof. Gerwin Gelinck, prof. Takahiro Seki and prof. Julius Vancso for taking your time to evaluate

my thesis and being part of my doctoral committee. I am looking forward to your questions during my PhD defense.

Graag wil ik nu ook alle andere vaste stafleden van SFD bedanken. Michael, Johan and Cees, thank you for always taking an interest in my research. I highly appreciate the many questions, comments and suggestions I got from you during my SFD presentations. Tom, jij bent altijd bereid om mensen te helpen. Het maakt niet uit of het gaat om het verplaatsen van onderdelen, bestellingen, kapotte apparatuur, onverklaarbare data, persoonlijke frustraties, politieke discussies, vrijdagmiddagpraat of een cursus flirten in het Chinees, bij jou kan je terecht. Ik weet nu al dat ik je ga missen op mijn volgende werkplek. Marjolijn, dankzij jou verloopt alles binnen SFD altijd soepel en als vanzelf. Bedankt voor je inlevingsvermogen en bereidheid om iedereen helpen. Soms had je zelfs al oplossingen voor problemen waar ik nog niet eens van op de hoogte was!

Next, I also would like to thank my collaborators. Dr. Hubert Gojzewski, thank you for your can-do mentality during the AFM measurements at Twente University. Dr. Jack Massaad and Dr. Paul van Neer, thank you for sharing your expertise during the acoustic analysis of our dynamic coatings at the Delft University of Technology. My trip to Delft was a nice break from the lockdown and I think we were all pleasantly surprised with the results from those experiments. Finally, I also want to thank the students that have contributed to my research. Erik, Anne, Dennis and Zaneta, thank you for the nice collaborations. I hope you have learned as much from me as I have from you. Good luck in your further careers.

To all former and current members of SFD and other groups, thank you for the awesome times in the lab, at the F.O.R.T., during lunch and at the coffee table: Alberto, Anahita, Annelore, Anping, Arne, Danielle, Davey, Diederik,

Dirk-Jan, Jody, Ellen, Eveline, Frankje, Gilles, Huiyi, Jeroen, Jeroen, Li, Marc, Marcos, Marina, Matthew, Niki, Patri, Pei, Rob, Roel, Sarah, Sean, Sebastian, Shajeth, Simon, Sterre, Stijn, Tom, Yari, Yuanyuan, Xiaohong, Xinglong, Wanshu, Wei, Wilson. A special word of thanks for Yuanyuan, my paronymph, dear officemate and Chinese "twin sister". We shared all the good and bad things that happened to us during the last four years. Even though we have different cultural backgrounds, we really understand each other. You are always welcome at our place to share a room with Pumbaa. Davey, samen met Yuanyuan was het altijd gezellig op kantoor. Ik kan je verfrissende oprechtheid en behulpzaamheid ontzettend waarderen. Stijn, bedankt voor de gezelligheid tijdens onze avonturen op de A50. We hebben het er gelukkig zonder kleerscheuren vanaf gebracht.

Verder heb ik ook nog een hartstikke leuke groep vrienden overgehouden aan mijn tijd in Nijmegen: Annelous, Annemiek, Anouk, Christel, Conny, Fleur, Isabelle, Leanne, Pol, Sander, Toine en Verena. Hopelijk kan ons volgende VIP weekend weer doorgaan. Sander en Fleur, ik geniet altijd enorm van de gezellige avonden (tegenwoordig middagjes) die wij met ons vieren doorbrengen. Hopelijk wonen we ook over een paar jaar nog dicht bij elkaar. Sander, bedankt dat je mijn paranimf wil zijn.

Isabella en Bart, fijn dat jullie lekker dichtbij wonen. In tijden van crisis kunnen we altijd bij elkaar terecht. Isabella, (Sistha!) ik zal nooit vergeten hoe je voor mij opkwam toen ik de ziekte van Lyme had. Daarnaast had ik geen beter zus kunnen wensen als slachtoffer voor al mijn plagerijtjes.

Gewone oma, bedankt voor alle gezellige logeerpartijen en fijne herinneringen. Ik denk nog altijd aan die keer dat ik onbeperkt frituursnacks mocht eten. Opa Loe, bedankt voor alle steun, informatieve wandelingen door de natuur en verhalen over de dassenburcht. Ik ken weinig mensen

die zoveel passie voor de natuur hebben. Oma Annie en gewone opa, ik denk nog vaak aan jullie.

Lieve pap en mam, bedankt dat jullie altijd voor me hebben klaargestaan, wat er ook gebeurde. Dankzij jullie ben ik zover gekomen. Mam, jij stimuleerde me altijd om mijn best te doen op school, ook al zei ik soms zeer overmoedig: 'Achjoh, dat komt wel goed.' Ik geniet er nog steeds van om samen met jou lekker de slappe lach te krijgen. Pap, dankzij jouw handigheid en bouwkundige kennis wonen Anouk en ik in een prachtig huisje. Zonder jou sliepen we misschien nog steeds op kurken vloeren met een oerwoud als voortuin en verstopte rioleringen.

Lieve Anouk, de afgelopen jaren heb je mij door dik en dun gesteund. Je maakt mij gelukkig en je zorgt ervoor dat ik me speciaal voel. Ik weet zeker dat we samen een mooie toekomst tegemoet gaan.

# Curriculum Vitae

Fabian Visschers was born on June 20<sup>th</sup>, 1992 in Meerssen, the Netherlands. After finishing high school in 2010 at Stella Maris College in Meerssen, he moved to Nijmegen to study Chemistry at the Radboud University. In 2016, he successfully defended his master thesis within the 'Physical-Organic & Supramolecular Chemistry' group under the supervision of prof.dr. Roeland Nolte and dr. Hans Elemans. After an industrial internship at Océ – A Canon Company in Venlo he received his Master's degree in 2017. That same year he started his PhD project at the Eindhoven University of Technology in the 'Stimuli-responsive Functional Materials and Devices' group under the supervision of prof.dr. Dick Broer, prof.dr. Albert Schenning and dr. Danqing Liu. The most important results of his PhD research are described in this thesis.





# List of Publications

## Publications related to this thesis

- F.L.L. Visschers, M. Hendrikx, Y. Zhan, D. Liu, Liquid crystal polymers with motile surfaces, *Soft Matter*, **2018**, 14, 4898-4912.
- F.L.L. Visschers, H. Gojzewski, G.J. Vancso, D.J. Broer, D. Liu, Oscillating surfaces fueled by a continuous AC electric field, *Advanced Material Interfaces*, **2019**, 1901292.
- F.L.L. Visschers, D.J. Broer, D. Liu, Electric-field induced oscillating surface waves with programmable shapes, *Proceedings of SPIE 11375, Electroactive Polymer Actuators and Devices XXII*, **2020**, 1113751F.
- F.L.L. Visschers, D.J. Broer, D. Liu, Patterned surface dynamics at substrate-restricted electroactive silicone coatings, (submitted).
- F.L.L. Visschers, J. Massaad, P. van Neer, D. Liu, D.J. Broer, High-frequency surface dynamics in electroactive polymer coatings with SU-8 microstructures, (manuscript in preparation).

## Other publications

- Y. Zhan, G. Zhou, B.A.G. Lamers, F.L.L. Visschers, D.J. Broer, D. Liu, Artificial organic skin wets its surface by field-induced liquid secretion, *Matter*, **2020**, 3, 782-793.



- K. Stout, T.P.J. Peters, M.F.J. Mabesoone, F.L.L. Visschers, E.M. Meijer, J.R. Klop, J. van den Berg, P.B. White, A.E. Rowan, R.J.M. Nolte, J.A.A.W. Elemans, Double Porphyrin Cage Compounds, *European Journal of Organic Chemistry*, **2020**, 45, 7087-7100.

